NASA Contractor Report 165661

ADVANCED STABILITY ANALYSIS FOR LAMINAR FLOW CONTROL

Steven A. Orszag

CAMBRIDGE HYDRODYNAMICS, INC.

CAMBRIDGE, MASSACHUSETTS 02139

CONTRACT NAS1-15894

FEBRUARY 1981

National Aeronautics and Space Administration

Langley Research Center
Hampton, Virginia 23665

NASA Contractor Report 165661

ADVANCED STABILITY ANALYSIS FOR LAMINAR FLOW CONTROL

Steven A. Orszag

CAMBRIDGE HYDRODYNAMICS, INC.

CAMBRIDGE, MASSACHUSETTS 02139

CONTRACT NAS1-15894

FEBRUARY 1981

National Aeronautics and Space Administration

Langley Research Center
Hampton, Virginia 23665

TABLE OF CONTENTS

I. Introduction

In this report, we summarize work done under NASA Contract No. NAS1-15894 on advanced stability theory analyses for laminar flow control. The report consists of six sections, of which the last five are independent reports that summarize our progress on different aspects of this work.

In Section II, we present a summary of our work on the SALLY stability analysis code for compressible flow problems. The resulting computer code seems to be at least an order of magnitude more efficient than previously developed codes.

In Section III, we present a comparison of methods for prediction of transition using the incompressible SALLY computer code. It is shown that transition prediction by the envelope method and a new modified wave packet method are comparable in reliability but that the envelope method is more efficient computationally.

In Section IV, we present a study of instability and transition in rotating disk flow in which the effects of Coriolis forces and streamwise curvature on transition are investigated. Good agreement between the theory and experiments performed at NASA Langley Research Center has been achieved using the e^N method with N of order 10 at the onset of transition.

In Section V, we present a new 'linear' three-dimensional instability mechanism that predicts Reynolds numbers for transition to turbulence in planar shear flows that agrees well with experiment. We have extended the SALLY stability codes to compute directly this new instability mechanism. The results are in good agreement with experiment. Subcritical transitional Reynolds numbers of order 1000 in plane Poiseuille and plane Couette flow and of order 2000 in pipe Poiseuille flow have been found.

In Section VI, we present results obtianed using our stability analysis codes to study the finite-amplitude (nonlinear) stability of axisymmetric pipe Poiseuille flow. Our results are in disagreement with the earlier analytical work of Davey, Itoh, and Stuart. There appear to be no finite-amplitude nonlinear axisymmetric instabilities, in contrast to the predictions of the above-mentioned authors. The conclusion is that extreme care must be exercised in the application of Landau-Stuart-Watson perturbation ideas to such flows.

II. Efficient Computation of Compressible Flow Stability of Three-Dimensional Boundary Layers

In this section we present a method for calculation of compressible flow stability of three-dimensional boundary layers. The method is based upon a two point boundary value (direct) approach and is more efficient than the commonly used shooting methods (1, 2) by an order of magnitude.

The computer code SALLY (3) which was developed for LFC (laminar flow control) design applications employed incompressible stability theory. It is highly desirable to develop a COMPRESSIBLE SALLY code which can be used as a design tool for LFC applications. One basic prerequisite for such a code is a fast eigenvalue solver for compressible stability equations which comprise of a system of eight first order equations. The existing numerical methods generally use Runge-Kutta integration procedure along with Gram-Schmidt orthonormalization to control the parasitic error growth. This procedure is often very slow and thus very inefficient if used in a black box stability code such as SALLY. We describe here an efficient method for obtaining eigenvalues of the compressible stability equations. This method will be used in the compressible version of SALLY.

We write the governing equations as

$$(A\,D^2 + B\,D + C)\,\tilde{\phi} = 0 \qquad (1)$$

where $\tilde{\phi}$ is a 5 row vector defined as

$$\tilde{\phi} = \begin{pmatrix} \alpha u' + \beta w' \\ \alpha w' - \beta u' \\ T' \\ V' \\ P' \end{pmatrix} \qquad (2)$$

and A, B, C are 5 X 5 matrices with the following structure:

$$A = \begin{pmatrix} 1 & 0 & 0 & 0 & 0 \\ 0 & 1 & 0 & 0 & 0 \\ 0 & 0 & 1 & 0 & 0 \\ 0 & 0 & 0 & 0 & 0 \\ 0 & 0 & 0 & 0 & 0 \end{pmatrix}$$

$$B = \begin{pmatrix} b_{11} & b_{12} & 0 & 0 & 0 \\ b_{21} & b_{22} & b_{23} & 0 & 0 \\ 0 & b_{32} & b_{33} & 0 & 0 \\ 0 & 0 & 0 & b_{44} & 0 \\ b_{51} & b_{52} & 0 & 0 & b_{55} \end{pmatrix} \qquad (3)$$

$$C = \begin{pmatrix} c_{11} & c_{12} & 0 & c_{14} & c_{15} \\ 0 & c_{22} & 0 & c_{24} & c_{25} \\ 0 & c_{32} & c_{33} & c_{34} & 0 \\ c_{41} & c_{42} & 0 & c_{44} & c_{45} \\ c_{51} & c_{52} & 0 & c_{54} & c_{55} \end{pmatrix}$$

In the above $D \equiv \frac{d}{dy}$, where y is the normal boundary layer coordinate and V' is the corresponding perturbation amplitude. u' and w' are the perturbation amplitudes in x and z directions and α, β are the respective wave numbers. T' and P' are the amplitudes of temperature and pressure fluctuations respectively.

The boundary conditions for Equation (1) are

$$y = 0; \quad \phi_1 = \phi_2 = \phi_3 = \phi_4 = 0$$

$$y \to \infty; \quad \phi_1, \quad \phi_2, \quad \phi_3, \quad \phi_4 \to 0 \qquad (4)$$

In order to solve eigenvalue problems posed by Equations (1) and (4), we represent Equation (1) by central differences which results in a block-tridiagonal system of equations with 5 X 5 blocks. The system of equations is solved using Lu factorization. We use inverse iteration procedure (4) for eigenvalue search. This method is very effective once a good guess for the eigenvalue is available because the convergence is cubic.

If we write Equation (1) as

$$L \phi = 0$$

then, the inverse iteration algorithm for obtaining eigenvalue can be written as

$$(L - \lambda_k I) \phi_{k+1} = f \phi_k$$

$$(L - \lambda_k I)^T \psi_{k+1} = f' \psi_k$$

$$\lambda_{k+1} = \psi_{k+1}^T L \phi_{k+1} \Big/ \psi_{k+1}^T \phi_{k+1}^T$$

The finite-difference method presented above is second order accurate. However, the accuracy of the eigenvalue obtained by this procedure can be increased by Richardson's extrapolation. For this purpose we use Neville's algorithm.

If

$$P_i^{(0)} = \lambda (h_i) \qquad (i = 0, \ldots m)$$

where h_i is the grid size, then

$$P_i^{(j)} = P_{i+1}^{(j-1)} + \frac{P_{i-1}^{(j-1)} - P_i^{(j)}}{\left(\frac{h_i}{h_{i+j}}\right)^2 - 1} \qquad \begin{matrix} j = 1, \ldots m \\ i = 0, \ldots m-j \end{matrix} \qquad (6)$$

We present here eigenvalue results for the leading edge region (R = 150) of a 35^o swept back wing of infinite span. Table 1 gives the eigenvalues calculated for different grids ($h_i = \frac{1}{N_i}$) and the extrapolated values. The sequence for h_i chosen is that proposed by Bulirsch and Stoer (5) which gives an eigenvalue converged to five significant digits. The cost of computation obviously depends upon the required accuracy. Generally, an eigenvalue accurate to 3 significant digits can be obtained in less than 2 seconds on Cyber 175. Figure 1 shows eigen-function distribution for the same flow as above.

Another way to increase accuracy is to use Chebyshev spectral method (6). The spectral methods provide infinite order of accuracy and are extremely desirable particularly for high Reynolds number applications. Let us represent Equation (1) as

$$L_{sp} \tilde{\phi} = f \qquad (7)$$

where L_{sp} is a spectral operator.

The direct solution of (7) by Gauss elimination methods would require order N^2 (N = number of points) and order N^3

arithmatic operations. We describe here a method which permits solution of (7) using order N storage locations with the number of arithmetic operations of the order of N log N. Specifically we use Chebyshev acceleration scheme (7):

$$L_{ap}\,\phi^{n+1} = L_{ap}\left[\omega_n\,\phi^{(n)} + (1-\omega_n)\,\phi^{(n-1)}\right] - \alpha\,\omega_n\,(L_{sp}U^{(n)} - f) \qquad (8)$$

where L_{ap} is an approximate finite-difference operator and ω_n is a relaxation parameter. The error in the solution of Equation (7) is decreased by a factor of 10^6 after about 9 iterations of Equation (8).

REFERENCES

1. Mack, L. M., "On the Stability of the Boundary Layer on Transonic Swept Wing," AIAA paper 79-0264 (1979).

2. Lekoudis, S., "Stability of Three-Dimensional Compressible Boundary Layers Over Wings With Suction," AIAA paper 79-0265 (1979).

3. Srokowski, A.J. and Orszag, S. A., "Mass Flow Requirements for LFC Wing Design," AIAA paper 77-1222 (1979).

4. Wilkinson, J. H., "The Algebraic Eigenvalue Problem," Oxford, 1965.

5. Bulirsch, R. and Stoer, J., "Numerical Treatment of Ordinary Differential Equations by Extrapolation Methods," Num. Math. 8, 1-13, 1966.

6. Orszag, S. A., "Advanced Stability Theory Analyses for Laminar Flow Control," NASA CR3233 (1980).

7. Ames, W. F., "Numerical Methods for Partial Differential Equations," Barnes & Noble, Inc., New York, 1969.

TABLE 1.

RICHARDSON EXTRAPOLATED EIGENVALUES λ-- (α = .2724, β = - .2915)

N	m =	1	2	3	4	5	6
	i						
20	1	-.2541052E-01 .662266E-02					
			-.2505890E-01 .6155269E-02				
40	2	-.2514681E-01 .6272069E-02		-.2508804E-01 615854GE-02			
			-.2508481E-01 .6158182E-02				
60	3	-.2511236E-01 .6208798E-02		-.2508700E-01 .6158786E-02	-.2500698E-01 .6158802E-02		
			-.2508645E-01 .6158633E-02		-.2508797E-01 .6159012E-02	-.2508800E-01 .6159018E-02	
80	4	-.2510183E-01 .6186852E-02		-.2508786E-01 .6158987E-02			-.2508785E-01 .6159061E-02
			-.2508751E-01 .6153899E-02		-.2508786E-01 .6159057E-02	.2508786E-01 .6159060E-02	
120	5	-.2509352E-01 .6171322E-02		-.2508786E-01 .6150047E-02			
			-.2503777E-01 .6159010E-02				
160	6	-.2509100E-01 .6165936E-02					

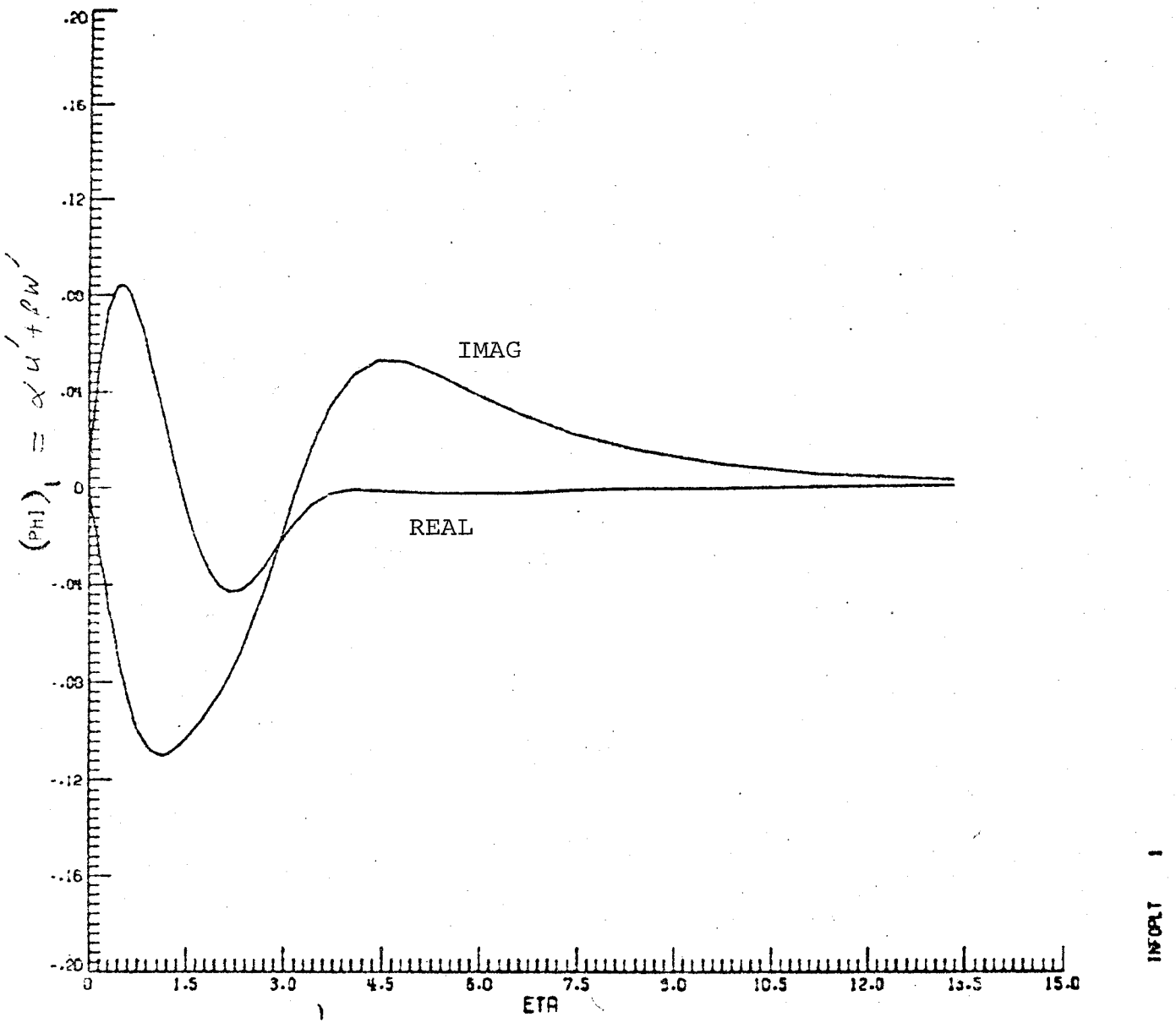

Fig. 1(a) EIGEN-FUNCTION DISTRIBUTION (α = .2724, β = -.2915)

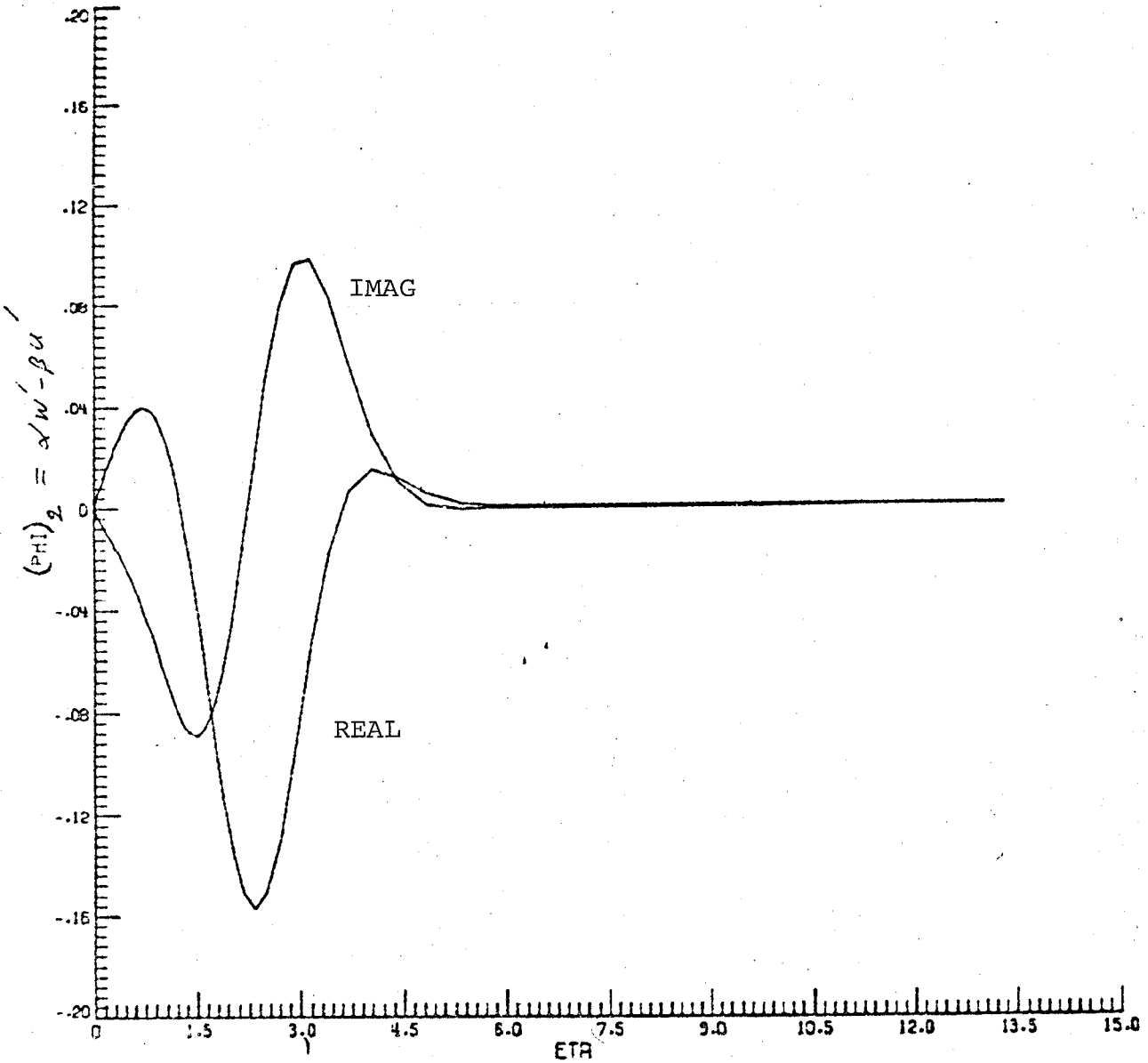
IMAG
REAL
$(PHI)_2 = \alpha w' - \beta u'$
.20
.16
.12
.08
.04
0
-.04
-.08
-.12
-.16
-.20
0
1.5
3.0
4.5
6.0
7.5
9.0
10.5
12.0
13.5
15.0
ETA
INFOPLT 1

Fig. 1(b)

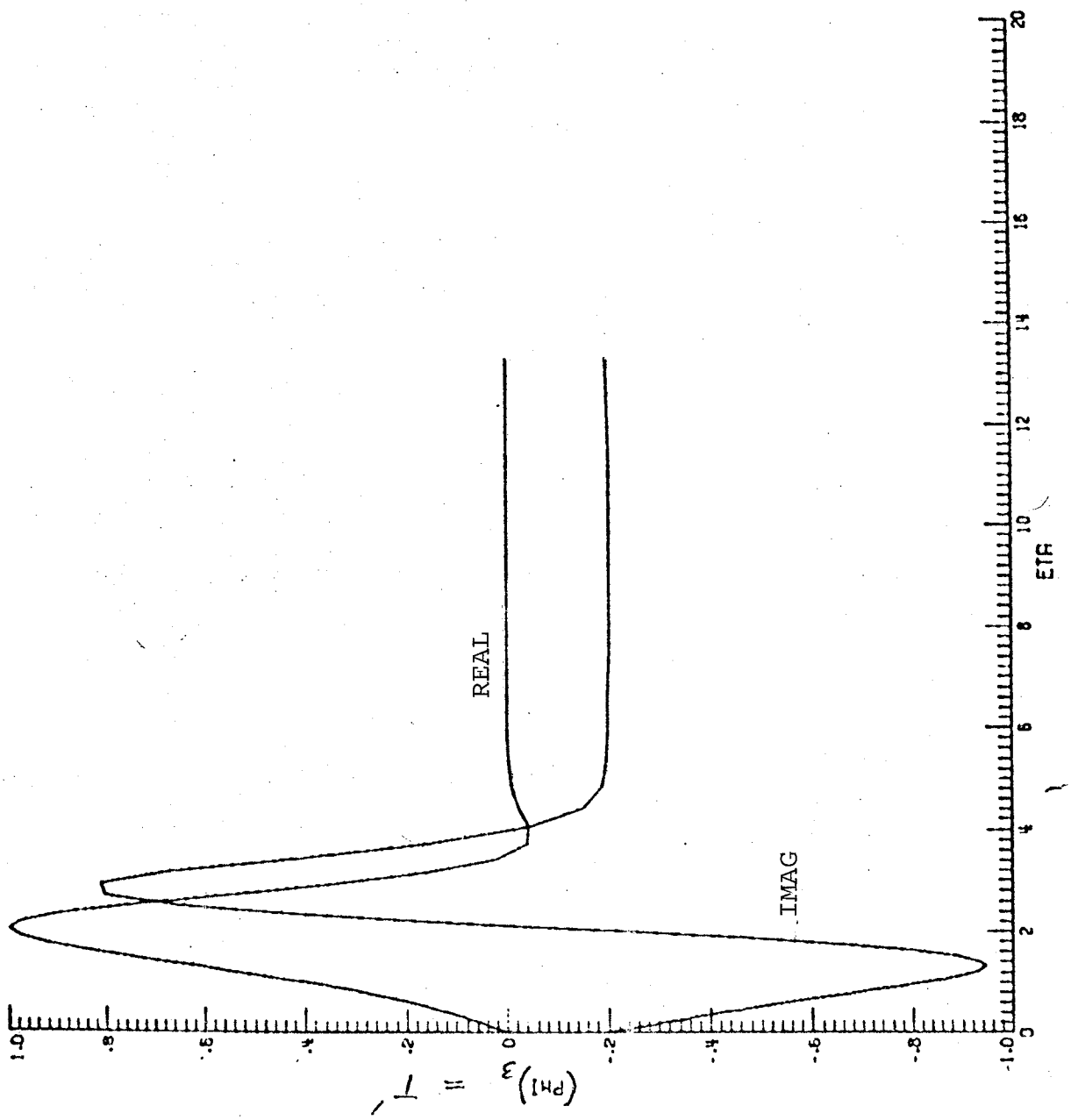

Fig. 1(c)

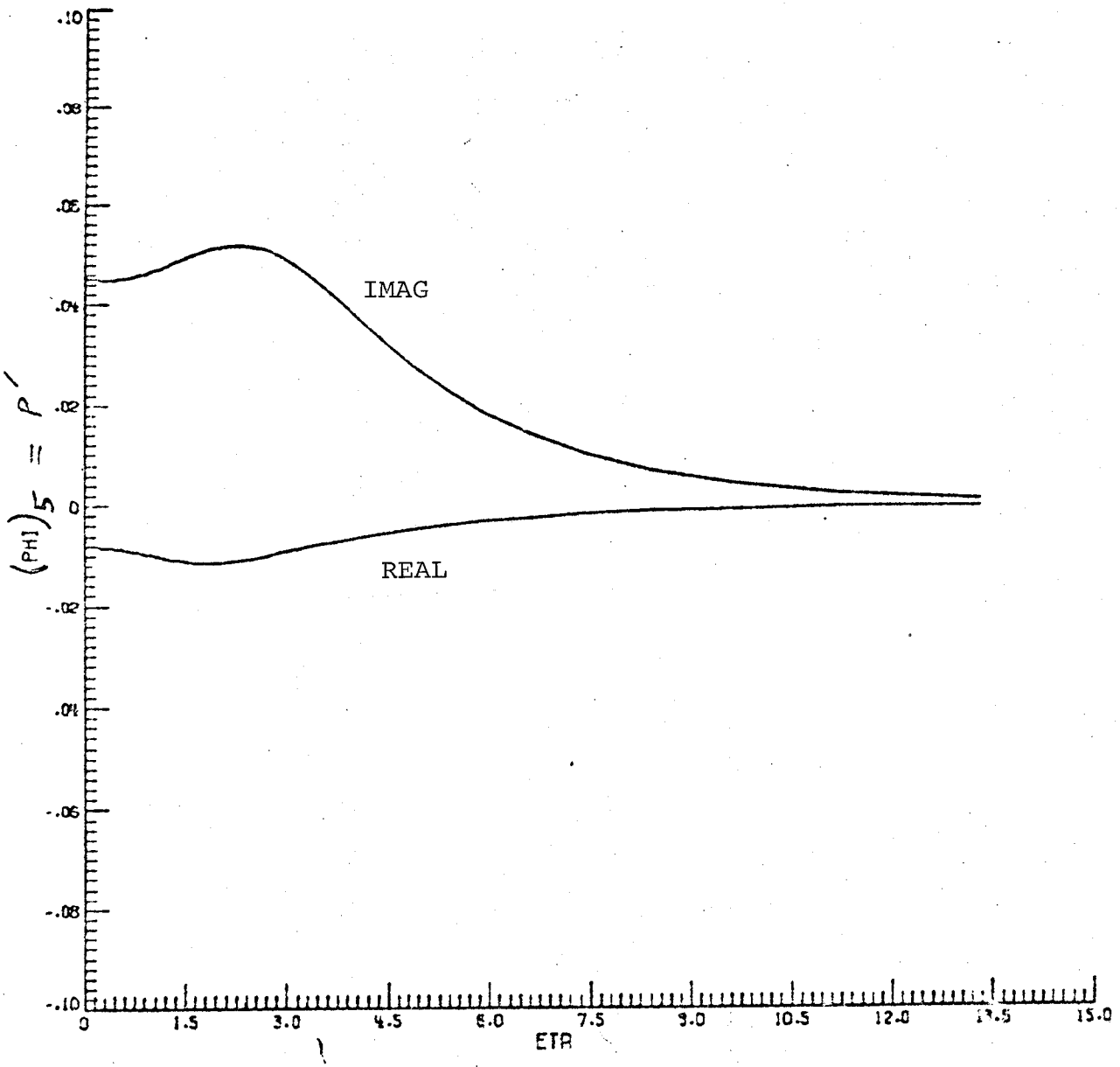
.10
.08
.06
.04
.02
0
-.02
-.04
-.06
-.08
-.10
$(PHI)_5 = P'$
IMAG
REAL
0
1.5
3.0
4.5
6.0
7.5
9.0
10.5
12.0
13.5
15.0
ETA

Fig. 1(d)

III. Comparison of Methods for Prediction of Transition by Stability Analysis

ABSTRACT

Several methods of transition prediction by linear stability analysis are compared. The spectral stability analysis code SALLY is used to analyze flows over laminar flow control wings. It is shown that transition prediction by the envelope method and a new modified wave packet method are comparable in reliability but that the envelope method is more efficient computationally.

NOMENCLATURE

A	maximum disturbance amplitude
a_n	Chebyshev coefficients
c	wing chord
f	dimensional frequency
$\vec{k}$	wave vector
L	algebraic mapping parameter
N	N-factor = $\ell n\ A/A_0$
R	displacement thickness Reynolds number, $U_x \delta^* / \nu_\infty$
Re_c	chord Reynolds number, $U_\infty\ c/\nu_\infty$
s	arc length along an arbitrary path on the wing
T_n	Chebyshev polynomial
t	time
U	unperturbed x-velocity in the boundary layer
$\vec{U}_p$	potential flow vector at edge of boundary layer
U_x	x-component of $\vec{U}_p$
U_∞	incoming free stream velocity
$\vec{v}_g$	group velocity vector
v'	perturbation velocity in the y-disection
W	unperturbed z-velocity in the boundary layer
w	mapped coordinate normal to wing surface
x	coordinate in the direction of the normal chord
y	coordinate normal to the wing surface
z	coordinate along the wing span

α	x-wave number
α_A	angle of attack
β	z-wave number
ω	frequency
δ^*	displacement thickness
λ	wave length
ν	kinematic viscosity
θ	wing sweep angle
ψ	angle formed by the wave number vector with the x-axis
ψ_g	angle formed by the group velocity vector with the x-axis
ψ_p	angle formed by the potential flow vector with the x-axis
ϕ	eigenfunction; defined in Eq. (3).

INTRODUCTION

In this section, several methods of transition prediction using linear stability analysis are compared. The incompressible linear stability computer code SALLY is used in various ways to study three-dimensional boundary layer flow over laminar flow control (LFC) wings. Here we compare the so called envelope method[1] with wave-packet methods[2], to predict transition. We conclude that the envelope method is at least as reliable as the more complicated and less efficient wave packet method.

Consider the stability of three dimensional laminar flow over swept wings with sweep angle θ. The coordinate system used on the wing is depicted in Fig. 1. The x-axis is in the direction of the normal chord, the y-axis is normal to the surface of the wing while the z-axis is along its span.

Neglecting the curvature of the wing surface, compressibility effects, and non-parallel flow effects, linear disturbances satisfy the Orr-Sommerfeld equation

$$\left(\frac{d^2}{dy^2} - \alpha^2 - \beta^2\right)^2 \phi$$

$$= iR\left\{ (\alpha U + \beta W - \omega) \left[\frac{d^2}{dy^2} - \alpha^2 - \beta^2\right]\phi - \left(\alpha\frac{d^2U}{dy^2} + \beta\frac{d^2W}{dy^2}\right)\phi \right\} \quad (1)$$

with the boundary conditions

$$\phi(0) = \frac{d\phi}{dy}(0) = 0; \quad \phi(\infty) \text{ bounded.} \tag{2}$$

Here the perturbation velocity in the y-direction is assumed to be of the form

$$v' = [\mathrm{Re}[\phi(y)e^{i(\alpha x+\beta z-\omega t)}], \tag{3}$$

$U(y)$ and $W(y)$ are the (unperturbed) laminar boundary layer velocities in the x- and z-directions, respectively, and R is the Reynolds number. It is assumed that all variables are non-dimensionalized with boundary layer scaling.

Equations (1) - (3) constitute an eigenvalue problem for the frequency ω and wavenumbers α,β. For given Reynolds number R, this eigenvalue problem provides a complex dispersion relation of the form

$$\omega = \omega(\alpha,\beta) \tag{4}$$

relating the complex parameters α,β and ω.

Semi-empirical methods to predict transition on LFC wings are based on tracing the evolution of modes across the wing.[1] An appropriate N-factor for transition correlation is defined as the (logarithm of the) total growth factor across the wing (see below). A good transition predictor is one for which transition occurs at nearly constant N for a wide variety of wings and flow conditions.

For natural transition, disturbances of all frequencies are present on the wing surface. In this case, there are many optional ways to compute N factors. The first choice is between temporal and spatial stability theory. In temporal theory, α and β are real while ω is complex; the mode grows in time if $\mathrm{Im}(\omega) > 0$, but the mode does not grow in space. An N-factor for transition correlation may be defined as

$$N = \int_{s_0}^{s} \mathrm{Im}(\omega)/|\mathrm{Re}(\vec{v}_g)|\,ds \qquad (5)$$

where $\vec{v}_g = (\partial\omega/\partial\alpha,\ \partial\omega/\partial\beta)$ is the (complex) group velocity and s is the arclength along an appropriate curve on the wing. The N-factor (5) is not fully defined until a prescription is given for singling out a specific mode at each position on the wing and for defining a specific curve on which to integrate. We shall return to these questions in Sec. 2.

In spatial stability theory, ω is real but α and/or β may be complex. Again, there is arbitrariness in the definition of an appropriate N-factor because of the variety of excitable modes on the wing.

WAVE PROPAGATION IN BOUNDARY LAYERS

The complex eigenvalue relation (4) provides two real relations among the three complex quantities $\alpha, \beta,$ and ω. In temporal stability theory, the requirements that α and β be real provide two more conditions so there remain two arbitrary parameters among $\mathrm{Re}(\alpha)$, $\mathrm{Re}(\beta)$, $\mathrm{Re}(\omega)$, and $\mathrm{Im}(\omega)$.

There are several ways to remove this arbitrainess in the computation of the growth factors N. In the envelope method[1], $\mathrm{Im}(\omega)$ is maximized with respect to α at fixed Re ω [which then determines α, β and ω uniquely at each point on the wing] and the curve in (5) is defined to be everywhere tangent to $\mathrm{Re}(\vec{v}_g)$.

With spatial stability theory, there remains three independent real parameters among α, β and $\mathrm{Re}(\omega)$ once the eigenvalue condition (4) is satisfied. One possibility is to require that the direction of most rapid growth, which is parallel to the vector $(-\mathrm{Im}(\alpha), -\mathrm{Im}(\beta))$, be parallel to $\mathrm{Re}(\vec{v}_g)$ and that the resulting value of the most rapid growth rate be maximized with respect to the remaining two independent parameters.[3]

Alternatively, it is possible to use wave

packet theory to remove the arbitrariness in the definition of N-factors. For a conservative dynamical system, kinematic wave theory implies that a wave packet propagates in physical and wavevector space according to the Hamilton-Jacobi equations[4]

$$\frac{dx}{dt} = \frac{\partial \omega}{\partial \alpha} \tag{6}$$

$$\frac{dz}{dt} = \frac{\partial \omega}{\partial \beta} \tag{7}$$

$$\frac{d\alpha}{dt} = -\frac{\partial \omega}{\partial x} \tag{8}$$

$$\frac{d\beta}{dt} = -\frac{\partial \omega}{\partial z} \tag{9}$$

Nayfeh[2] considered the extension of Eqs. (6)-(9) to non-conservative systems where $\alpha, \beta,$ and ω can be complex. Then, ω_α and ω_β may also be complex. For a physical solution with real $x,z,$ and t to exist, (6) and (7) imply that the group velocity $(\omega_\alpha, \omega_\beta)$ must be real. Nayfeh proposed the computation of wave packet solutions determined by the six independent conditions: (i) the eigenvalue condition (4); (ii) $\text{Im}\ \omega_\alpha = \text{Im}\ \omega_\beta = 0$; (iii) Re ω fixed; (iv) Re β fixed; and (v) $dx/dt = \omega_\alpha$, $dy/dt = \omega_\beta$. Under these conditions the N-factor is determined by

$$N = \int_{t_0}^{t} [-\omega_\alpha \mathrm{Im}(\alpha) - \omega_\beta \mathrm{Im}(\beta) + \mathrm{Im}(\omega)]\,dt \qquad (10)$$

Finally we study a modified non-conservative wave packet formulation in which $\alpha, \beta,$ and ω are determined by: (i) the eigenvalue condition (4); (ii) $\mathrm{Im}\ \omega_\alpha = \mathrm{Im}\ \omega_\beta = 0$; (iii) $\mathrm{Re}\ \omega$ fixed with $\mathrm{Im}\,\omega = 0$; and (iv) $dx/dt = \omega_\alpha$, $dy/dt = \omega_\beta$. The motivation for these latter conditions is simply that laminar flow over a LFC wing may be assumed steady so a wave packet should propagate at fixed real frequency. However, there is less justification for assuming $\mathrm{Re}\ \beta$ is fixed as in Nayfeh's formulation, because the flow is not homogeneous in space. The N-factor is given by (10) with $\mathrm{Im}(\omega) = 0$.

With Nayfeh's formulation of the wave packet equations, the growth factor N is a function of the independent variables $\mathrm{Re}\,\omega$ and $\mathrm{Re}\ \beta$, while N is a function of only $\mathrm{Re}\,\omega$ in our wave packet formulation. Therefore, maximization of N over all allowable packets is computationally more efficient with our formulation. We have performed computations (not reported in detail here) with Nayfeh's wave packet formulation and have found the computations to be extremely sensitive, with realistic solutions satisfying the required constraints at some wing locations but not at others and the overall N factor at transition highly

valuable. We do not believe these latter effects originate in the numerical scheme. In any case, the conclusion of the present paper that the envelope method is at least as reliable as the wave packet method and that it is considerably more efficient would not be changed by comparisons with results obtained by Nayfeh's wave packet formulation.

NUMERICAL METHOD

In the computer code SALLY[1], Eqs. (1) - (2) are solved using a spectral method based on Chebyshev polynomials[5]. The boundary layer direction y $0 \leq y < \infty$, is mapped into the finite interval $-1 \leq w < 1$ by the algebraic mapping

$$w = 2 \frac{y}{y+L} - 1 \tag{11}$$

and $\phi(y)$ is approximated as the finite Chebyshev polynomial series

$$\phi(y) = \sum_{n=0}^{N} a_n T_n(w) \tag{12}$$

The resulting algebraic eigenvalue problem is solved globally (if a guess for the eigenvalue is not available) by a generalized QR algorithm or locally (if a good guess is available) by inverse Rayleigh iteration[6]. The resulting scheme is very efficient and accurate.

The properties of the laminar boundary layer profiles required to solve (1) - (2) are obtained using a compressible boundary layer code for swept tapered wings developed by Kaups and Cebeci.[1]

The code SALLY also performs a number of optional computations, including: (i) computation of maximum amplification among all wavelengths and propagation angles; (ii) computation of amplification at fixed frequency and fixed wave length; (iii) computation of amplification at fixed frequency and fixed propagation angle; (iv) computation of maximum amplification at fixed frequency; and (v) computation of wave packet solutions according to the prescriptions discussed in Sec. 2.

RESULTS

Burrows[7] has reported flight transition data taken at Cranfield for a large, untapered, 45° swept half wing mounted as a dorsal fin upon the mid-upper fuselage of an Avro Lancaster airplane. The airfoil section was made-up of two semi-ellipses, one of which constituted a faired trailing edge and the other corresponding to the leading edge of a 10 percent thick airfoil, with effective chord of 10.83 feet, measured in the free stream direction. The location of the beginning of transition in the Cranfield data was estimated as given in Ref. 8. Two of the Cranfield flight rests were chosen for correlating transition using wave packet theory.

In the first test case, calculations were made for a chord Reynolds number of 11.7×10^6 and $-2°$ angle of attack. In this flow, transition begins at $x/c = 5.5\%$. A maximum N factor of 7.6 was obtained at a frequency of 1250 Hz both with the envelope method and the modified wave packet method.

The predicted variation of the N factor up to the transition location was almost identical for the envelope method and the modified wave packet method. We also compute the solution of the conservative wave packet equations (6) - (9) in which only the real parts of equations (6) - (7) are taken while (8)-(9)

are solved in their full complex form. The resulting N factor at transition is 5.2. The variation of N factor with x/c for the various methods is plotted in Fig. 2.

Wave angle, wave length and the direction of the group velocity as predicted by the envelope and wave packet methods are given in Figs. 3 - 5. Although the results are qualitatively similar, there is appreciable quantitative difference in these parameters at the transition location. It is surprising that the N factor calculated by the envelope and modified wave packet methods are the same.

In the second test case, the angle of attack of the wing was changed to zero. In this case, transition occurred experimentally at x/c = 7%. The envelope method gave an N factor of 10.8 at a frequency of 1000 Hz. The wave packet method gave a maximum N factor of 10.5 at a frequency of 1200 Hz, which is close to the prediction of the envelope method. The variation of N factor with x/c is plotted in Fig. 6. The predictions of the conservative wave packet approximation and a fixed wavelength, fixed frequency integration are also plotted in this figure. The conservative wave packet approximation gave an N factor at transition of 8.6 rather than 10.5.

Figure 7 shows the influence of frequency on N factor at transition for the wing as predicted by the wave packet theory. Wave angle, wave length and direction of the group velocity for this particular wing are shown in Figs. 8-10. Again there is substantial quantitative difference in the predictions of the two methods.

CONCLUSIONS

Calculations were made for a Cranfield 45° swept wing with $Re_c = 11.7 \times 10^6$ using a modified wave packet method and the envelope method. Both methods gave an N factor of 7.6 at transition location for an angle of attack, $\alpha_A = -2°$. For $\alpha_A = 0°$, the envelope and modified wave packet methods gave N factors of 10.8 and 10.5, respectively. Since it may be argued that the wave packet method is physically more relevant for predicting transition in three dimensional boundary layers, it was initially hoped that the wave packet method might give more consistent transition N factors. However, the results show that the wave packet method provides N factors which are at best as consistent as those of envelope method. Since the wave packet method is at least 3 times as expensive to use as the envelope method, the latter is recommended for engineering design calculations.

REFERENCES

1. Srokowski, A. J., and Orszag, S. A., 'Mass Flow Requirements for LFC Wing Design', AIAA Paper No. 77-1222, 1977.

2. Nayfeh, A. H., 'Stability of Three-Dimensional Boundary Layers', AIAA Paper No. 79-0262, 1979.

3. Mack, L. M., 'Transition Prediction and Linear Stability Theory, In AGARD Conference Proceedings No. 224, Laminar-Turbulent Transitions, Paper No. 1, 1977.

4. Courant, R. and Hilbert, D., Methods of Mathematical Physics, Vol.2, Interscience Publishing Co., New York, 1962.

5. Orszag, S. A., 'Accurate Solution of the Orr-Sommerfeld Equation', Journal of Fluid Mechanics, Vol. 50, 1971, p. 689.

6. Benney, D. J. and Orszag, S. A., 'Stability Analysis for Laminar Flow Control', NASA CR-2910, 1977.

7. Burrows, F. M., 'A Theoretical and Experimental Study of the Boundary Layer Flow on a 45° Swept Back Wing', COA Report No. 109, The College of Aeronautics, Cranfield, 1956.

8. Hefner, J. N. and Bushnell, D. M., Application of Stability Theory to Laminar Flow Control', Paper presented at thel2th AIAA Fluid and Plasma Dynamics Conference, July 24-26, 1979, Williamsburg, Virginia.

FIGURE CAPTIONS

Figure 1. A plot of the coordinate system on a swept wing.

Figure 2. A plot of N versus percent of chord x/c for various methods applied to a swept wing of an Avro Lancaster airplane at $-2°$ angle of attack. Solid curve: modified wave packet method and envelope method at $f = 1250$ Hz which gives nearly the maximum N at the transition point. Dashed curve: result of integrating equations (6) - (9) across the wing with (6) and (7) replaced by their real parts. The curves are plotted from the beginning of the unstable flow region until the transition point at $x/c = 5.5\%$.

Figure 3. A plot of wave propagation angle versus x/c for the same flow as in Figure 2.

Figure 4. A plot of wavelength versus x/c for the same flow as in Figure 2.

Figure 5. A plot of the direction of the group velocity for the same flow as in Figure 2.

Figure 6. Same as Fig. 2 except for the wing at $0°$ angle of attack. In addition to the results of the wave packet methods and envelope method, the N

factor obtained by integrating a fixed wavelength, fixed frequency mode across the wing is given. Here N is given by (5) and the mode is determined by the six real conditions: (i) Eq. (4); (ii) $\mathrm{Im}\,\alpha = -\mathrm{Im}\,\beta = 0$; (iii) $\lambda/c = 0.001$; (iv) $\mathrm{Re}\,\omega = 750$ Hz.

Figure 7. Variation of N at transition versus frequency obtained using the modified wave packet method for the same flow as in Figure 6.

Figure 8. A plot of wave propagation angle versus x/c for the same flow as in Figure 6.

Figure 9. A plot of wavelength versus x/c for the same flow as in Figure 6.

Figure 10. A plot of the direction of the group velocity for the same flow as in Figure 6.

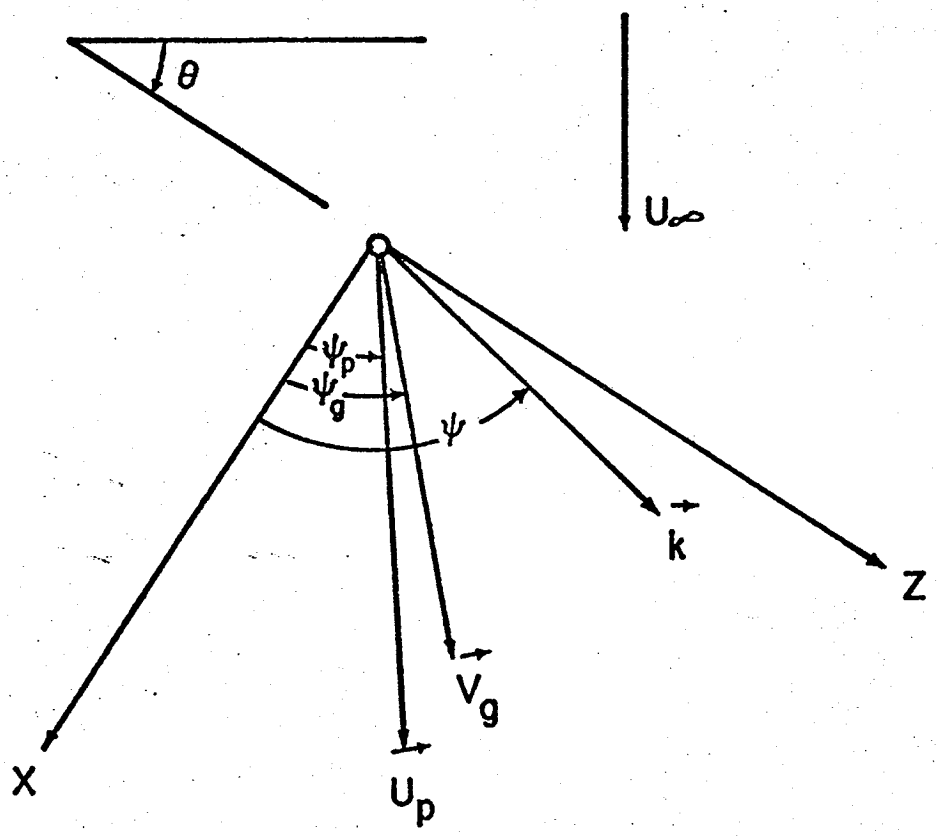

Figure 1.

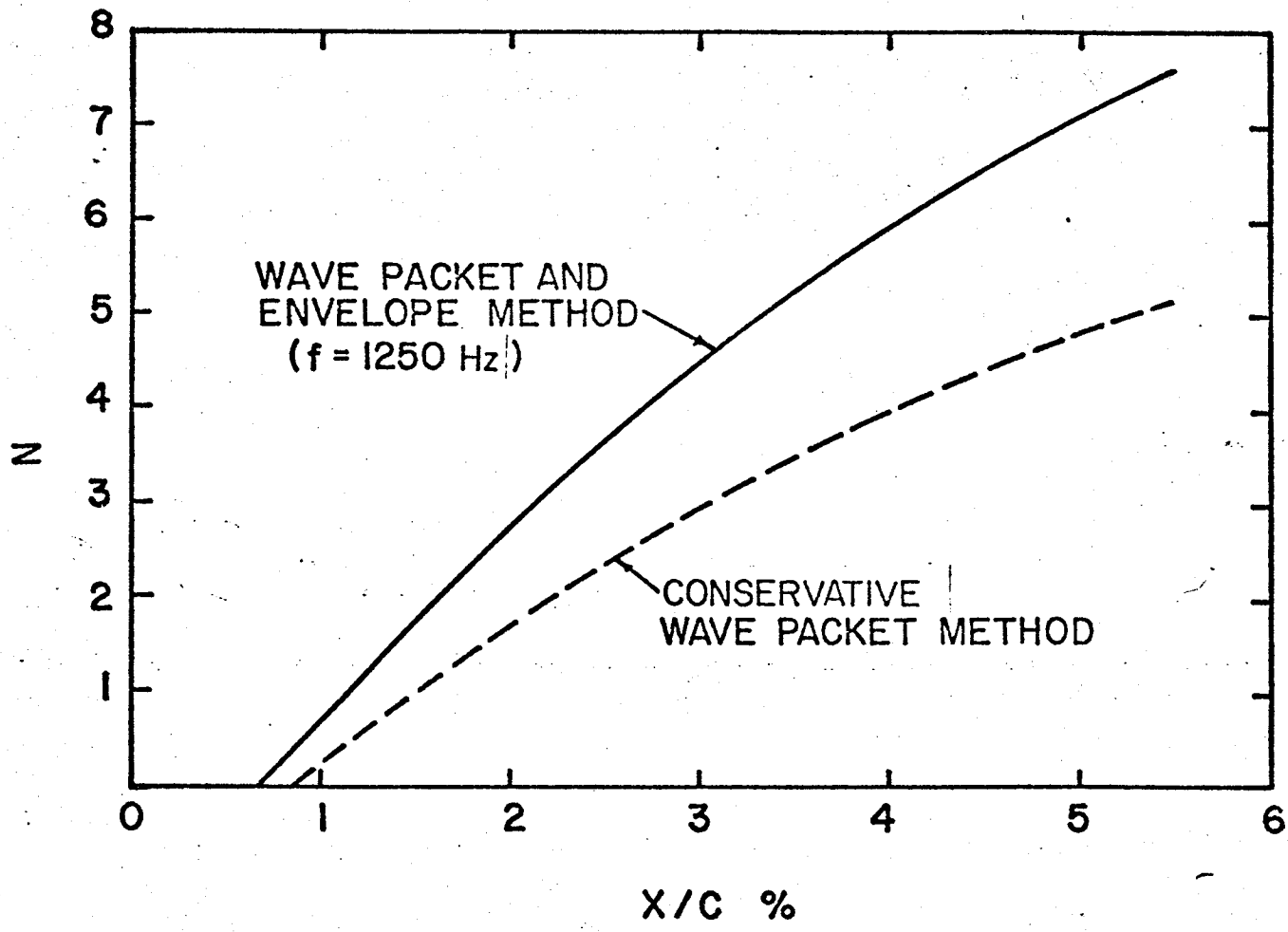
8
7
6
5
4
3
2
1
N
0
1
2
3
4
5
6
X/C %
WAVE PACKET AND
ENVELOPE METHOD
(f = 1250 Hz)
CONSERVATIVE
WAVE PACKET METHOD

Figure 2.

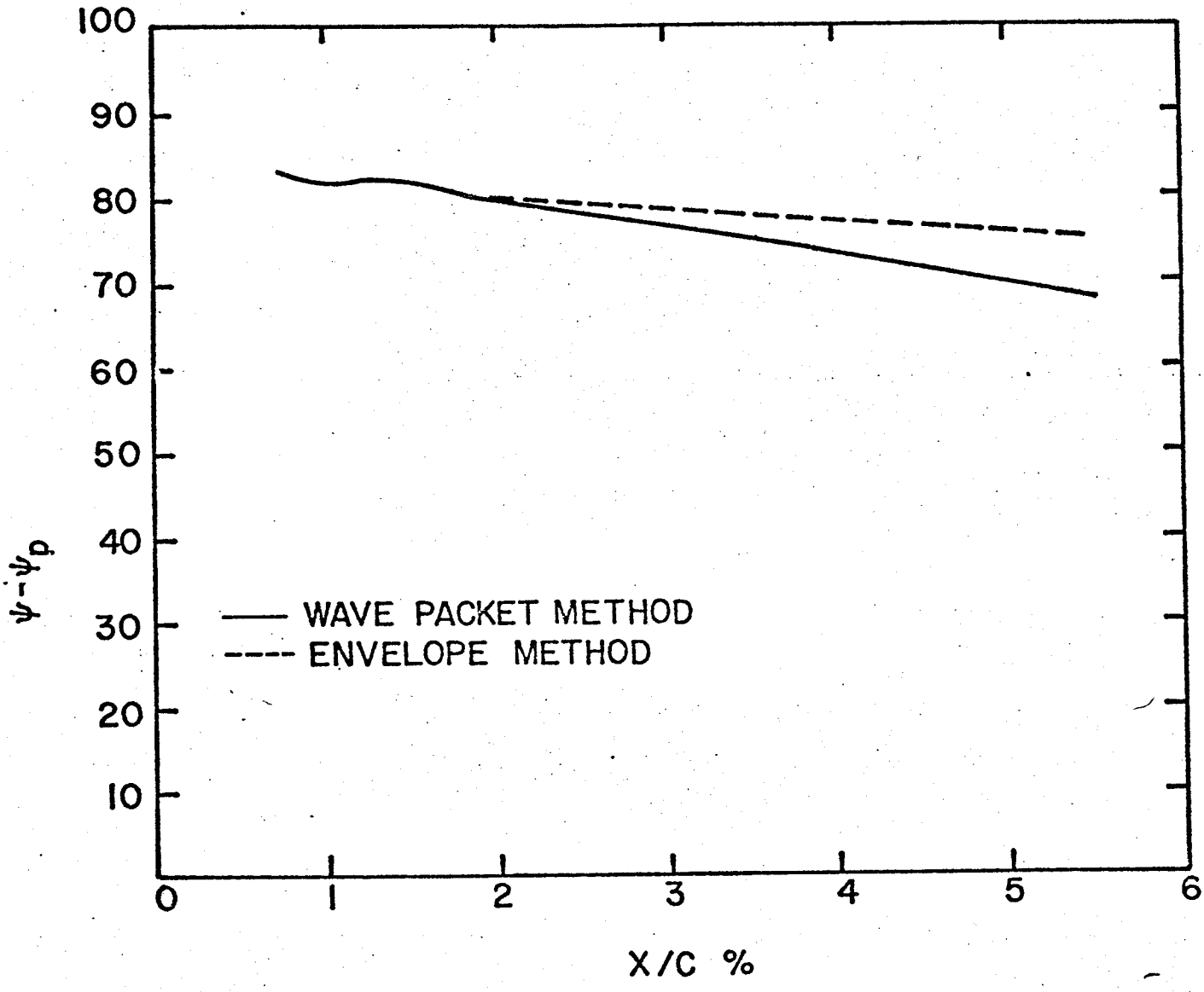
100
90
80
70
60
50
40
30
20
10
0
1
2
3
4
5
6
$\psi - \psi_p$
WAVE PACKET METHOD
ENVELOPE METHOD
X/C %

Figure 3.

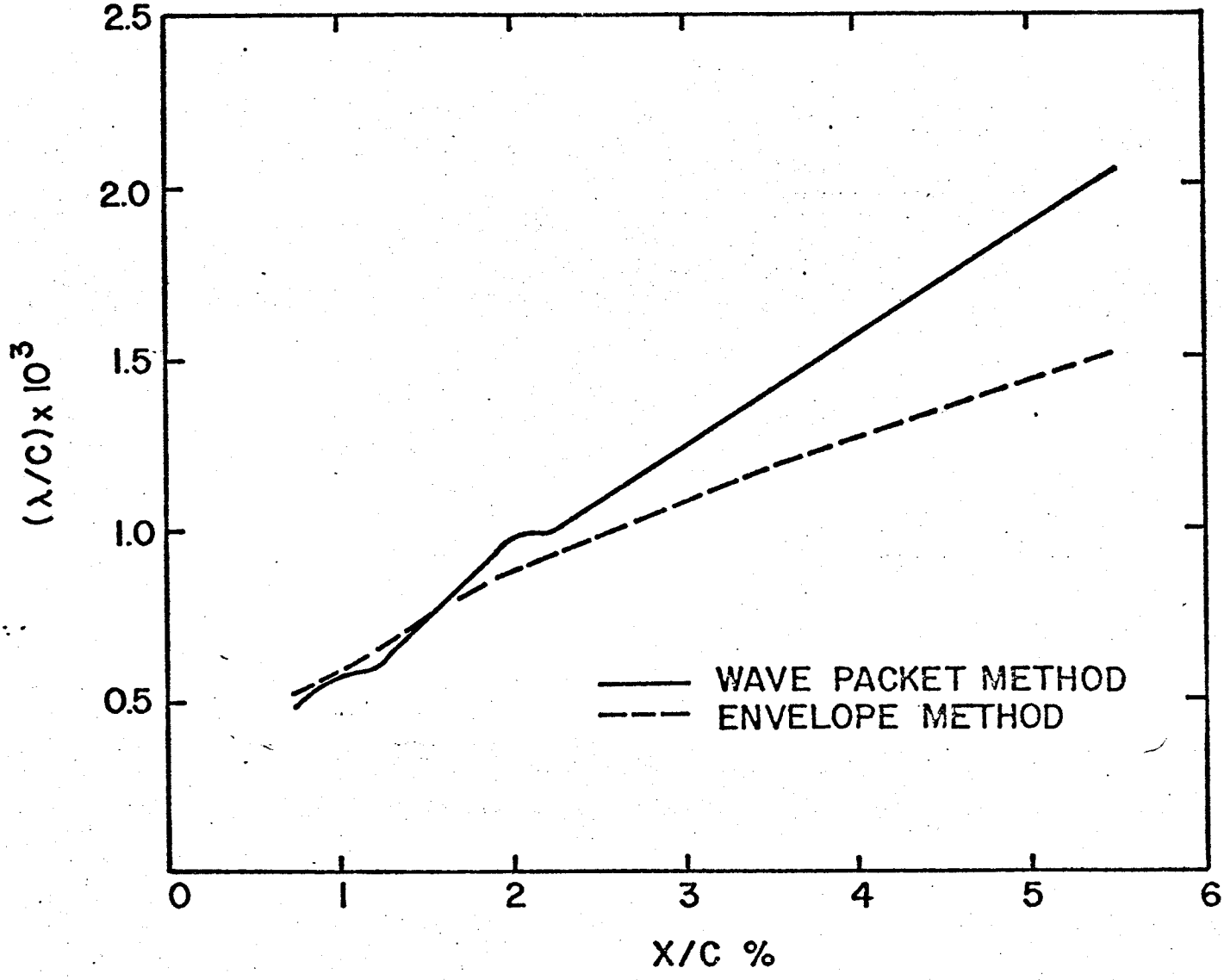
2.5
2.0
1.5
1.0
0.5
(λ/C) x 10^3
0
1
2
3
4
5
6
X/C %
WAVE PACKET METHOD
ENVELOPE METHOD

Figure 4

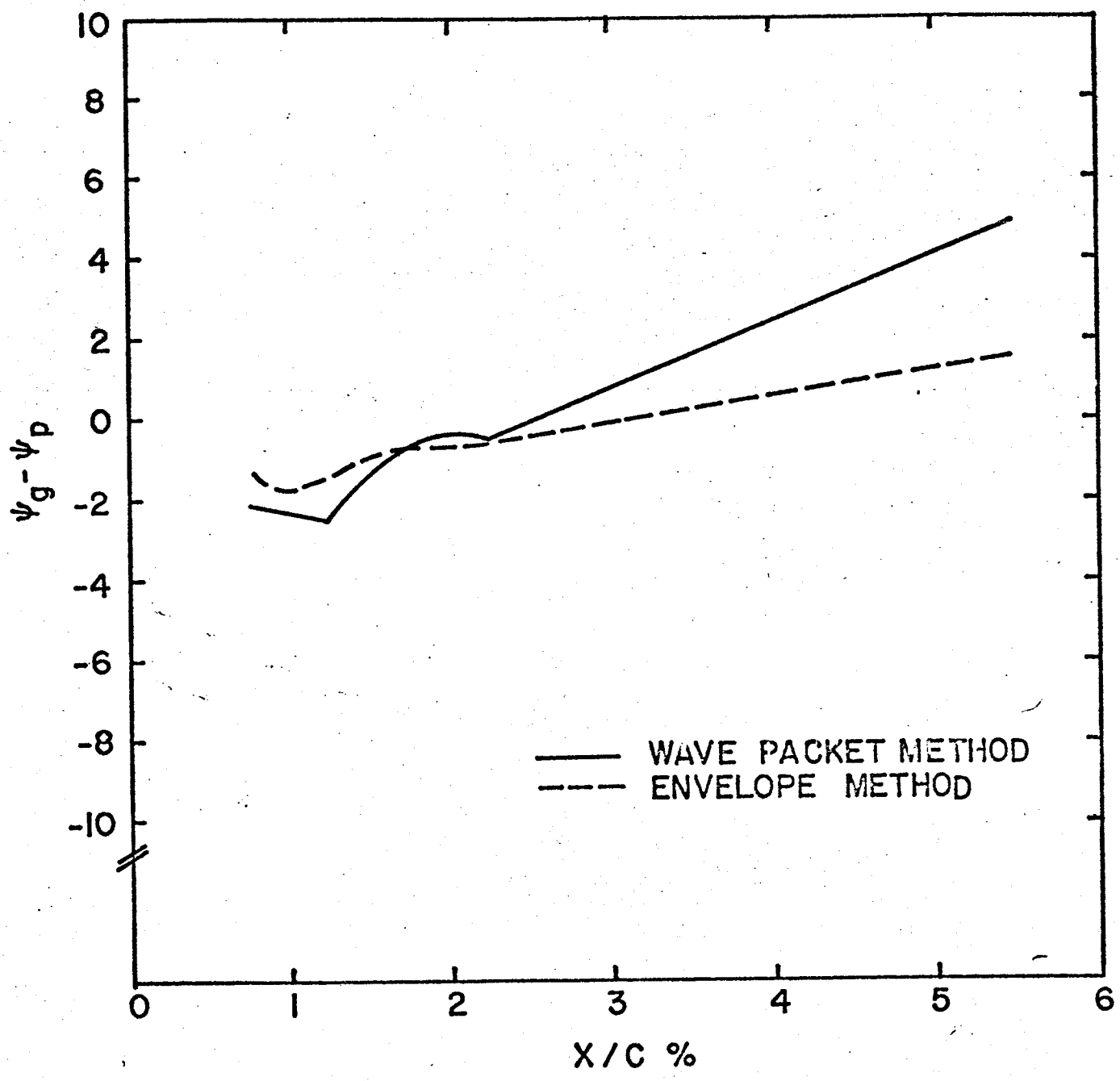
10
8
6
4
2
0
-2
-4
-6
-8
-10
$\psi_g - \psi_p$
0
1
2
3
4
5
6
X/C %
WAVE PACKET METHOD
ENVELOPE METHOD

Figure 5.

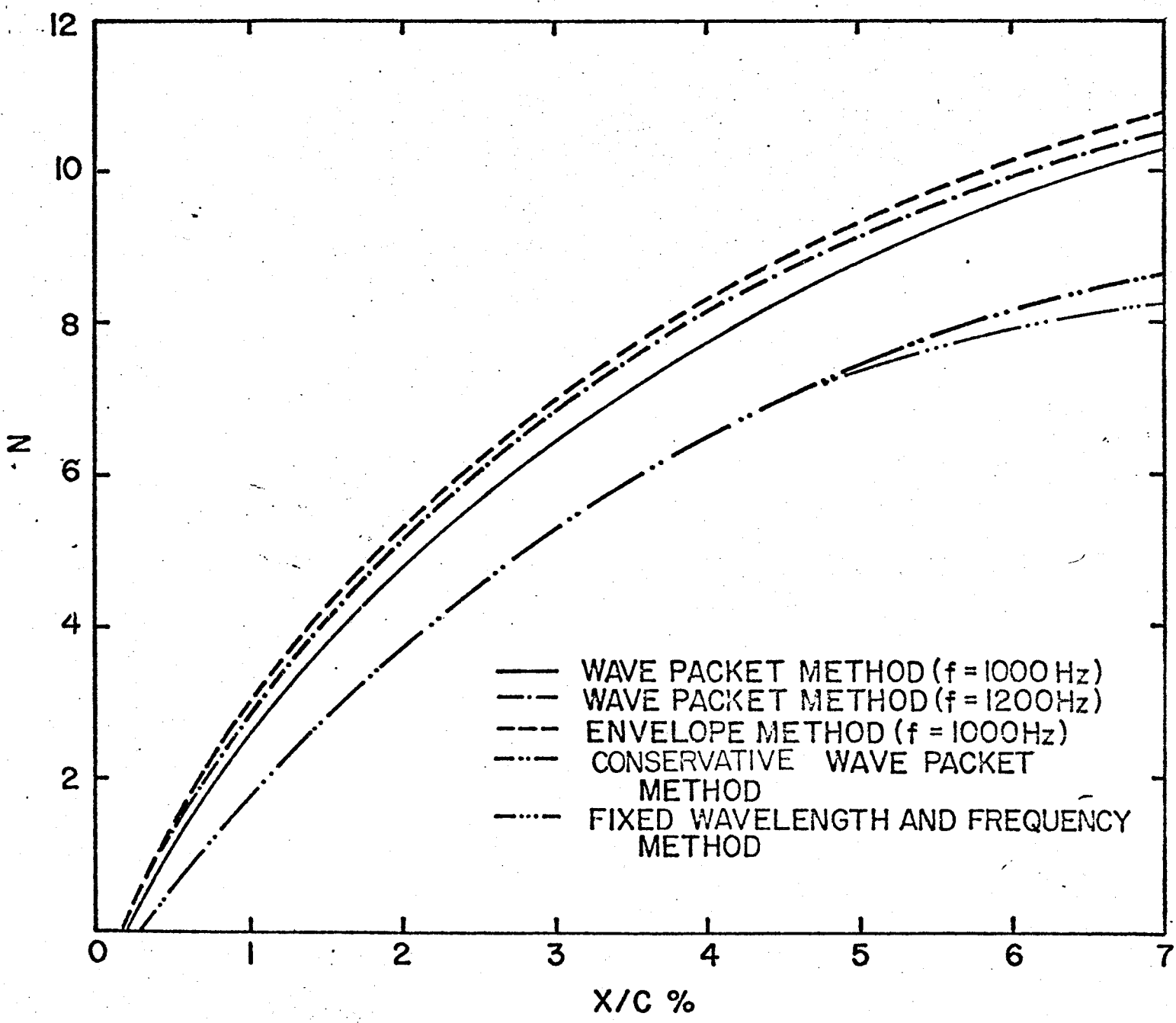
12
10
8
6
4
2
N
0
1
2
3
4
5
6
7
X/C %
WAVE PACKET METHOD (f = 1000 Hz)
WAVE PACKET METHOD (f = 1200Hz)
ENVELOPE METHOD (f = 1000Hz)
CONSERVATIVE WAVE PACKET METHOD
FIXED WAVELENGTH AND FREQUENCY METHOD

Figure 6.

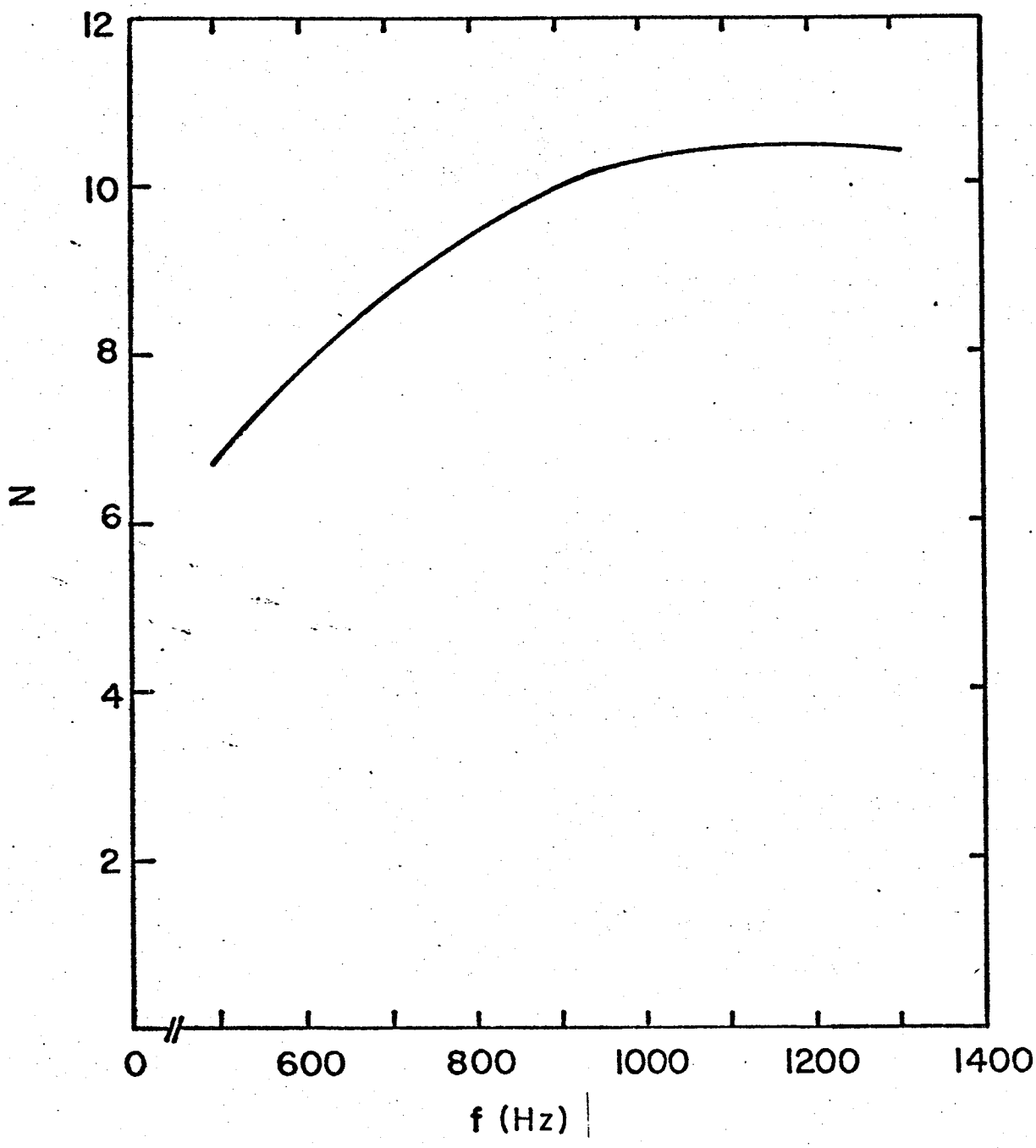

Figure 7.

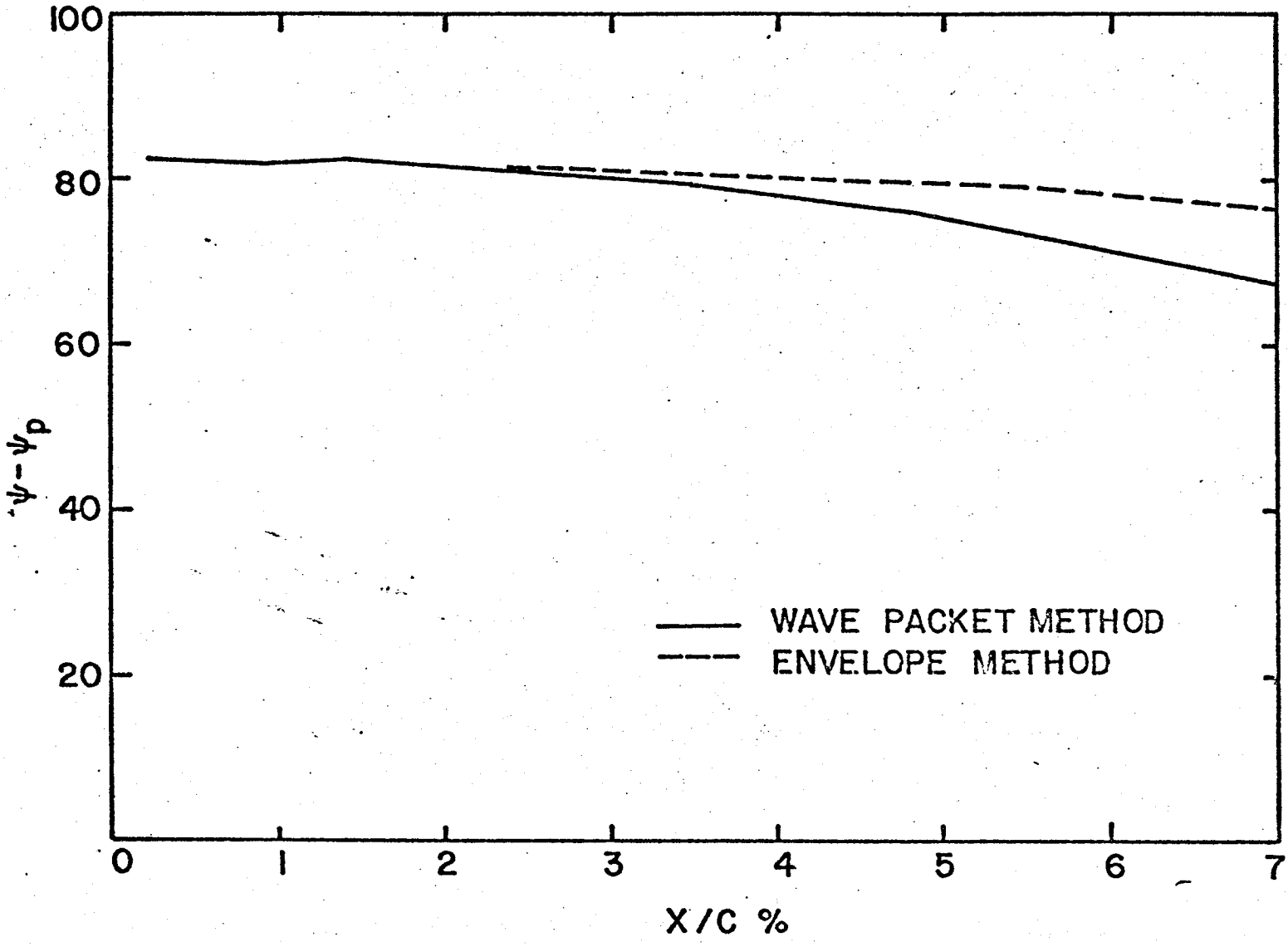
100
80
60
40
20
$\psi - \psi_p$
WAVE PACKET METHOD
ENVELOPE METHOD
0
1
2
3
4
5
6
7
X/C %

Figure 8.

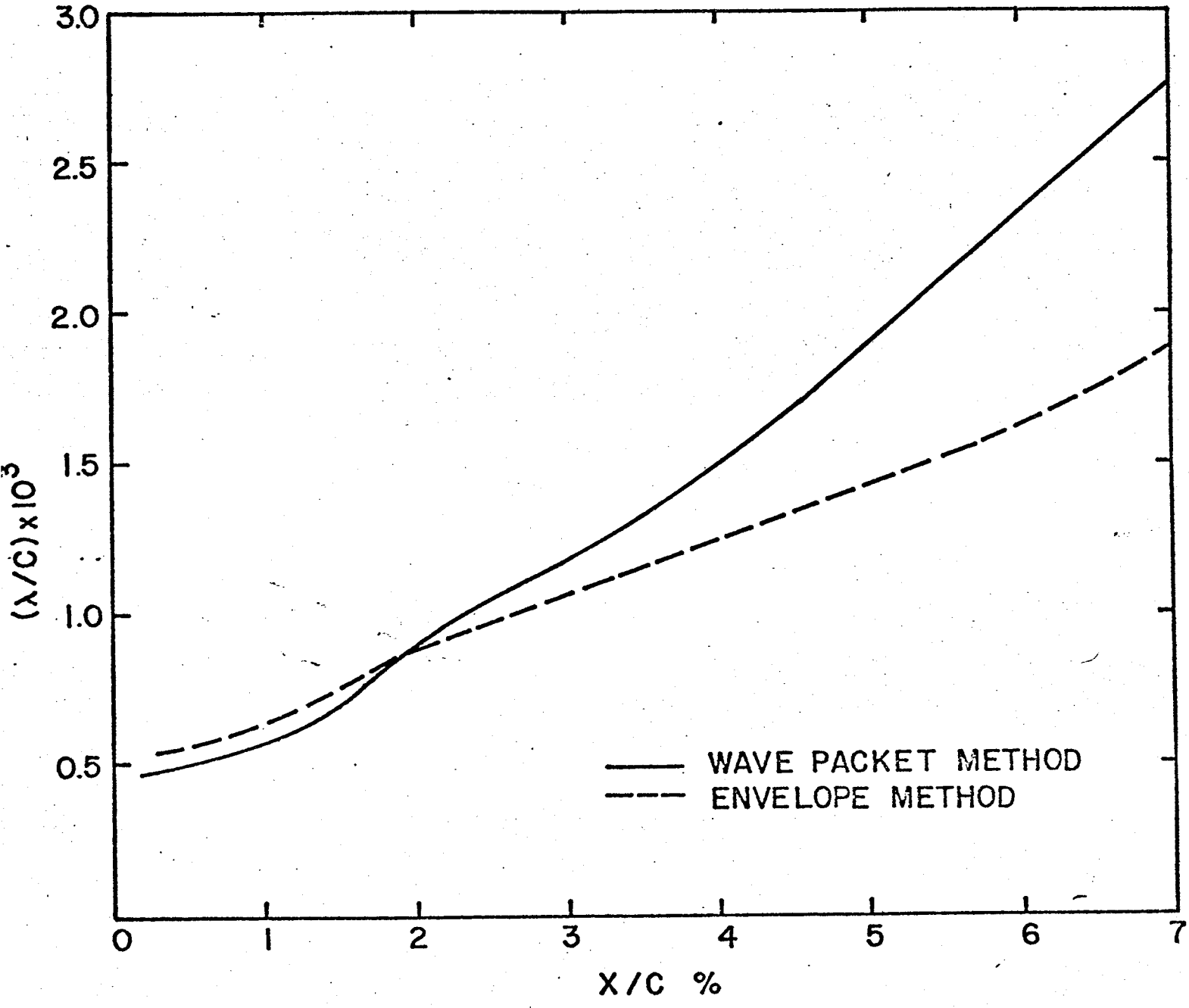
3.0
2.5
2.0
1.5
1.0
0.5
(λ/C)x10^3
0
1
2
3
4
5
6
7
X/C %
WAVE PACKET METHOD
ENVELOPE METHOD

Figure 9.

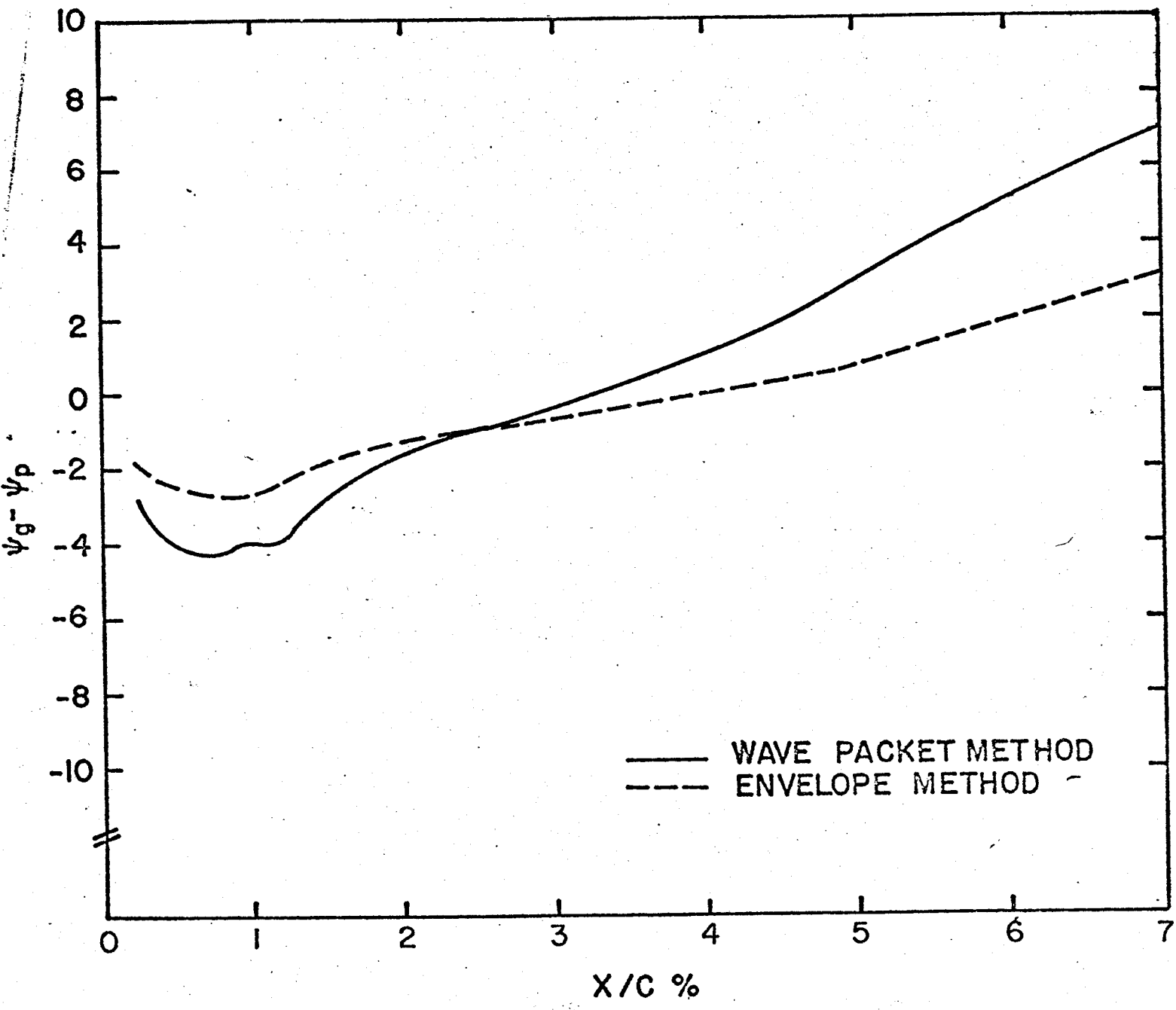
10
8
6
4
2
0
-2
-4
-6
-8
-10
$\psi_g - \psi_p$
0
1
2
3
4
5
6
7
X/C %
WAVE PACKET METHOD
ENVELOPE METHOD

Figure 10.

IV. Instability and Transition in Rotating Disk Flow

ABSTRACT

The stability of three-dimensional rotating disk flow is investigated, including the effects of Coriolis forces and streamline curvature. The results show that the critical Reynolds number for establishment of stationary vortex flow is $R_c = 287$. These vortices spiral outwards at an angle of about 11.2° and transition to turbulence occurs when their total amplification is about e^{11}. We also report new experimental results on the spatial growth rates of the stationary vortices. It is shown that our analysis gives growth rates that compare much better with the experimental results than do results obtained using the Orr-Sommerfeld equation. Our calculations also indicate the existence of weakly unstable propagating (Type II) modes at low Reynolds numbers ($R_c = 49$).

1. INTRODUCTION

The prediction of transition in three dimensional boundary layers [1-3] is a subject of both fundamental and practical importance in fluid mechanics. Practical interest in the subject centers on the design of laminar flow control (LFC) wings that promise significant improvement in airplane fuel efficiency. At present, the most useful tool for transition prediction in such flows is the so-called e^N method [4]. Hefner and Bushnell [5] and Malik and Orszag [6] show that the exponent N (called the N factor) is of the order 7-11 when transition occurs on LFC swept wings.

The instability mechanism exhibited in the leading edge region of a swept wing is similar to that found in the boundary layer on a rotating disk, since both have mean cross flow profiles with inflection points. More details on the similarities between the two flows is given in Ref. [7]. However, the rotating disk flow is more convenient to study in view of von Karman's exact steady solution of the Navier-Stokes equations [8].

Using hot-wire techniques, Smith [9] observed that sinusoidal disturbances appear in a rotating disk boundary layer at sufficiently large Reynolds number. About 32

oscillations were observed within a disk rotation period and analysis indicated that the disturbances propagate at an angle of about 14° relative to the outward drawn radius (where the direction of disk rotation defines positive angles). Later, in a remarkable study using the china-clay technique, Gregory et al [10] observed about 30 vortices over the disk spiraling outwards at an angle of about 14° (that is, their normals make an angle of about 14° with the outward drawn radius). These vortices, which appeared stationary relative to the rotating frame of the disk, were first observed at a Reynolds number $R_C \approx 430$ [where R is defined after (2.14) below]. Transition to turbulence occurred at $R_T \approx 530$. The overall conclusions drawn by Gregory et al have been confirmed in later investigations [11,12]. It has been found that there are about 30 stationary vortices whose normals make an angle of 11° - 14° with the radius. However, there seems to be considerable controversy over the value of the critical Reynolds number which in our view can be attributed to the measurement techniques used. Further, at low Reynolds numbers, Fedorov et al [13] observed only 14-16 vortices with normals lying at an angle of about 20°.

Stuart [10] analysed the linear, inviscid stability of rotating disk flow. However, the neglect of

viscosity resulted in the prediction of 113-140 vortices over the disk which is about four times larger than the observed value. Brown [14] extended Stuart's work to the viscous case by applying the Orr-Sommerfeld equation to disk flow. Using temporal instability theory, Brown found $R_c \simeq 178$, which is much less than the observed value. Recently, Cebeci and Stewartson [3] solved the Orr-Sommerfeld equation for rotating disk profiles using spatial stability theory and found $R_c \simeq 170$. They also suggested that wave packets propagate in three dimensional flows in such a way that $d\alpha/d\beta$ is real. Using this condition, Cebeci and Stewartson correlated transition using the e^N method and found the N factor at transition ($R_T = 510$) to be about 20 which is much higher than that found for LFC wings ([5],[6]). Bushnell (private communication) argues that a higher N factor may be required for transition in disk flow than on LFC wings because the boundary layer is rotating with the disk while the external disturbances in the surroundings are not. Consequently, there is no direct coupling between the external disturbances and the instability waves in the rotating disk boundary layer.

The Orr-Sommerfeld stability equation neglects the effects of Coriolis forces, streamwise curvature, and nonparallel flow. In Ekman layer flow, Lilly [15] has shown that the Coriolis force has a significant effect on

stability at low Reynolds numbers. Lilly showed that the critical Reynolds number for appearance of stationary vortices is higher ($R_c \simeq 115$) when the Coriolis force is included in the analysis than when it is neglected ($R_c \simeq 85$). In addition to the stationary vortices, he showed the existence of a parallel instability caused by the Coriolis force at much lower Reynolds numbers. Such an instability mechanism was also observed in the Ekman layer experiments of Faller and Kaylor [16] and Tatro and Mollo-Christensen [17]. The Ekman layer and the rotating disk are similar in that both are three-dimensional boundary layer flows in which rotation plays a significant role. Lilly's results suggest that the inclusion of the Coriolis force in the stability analysis of rotating disk flow may also lead to a higher critical Reynolds number for stationary vortices which is in better agreement with observations.

In this section we present a stability analysis of rotating disk flow in which the effects of Coriolis force and streamline curvature are included. The resulting sixth order system is solved numerically by a Chebyshev spectral method [18-19]. We also follow the evolution of the disturbance modes using the envelope method [1,6] and calculate the N factor at transition.

The work of Kobayashi et al [12], which appeared during the final stages of the present study, also includes the effects of the Coriolis force and streamline curvature. We will comment on this work in Sec. 6.

We also report results of an experimental investigation of rotating disk flow in which the growth rates of the boundary layer disturbances were measured using a hot-wire probe. While only limited experimental results are now available, the agreement with the present theoretical analysis seems encouraging. We know of no previous experimental study in which growth rates were measured.

2. THEORETICAL ANALYSIS

Consider an infinite plane disk rotating about its axis with angular velocity Ω . We take cylindrical coordinates r^*,θ,z^* with $z^* = 0$ being the plane of the disk. Assuming the fluid to lie in the half-space $z^* > 0$, the governing dynamical equations are, in the rotating coordinate system,

$$\frac{\partial u^*}{\partial t^*} + u^* \frac{\partial u^*}{\partial r^*} + \frac{v^*}{r^*} \frac{\partial u^*}{\partial \theta} + w^* \frac{\partial u^*}{\partial z^*} - \frac{v^{*2}}{r^*} = - \frac{1}{\rho} \frac{\partial p^*}{\partial r^*}$$

$$+ \nu\left(\frac{\partial^2 u^*}{\partial r^{*2}} + \frac{1}{r^{*2}} \frac{\partial^2 u^*}{\partial \theta^2} + \frac{\partial^2 u^*}{\partial z^{*2}} + \frac{1}{r^*} \frac{\partial u^*}{\partial r^*}\right.$$

$$\left. - \frac{2}{r^{*2}} \frac{\partial v^*}{\partial \theta} - \frac{u^*}{r^{*2}}\right) + 2\Omega v^* + r^* \Omega^2 \qquad (2.1)$$

$$\frac{\partial v^*}{\partial t^*} + u^* \frac{\partial v^*}{\partial r^*} + \frac{v^*}{r^*} \frac{\partial v^*}{\partial \theta} + w^* \frac{\partial v^*}{\partial z^*} + \frac{u^* v^*}{r^*} = - \frac{1}{\rho r^*} \frac{\partial p^*}{\partial \theta}$$

$$+ \nu\left(\frac{\partial^2 v^*}{\partial r^{*2}} + \frac{1}{r^{*2}} \frac{\partial^2 v^*}{\partial \theta^2} + \frac{\partial^2 v^*}{\partial z^{*2}} + \frac{1}{r^*} \frac{\partial v^*}{\partial r^*} + \frac{2}{r^{*2}} \frac{\partial u^*}{\partial \theta} - \frac{v^*}{r^{*2}}\right)$$

$$- 2\Omega u^* \qquad (2.2)$$

$$\frac{\partial w^*}{\partial t^*} + u^* \frac{\partial w^*}{\partial r^*} + \frac{v^*}{r^*} \frac{\partial w^*}{\partial \theta} + w^* \frac{\partial w^*}{\partial z^*} = - \frac{1}{\rho} \frac{\partial p^*}{\partial z^*}$$

$$+ \nu \left(\frac{\partial^2 w^*}{\partial r^{*2}} + \frac{1}{r^{*2}} \frac{\partial^2 w^*}{\partial \theta^2} + \frac{\partial^2 w^*}{\partial z^{*2}} + \frac{1}{r} \frac{\partial w^*}{\partial r^*}\right) \quad (2.3)$$

$$\frac{\partial u^*}{\partial r^*} + \frac{1}{r^*} \frac{\partial v^*}{\partial \theta} + \frac{\partial w^*}{\partial z^*} + \frac{u^*}{r^*} = 0, \quad (2.4)$$

where (u^*,v^*,w^*) are the velocity components in the (r^*,θ,z^*) directions, respectively, p^* is the pressure, ρ is the density, and ν is the kinematic viscosity.

Von Karman's exact solution of (2.1) - (2.4) for steady laminar rotating disk flow is obtained as follows [8]. Let $\bar{u},\bar{v},\bar{w}$, and $\bar{p}$ denote the steady state values of u^*,v^*,w^*, and p^* respectively. Defining

$$\bar{u} = r^*\Omega F(z), \ \bar{v} = r^*\Omega G(z), \ \bar{w} = \sqrt{\nu\Omega} H(z), \ \bar{p} = \rho\nu\Omega p(z), \quad (2.5)$$

where $z=z^*\sqrt{\Omega/\nu}$ then the Navier-Stokes equations (2.1) - (2.4) reduce to the following equations for F,G,H and P:

$$F^2 - (G+1)^2 + F'H - F'' = 0 \quad (2.6)$$

$$2F(G+1) + G' H - G'' = 0 \quad (2.7)$$

$$P' + HH' - H'' = 0 \tag{2.8}$$

$$2F + H' = 0 \tag{2.9}$$

where the prime denotes differentiation with respect to z. The boundary conditions are

$$\begin{aligned} &F = 0, \quad G = 0, \quad H = 0 \quad \text{at} \quad z = 0 \\ &F = 0, \; G = -1 \quad \text{for} \quad z \to \infty \end{aligned} \tag{2.10}$$

Now we study the evolution of infinitesimal small disturbances imposed on the steady flow governed by Eqs. (2.5) - (2.9). Let r_e^* be the radial location near which the analysis is to be made. Using $r_e^*\Omega$ as the reference velocity, $\delta^* = \sqrt{\nu/\Omega}$ as the reference length, and $\rho r_e^2 \Omega^2$ as the reference pressure, the perturbed nondimensional velocities u,v,w and pressure p can be written as

$$u(r,\theta,z,t) = \frac{r}{R} F(z) + \tilde{u}(r,\theta,z,t) \tag{2.11}$$

$$v(r,\theta,z,t) = \frac{r}{R} G(z) + \tilde{v}(r,\theta,x,t) \tag{2.12}$$

$$w(r,\theta,z,t) = \frac{1}{R} H(z) + \tilde{w}(r,\theta,z,t) \tag{2.13}$$

$$p(r,\theta,z,t) = \frac{1}{R^2} P(z) + \tilde{p}(r,\theta,z,t) \tag{2.14}$$

Here the nondimensional radius is $r = r^*\sqrt{\Omega/\nu}$, the Reynolds number is $R = r_e^* \sqrt{\Omega/\nu}$, and r_e^* corresponds to $r = R$.

Substituting Eqs. (2.11) - (2.14) in the Navier-Stokes equations (2.1) - (2.4) and linearizing with respect to the perturbations gives:

$$\frac{\partial \tilde{u}}{\partial t} + \frac{r}{R} F \frac{\partial \tilde{u}}{\partial r} + \frac{G}{R} \frac{\partial \tilde{u}}{\partial \theta} + \frac{H}{R} \frac{\partial \tilde{u}}{\partial z} + \frac{F}{R} \tilde{u} - \frac{2}{R} (G+1) \tilde{v} + \frac{r}{R} F' \tilde{w}$$

$$= - \frac{\partial \tilde{p}}{\partial r} + \frac{1}{R} \left[\frac{\partial^2 \tilde{u}}{\partial r^2} + \frac{1}{r^2} \frac{\partial^2 \tilde{u}}{\partial \theta^2} + \frac{\partial^2 \tilde{u}}{\partial z^2} + \frac{1}{r} \frac{\partial \tilde{u}}{\partial r} - \frac{2}{r^2} \frac{\partial \tilde{v}}{\partial \theta} - \frac{\tilde{u}}{r^2}\right] \tag{2.15}$$

$$\frac{\partial \tilde{v}}{\partial t} + \frac{r}{R} F \frac{\partial \tilde{v}}{\partial r} + \frac{G}{R} \frac{\partial \tilde{v}}{\partial \theta} + \frac{H}{R} \frac{\partial \tilde{v}}{\partial z} + \frac{F}{R} \tilde{v} + \frac{2}{R} (G+1) \tilde{u} + \frac{r}{R} G' \tilde{w}$$

$$= - \frac{1}{r} \frac{\partial \tilde{p}}{\partial \theta} + \frac{1}{R} \left[\frac{\partial^2 \tilde{v}}{\partial r^2} + \frac{1}{r^2} \frac{\partial^2 \tilde{v}}{\partial \theta^2} + \frac{\partial^2 \tilde{v}}{\partial z^2} + \frac{1}{r} \frac{\partial \tilde{v}}{\partial r} + \frac{2}{r^2} \frac{\partial \tilde{u}}{\partial \theta} - \frac{\tilde{v}}{r^2}\right] \tag{2.16}$$

$$\frac{\partial \tilde{w}}{\partial t} + \frac{r}{R} F \frac{\partial \tilde{w}}{\partial r} + \frac{G}{R} \frac{\partial \tilde{w}}{\partial \theta} + \frac{H}{R} \frac{\partial \tilde{w}}{\partial z} + \frac{H'}{R} \tilde{w}$$

$$= - \frac{\partial \tilde{p}}{\partial z} + \frac{1}{R} \left[\frac{\partial^2 \tilde{w}}{\partial r^2} + \frac{1}{r^2} \frac{\partial^2 \tilde{w}}{\partial \theta^2} + \frac{\partial^2 w}{\partial z^2} + \frac{1}{r} \frac{\partial \tilde{w}}{\partial r}\right] \tag{2.17}$$

$$\frac{\partial \tilde{u}}{\partial r} + \frac{1}{r}\frac{\partial \tilde{v}}{\partial \theta} + \frac{\partial \tilde{w}}{\partial z} + \frac{\tilde{u}}{r} = 0 \qquad (2.18)$$

The boundary conditions are that $\tilde{u},\tilde{v}$, and $\tilde{w}$ vanish at $z = 0,\infty$.

For $R>>1$, the system (2.15) - (2.18) may be consistently approximated by replacing factors of r by R and neglecting terms of order R^{-2} and smaller. The replacement of r by R at this stage of the calculation implies that we neglect some nonparallel flow effects. These effects are now under study. The neglect of terms of order R^{-2} and smaller has little effect on the results discussed below, as we verified by computations in which they were included.

Replacing factors of r by R in (2.15) - (2.18) gives a set of equations that are separable in r,θ,t so that the perturbation quantities may be assumed to have the form

$$(\tilde{u},\tilde{v},\tilde{w},\tilde{p}) = (f(z),h(z),\phi(z),\pi(z))e^{i(\alpha r+\beta R\theta-\omega t)} \qquad (2.19)$$

With this assumption, Eqs. (2.15) - (2.18) become (not yet dropping terms of order R^{-2})

$$i(\alpha F+\beta G-\omega)f+F'\phi + i\alpha\pi = \frac{1}{R}[f''-\lambda^2 f - Ff + 2(G+1)h - Hf'] + \frac{1}{R^2}[i\alpha f - 2i\beta h] - \frac{1}{R^3} f \qquad (2.20)$$

$$i(\alpha F + \beta G-\omega)h + G'\phi + i\beta\pi = \frac{1}{R}\,[h''-\lambda^2 h-Fh-2(G+1)f-Hh'] + \frac{1}{R^2}\,[i\alpha h + 2i\beta f] - \frac{1}{R^3}\,h \qquad (2.21)$$

$$i(\alpha F + \beta G-\omega)\,\phi + \pi' = \frac{1}{R}\,[\phi''-\lambda^2\phi-H\phi'-H'\phi] + \frac{i}{R^2}\,\alpha\,\phi \qquad (2.22)$$

$$(i\alpha+\frac{1}{R})f + i\beta h + \phi' = 0 \qquad (2.23)$$

where $\lambda^2 = \alpha^2 + \beta^2$.

Eliminating π from (2.20) - (2.22) by means of (2.23) gives, neglecting terms of order R^{-2} and smaller,

$$\frac{1}{R}\,[i(D^2-\lambda^2)(D^2-\bar{\lambda}^2) + R(\alpha F+\beta G-\omega)(D^2-\bar{\lambda}^2) - R(\bar{\alpha}F''+\beta G'')-iHD(D^2-\bar{\lambda}^2) - iH'(D^2-\bar{\lambda}^2) - iFD^2]\phi+\frac{1}{R}[2(G+1)D + 2G']\,\eta = 0 \qquad (2.24)$$

$$\frac{1}{R}[2(G+1)D-iR(\alpha G'-\beta F')]\,\phi +\frac{1}{R}[i(D^2-\lambda^2) + R(\alpha F+\beta G-\omega) - iHD - iF]\eta = 0 \qquad (2.25)$$

and where $D = d/dz$, $\bar{\alpha} = \alpha - i/R$, $\bar{\lambda}^2 = \alpha\bar{\alpha} + \beta^2$ and $\eta = \alpha h - \beta f$ is proportional to the z-component of the perturbation vorticity. The final result (2.24) - (2.25) is a consistent set of stability equations valid to order R^{-1}.

The boundary conditions for the sixth order system (2.24) - (2.25) are

$$\phi(0) = \phi'(0) = \eta(0) = 0$$

(2.26)

$$\phi(\infty) = \phi'(\infty) = \eta(\infty) = 0$$

Note that if the Coriolis force and streamline curvature effects are neglected, the above system reduces to the fourth-order Orr-Sommerfeld equation;

$$[i(D^2-\lambda^2)^2 + R(\alpha F+\beta G-\omega)(D^2-\lambda^2) - R(\alpha F''+\beta G'')]\phi = 0$$

(2.27)

In Sec. 6, we report numerical results for both the sixth order system (2.24) - (2.25) and the fourth order equation (2.27) in order to study the effect of Coriolis force and streamline curvature terms on the stability of flow due to a rotating disk.

3. NUMERICAL METHOD

We solve the Orr-Sommerfeld equation (2.27) in the computer code SALLY [1] by using a spectral method based on Chebyshev polynomials[18-19].Here we extend the method to solve the sixth order system (2.24) - (2.26).

The boundary layer coordinate z, $0 \leq z < \infty$ is mapped into the finite interval $-1 \leq \xi < 1$ by the algebraic mapping

$$\xi = 2 \frac{z}{z+L} - 1 \tag{3.1}$$

where L is a scale parameter chosen to optimize the distribution of points in ξ. Then $\phi(z)$ and $\eta(z)$ are approximated as the finite Chebyshev polynomial series

$$\phi(z) = \sum_{n=0}^{M} a_n T_n(\xi) \tag{3.2}$$

$$\eta(z) = \sum_{n=0}^{M} b_n T_n(\xi) \tag{3.3}$$

Substituting (3.2), (3.3) in (2.24) - (2.26) and collocating [19] at the discrete points $\xi_j = \cos \pi_j/M$ $(0 \leq j \leq M)$ gives the algebraic eigenvalue problem,

$$A \begin{Bmatrix} a_n \\ b_n \end{Bmatrix} = \omega B \begin{Bmatrix} a_n \\ b_n \end{Bmatrix} \tag{3.4}$$

where A and B are $2(M+1) \times 2(M+1)$ matrices. The eigenvalue problem (3.4) is solved globally (if a guess for an eigenvalue is not available) by a generalized QR algorithm or locally (if a good guess is available) by inverse Rayleigh iteration [20]. The resulting scheme is very efficient and accurate. In the present calculations the optimum value of the scaling parameter L was found to be about 1.8. In most of the calculations reported below, $M = 34$ so 35 Chebyshev polynomials were used.

The accuracy of the method was tested in several ways. First, the number of retained polynomials, $M + 1$ was varied to check the accuracy of the eigenvalues and eigenfunctions. Then, calculations were made for the stability of Ekman flow. Comparisons were made with the results obtained by Lilly [15] for $R = 65$, 110, 150, 300 and 500 with good agreement.

For rotating disk flow, the global method gives only one unstable eigenvalue [$\mathrm{Im}(\omega) > 0$] for $R \gtrsim 150$ that is insensitive to M. However, spurious unstable modes appear for lower R which are discarded as unphysical because they are very sensitive to M.

4. TRANSITION PREDICTION USING THE e^N METHOD

In three dimensional flow, the dispersion relation is given by the complex relation

$$\omega = \omega(\alpha,\beta) \tag{4.1}$$

where α,β, and ω are, in general, complex. Therefore, there are four arbitrary real parameters among α,β and ω. There are several ways [6] to remove this arbitrariness. In the present study we employ the envelope method [1]. Here the four conditions are obtained by using temporal stability theory [in which $Im(\alpha) = Im(\beta) = 0$] and by maximizing $Im(\omega)$ with respect to α,β at fixed $Re(\omega)$. The N factor is then given by

$$N = \int_{s_C}^{s_T} \frac{Im(\omega)}{|\, Re(\vec{v}_g)\,|}\, ds \tag{4.2}$$

where $\vec{v}_g = (\omega_\alpha, \omega_\beta)$ is the (complex) group velocity and s is the arc length along the curve whose tangent is the real part of the group velocity. Noting that

$$ds = \frac{dR}{Re(\omega_\alpha)} \sqrt{(Re(\omega_\alpha))^2 + (Re(\omega_\beta))^2} = \frac{dR}{Re(\omega_\alpha)} \left|\, Re(\vec{v}_g) \,\right| .$$

Eq. (4.2) can be written as

$$N = \int_{R_C}^{R_T} \frac{Im(\omega)}{Re(\omega_\alpha)}\, dR \tag{4.3}$$

Here the subscripts C and T indicate critical (linearly unstable) and onset of transition, respectively.

5. EXPERIMENTAL STUDY

An experimental program was established to quantitatively study the flat rotating disk flow with particular attention given to measurement of the growth of boundary layer disturbances as a function of Reynolds number. The experimental set-up is described along with the measurement techniques. Measured mean velocity profiles are compared with the exact solution and an analysis of mechanical disk vibrations is presented.

Rotating Disk Apparatus

The experimental apparatus is shown schematically in Figure (1). A 457 mm diameter, 12.7 mm thick Plexiglass disk was attached to a 50.8 mm diameter aluminum shaft by means of two parallel aluminum mounting disks. Shim stock inserted at various circumfrential locations between the mounting disks was used to control alignment of the Plexiglass disk and to compensate for asymetrical flexure of the Plexiglass introduced by mounting stresses. The drive shaft was inserted between two pre-mounted, self-aligning ball bearings and was driven by a 1/4 Hp, 1725 RPM AC motor through a 2:1 belt and pulley speed reduction

system. The test surface of the Plexiglass was hand ground on a surface table to a flat, near-gloss finish. Static measurements with a dial indicator showed the disk to have a +/- 0.008 mm deviation from a flat plane. The assembly was housed in a 1.8 m cubical box with an open front. The radial flow at the disk periphery was ducted behind the disk by placing a 1.8 m square cover several boundary layer thicknesses in front of the disk with the test surface exposed by a large hole of slightly smaller diameter than the disk.

Hot Wire System

A single constant temperature, linearized hot wire was used for all measurements. Wollostan Pt-10Rh 0.0025 mm wire with an active length of 1.0 mm was used. Calibration was done in the entry region of a duct flow at room temperature with the wire and prongs in the same orientation with respect to the flow as during the boundary layer measurements. For measurements, the wire was placed parallel to the disk surface with the wire axis along a radius. The wire was fixed in space while the disk boundary layer rotated past it.

Response of a Single Hot Wire in a Three-Dimensional Disk Flow

A single hot wire parallel to the disk surface with the wire axis along a radius will indicate a mean velocity having the magnitude of the vector composed of the axial and tangential

components of the flow. In non-dimensional terms, the ratio of this magnitude to that of the tangential component is given by:

$$\sqrt{1 + \left(\frac{1}{R}\frac{H}{(G+1)}\right)^2} \simeq 1 + \frac{1}{2}\left(\frac{1}{R}\frac{H}{(G+1)}\right)^2 \qquad (5.1)$$

Provided that the term $\frac{1}{2}\left(\frac{1}{R}\frac{H}{(G+1)}\right)^2$ is small, the hot wire will provide an excellent estimate of the actual tangential velocity distribution. For the current experiment, the minimum value of R was 125. For this case, Eq. (5.1) shows that the discrepancy between the actual tangential velocity and the quantity measured by the hot wire is less than one percent for all $G>-0.95$ or over approximately the inner 80% of the boundary layer thickness. Since the outer region of the boundary layer is characterized by extremely low velocities for which measurements are inherently inaccurate, no corrections were made to the measured profiles.

To verify that a well behaved disk flow was present, the mean tangential velocity distribution was measured at several Reynolds numbers. Results are shown in Figure 2. The profiles for $R = 251,\ 374$ are in good agreement with the exact solution (see Eqs. (2.6) - (2.10)). The distribution at higher Reynolds numbers Reynolds numbers is expected to deviate from the exact solution due to the presence of the highly amplified stationary vortices. Even

then, the effect of the stationary vortices on the mean flow is found to be largely confined to the outer region of the boundary layer.

Measurements of the fluctuating components of the flow were made in order to determine the growth rate of the stationary disk disturbances. The theoretical formulation of the problem assumes the same growth rate $\text{Im}\,\omega$ for the three velocity components. Therefore, any arbitrary combination of the components will also have the same growth rate. The single hot wire responds to the axial and tangential components of the flow. The growth exhibited by the hot wire can, therefore, be used for comparisons with theoretical predictions. The experimental growth rates will be compared with the theoretical predictions in the next Section.

Mechanical Disk Vibrations

Due to the large velocity gradient near the disk surface, any displacement of the disk surface relative to the hot wire will modulate the anemometer output. Low frequency displacements due to the static or dynamic deviation of the disk from a flat plane are easily recognizable since they modulate the signal at a frequency corresponding to some small multiple of rotational frequency. Figure 3 shows that static deviation of the disk consists of four undulations in the surface. Figure 4 is a plot of the hot wire output at $R = 457$ and $G = -0.5$ for one revolution of the disk. The signal was bandpass filtered in the range

250 < f < 600 hz, however, the envelope of the signal roughly corresponds to the disk surface undulations and thus partially accounts for the modulated output.

Other sources of vibrations were the ball bearings, drive system, and structural resonances of the disk support stand. These vibrations were of very small amplitude and were noted to occur in the same frequency range as the passing stationary vortices. These vibrations are critical when measuring disturbances in regions of low fluctuation intensity. To show the effect of these vibrations, the displacement of the center of the disk was monitored with a proximeter and the spectrum of these vibrations was compared to that of the hot wire output at $R = 125$ and $G = -0.5$. The vibration data was converted to apparent velocity fluctuations by using the calculated $\bar{v}(z)$ velocity gradient at the hot wire location. It was assumed that the vibrations at the center of the disk were very similar to those at the hot wire location. Results are shown in Figure 5 . (Both sets of data were bandpass filtered in the range $250<f<600$ Hz). The plots show that the hot wire output can be largely attributed to the disk vibrations. Since the vibrations were in the same frequency range as the stationary vortices, the hot wire data at low intensities could not be used to indicate the amplification rate of the stationary disk disturbances. This also eliminated the possibility of experimentally determining the critical Reynolds number for the stationary disturbances.

6. RESULTS AND DISCUSSION

Critical and Transition Reynolds Numbers

Some of the available experimental data for critical and transition Reynolds numbers are given in Table 1. It is apparent that there is considerable variation of the observed critical point. We believe that the variation can be attributed to the different measurement techniques used in the experiments. Using the Orr-Sommerfeld equation, we obtained a critical Reynolds number $R_C \simeq 171$ which is in good agreement with the theoretical results of Brown [14] and Cebeci and Stewartson [3] but is considerably less than the observed values. The value of the critical Reynolds number for stationary vortices is significantly improved when the effects of Coriolis forces and streamline curvature are included. Our calculated critical Reynolds number of 287 is in excellent agreement with the value of 297 obtained by Kobayashi et al [12] using hot-wire techniques. Kobayashi et al [12] also performed a theoretical analysis in which some of the effects of Coriolis forces and streamline curvature were considered. They calculated a critical Reynolds number of 261.

In order to correlate transition using stability theory, one has to know the experimental location of the onset of transition. The transition Reynolds numbers usually given for experiments (see Table 1) are the locations where transition is complete.

Gregory and Walker [21] showed that, for a slitted rotating disk, the transition region is composed of two subregions: (i) a vortex region and (ii) an intermediate turbulent region where the intermittancy factor γ varies from 0 to 1. Stability theory is only applicable up to the point where the first turbulence burst appears ($\gamma = 0$). Gregory and Walker obtained $R = 505$ and 524 for $\gamma = 0$ and $\gamma = 1$, respectively. Chin and Litt [23], using an electrochemical technique, observed that the transition was complete at $R = 592$. They also observed that the vortices start breaking down into turbulence at $R_T = 510$. We believe that this result should be taken as the relevant location for the onset of transition for the purposes of comparison with stability theory. Further evidence that the initiation of transition occurs at $R_T \simeq 510$ is provided by Kobayashi et al who observe that the disturbances are non-linear at $R = 500$. Usually the non-linear region is narrow so the onset of transition soon follows. Further, Federov et al [13] observed turbulent flow at $R = 515$. On the basis of all this evidence we take $R_T \simeq 510$ as the location of the onset of transition.

Growth of Infinitesimal Disturbances

Disturbances of all frequencies may be present in natural transition. We follow the evolution of several different modes and the one which gives the highest inte-

grated growth factor is used to correlate transition. Stationary disturbances were found to give the highest N factor for rotating disk flow over all positive real frequencies. Disturbances with negative phase velocities can give slightly higher N factors but they are of no consequence in the process of transition.

It was shown in [6] that envelope method is a reliable tool for transition prediction in three dimensional flows. First, we report calculations using the Orr-Sommerfeld equation. The resulting N factors are compared with those of Cebeci and Stewartson [3] in Figure 6. It is evident that their method predicts $N \simeq 20$ at transition ($R = 510$) while the present (envelope) method gives $N \simeq 22$ at transition. Cebeci and Stewartson [3] used spatial stability theory and in order to remove arbitrariness among the parameters of equation (4.1), they imposed the condition

$$\frac{\partial \alpha_i}{\partial \beta_r} = 0 \qquad (6.1)$$

where $\alpha_i = \mathrm{Im}(\alpha)$, $\beta_r = \mathrm{Re}(\beta)$. In order to simplify their computations, Cebeci and Stewartson assumed that the maximum growth rate at any $R > R_c$ is independent of the growth direction. This condition is not realistic and we believe that had their growth rates been maximized over all possible growth directions their N factor at transition would be in better agreement with the present predictions using the Orr-Sommerfeld equation.

In Fig. 7 we plot calculated temporal growth rates ($\mathrm{Im}(\omega)$) for stationary vortices. It can be seen that the inclusion of streamline curvature and Coriolis forces have a significant stabilizing effect. Calculations with only Coriolis terms (as done by Lilly [15] for Ekman flow) were also made. These results indicate that streamline curvature effects must also be included in order to model properly the physical problem.

Since the instability is spatial in nature, we transform temporal growth rates to spatial growth rates σ using the group velocity transformation

$$\sigma = \frac{\mathrm{Im}(\omega)}{\mathrm{Re}(\omega_\alpha)} \qquad (6.2)$$

The spatial growth rates are plotted in Figure 8 together with experimental data. Except for the data at low fluctuation intensity and for data in the turbulent breakdown region, the agreement with the present stability analysis is good.

Integrated growth rate (N factor) results are presented in Figure 9. The present stability theory gives $N \simeq 10.6$ which is close to the value $N = 9$ for two dimensional flows and is in the range of values found for swept wings [6]. It is apparent that there is a very significant effect on the predicted transition N factor when the effects of Coriolis forces and streamline curvature are included. The resulting N factors are much more reasonable than those obtained by conventional stability theory where only the Orr-Sommerfeld equation is solved.

Also presented in Figure 9 are experimental results for the N factor. The experimental amplification rate of the stationary vortices was determined from the rms spectra of the bandpass filtered hot wire output. The rms voltage in a narrow band centered on the frequency (438 ± 8 Hz) of the stationary vortices being swept past the probe was calculated for each Reynolds number. The N factor was based on this rms level relative to the local disk velocity. Due to the

problem with disk vibrations indicated earlier, it was assumed that $A_0 = 1$ and the resultant data were shifted at constant Reynolds number to match the theoretical growth curve. The data are seen to be in a fair agreement with the present theory over the range $400<R<500$. The significant deviation of the data for $R < 400$ is attributed to disk vibrations. The falling off of the data for $R > 500$ is due to the highly non-linear nature of the flow in this region and breakdown to turbulence.

Although shifting the level of the data because of uncertainty in the value of A_0 can be questioned, the fact that the slope of the experimental curve ($\sigma = dN/dR$) matches the present theory (see Figure 8) in the range $400<R<500$ is very encouraging. With recent advances in rotating equipment technology, it may be feasible to build a disk drive system with low enough vibration amplitudes in the frequency range of interest to allow an experimental estimate of A_0 to be made. Work investigating this possibility is now underway.

The absolute value of the fluctuation intensity is plotted in Figure 10. The intensities for the range in which the growth rate agrees with the theory is seen to be from 0.1% to 10%.

Orientation and Number of Vortices

In the envelope method we maximize growth rates $Im(\omega)$ for stationary vortices over all possible wave angles. We find that the vortex spirals make an angle of 11.2° with the negative of the direction of disk rotation. This is in excellent agreement with the experimental value of 11-14° [10-13].

It can be shown that the number of vortices is given by

$$n = \beta R \tag{6.3}$$

where β is defined in (2.19).

Gregory et al [10] observed about 30 vortices in the range of Reynolds numbers range 430-530. At $R = 430$, we obtain $n = 0.0698 \times 430 \simeq 30$, which is in excellent agreement with the experimental observation. If the number of vortices is to remain constant then β should vary as $1/R$. Our calculations do not show this behavior. Instead, β remains almost constant so that n varies with R.

The continuous variation of n can not be justified physically. However, it is possible that the number of vortices does vary but not in a continuous fashion. There is some experimental evidence of bifurcation in which n undergoes discrete jumps. Fedorov et al [13] observed

30 vortices at R = 387. However at lower Reynolds numbers (R = 180 - 245), they observe 14-16 vortices. Linear theory is unable to predict such bifurcation phenomena so nonlinear theory may be needed.

Parallel or Type II Instability

Lilly [15] presented numerical solutions of the Ekman layer problem and included the effect of Coriolis forces in his analysis. He found that at very low Reynolds numbers an instability mechanism exists whose disturbances are different from the stationary disturbances described previously. Lilly called this "parallel instability" and suggested that it is of viscous type since it vanishes at high Reynolds numbers. He found that the critical Reynolds number for these fast moving disturbances is 55 and the resulting modes are oriented at small negative angles. The orientation angle at the critical point is -23° which decreases in magnitude as the Reynolds number increases. A similar instability mechanism was detected in the experiments of Faller and Kaylor [16] (who called it a type II instability) and Tatro and Mollo-Christensen [17].

In our calculations, we also find travelling disturbances (f ~ 100 Hz relative to the disk) at low Reynolds numbers. The critical Reynolds number for these disturbances is calculated to be 49. The critical parameters are

$$\alpha = 0.27 \qquad \beta = -0.137 \qquad \omega_r = 0.146 \tag{6.4}$$

This corresponds to a wave oriented at an angle of-26.9°. These disturbances have much lower growth rates than the stationary ones.

CONCLUSIONS

The growth of instabilities in the three dimensional flow due to a rotating disk is studied both theoretically and experimentally. The experiments show clearly a region of linear growth that is in good agreement with linear stability theory that includes the effects of Coriolis forces and streamline curvature. Therefore, the e^N method gives good results for transition prediction in these three dimensional boundary layers with N of the order 11.

REFERENCES

1. Srokowski, A. J. and Orszag, S. A., "Mass Flow Requirements for LFC Wing Design", AIAA paper 77-1222.
2. Nayfeh, A. H., "Stability of Three-Dimensional Boundary Layers", AIAA J., Vol. 18, 1980, pp. 406-416.
3. Cebeci, T. and Stewartson, K., "On Stability and Transition in Three-Dimensional Flows", AIAA J., Vol. 18, 1980, pp. 398-405.
4. Smith, A. M. O. and Gamberoni, N., "Transition, Pressure Gradient, and Stability Theory", Report No. ES 26388, Douglas Aircraft Company, August 1956.
5. Hefner, J. N. and Bushnell, D. M., "Application of Stability Theory to Laminar Flow Control", AIAA Paper No. 79-1493.
6. Malik, M. R. and Orszag, S. A., "Comparison of Methods for Transition Prediction Using Three Dimensional Stability Theory," AIAA Paper 80-1375.
7. Poll, D.I.A., "Some aspects of the Flow Near a Swept Attachment Line with Particular Reference to Boundary Layer Transition", C of A Report 7805. Cranfield Institute of Technology, Cranfield, August 1978.
8. von Kármán, T., "Über laminare und turbulente Reibung", Zeitschrift für angewandte Mathematik and Mechanik, Vol. 20, pp. 241-253, 1940.
9. Smith, N. H., "Exploratory Investigation of Laminar Boundary Layer Oscillations on a Rotating Disk", N.A.C.A. Tech. Note No. 1227 (1947).

10. Gregory, N., Stuart, J. T. and Walker, W. S., "On the Stability of Three-Dimensional Boundary Layers with Application to the Flow Due to a Rotating Disk", Philosophical Transactions of the Royal Society, London, Series A, 248, 1955, pp. 155-199.

11. Clarkson, M. H., Chin, S. C. and Shacter, P., "Flow Visualization of Inflexional Instabilities on a Rotating Disk", Paper No. 80-0279.

12. Kobayashi, R., Kohama, Y. and Takamadate, Ch., "Spiral Vortices in Boundary Layer Transition Regime on a Rotating Disk", Acta Mechanica, Vol, 35, 1980, pp. 71-82.

13. Fedorov, B. I., Plavnik, G. Z., Prokhorov, I. V. and Zhukhovitskii, L. G., "Transitional Flow Conditions on a Rotating Disk", J. Engineering Physics, Vol. 31, 1976, pp. 1448-1453.

14. Brown, W. B., "Numerical Calculation of the Stability of Cross Flow Profiles in Laminar Boundary Layers on a Rotating Disk and on a Swept-Back Wing and an Exact Calculation of the Stability of the Blasius Velocity Profile", Northrop Aircraft Report NAI-59-5, Jan. 1959.

15. Lilly, D. K., "On the Instability of Ekman Boundary Flow", J. Atmospheric Sciences, Vol. 23, 1966, pp. 481-494.

16. Faller, A. J. and Kaylor, R. E., "Investigations of Stability and Transition in Rotating Boundary Layers", Ed. S. I. Pai, Dynamics of Fluids and Plasmas, Academic Press, N. Y., 1966, pp. 309-329.

17. Tatro, P. R. and Mollo-Christensen, E. L., "Experiments on Ekman Layer Instability", J. Fluid Mech., Vol. 28, 1967, pp. 531-543.

18. Orszag, S. A., "Accurate Solution of the Orr-Sommerfeld Stability Equation", J. Fluid Mech., Vol. 50, 1971, pp. 689-703.

19. Gottlieb, D. and Orszag, S. A., "Numerical Analysis of Spectral Methods", NSF-CBMS Monograph No. 26, Soc. Ind. and Appl. Math. (1977).

20. Wilkinson, J. H., "The Algebraic Eigenvalue Problem", Oxford (1965).

21. Gregory, N. and Walker, W. S., "Experiments on the Effect of Suction on the Flow Due to a Rotating Disk", J. Fluid Mech., Vol. 9, 1960, pp. 225-234.

22. Chin, D. and Litt, M., "An Electrochemical Study of Flow Instability on a Rotating Disk", J. Fluid Mech., Vol. 54, 1972, pp. 613-625.

23. Cobb, E. C. and Saunders, O. A., "Heat Transfer from a Rotating Disk", Proc. Roy. Soc., Series A 236, 1956, pp. 343-351.

Table 1. Critical and Transition Reynolds Numbers for Rotating Disk Flow

Investigators	Reynolds Number			Method of Investigation
	Critical	Transition	Onset of Transition (estimated)	
Smith [9] (1947)	460	557	-	hot-wire probe
Gregory et al [10] (1955)	430	530	-	visual (China clay technique)
Cobb & Saunders [23] (1956)	447	490	-	heat transfer from the disk
Gregory & Walker [21] (1960)	367	524	505	acoustical slitted disk
Chin & Litt [22] (1972)	412	592	510	mass transfer coefficient using electrochemical technique
Fedorov et al [13] (1976)	387	515	-	visual (Napthalene), acoustical
Clarkson et al [11] (1980)	532-621	562-680	-	visual (dye in water)
Kobayashi et al [12] (1980)	297	566	500 (non-linear oscillations)	hot wire probe
Present results	287	-	-	calculations using stability theory including Coriolis force and streamlin curvature effects

FIGURE CAPTIONS

Figure 1. Disk system lay out - top view

Figure 2. Normalized mean tangential velocity profiles for the Kármán rotating disk flow

Figure 3. Measured deviation of disk surface from a flat plane

Figure 4. Time variation of fluctuation intensity

Figure 5. Comparison of disk vibration spectrum with hot wire output. (a) Hot wire output (b) Proximeter

Figure 6. Integrated growth factor using Orr-Sommerfeld equation
(a) Present calculations
(b) Cebeci and Stewartson [3]

Figure 7. Temporal growth rates for stationary vortices
(a) Orr-Sommerfeld equation
(b) Orr-Sommerfeld equation with Coriolis force effects included
(c) Orr-Sommerfeld equation with Coriolis force and streamline curvature effects included

Figure 8. Spatial growth rates for stationary vortices
(a) Orr-Sommerfeld euqation
(b) Present theory
(+) Experimental data

Figure 9. Integrated growth factor for stationary vortices
(a) Orr-Sommerfeld equation
(b) Present theory
(+) Experimental data

Figure 10. RMS intensity of velocity fluctuations as a function of Reynolds number

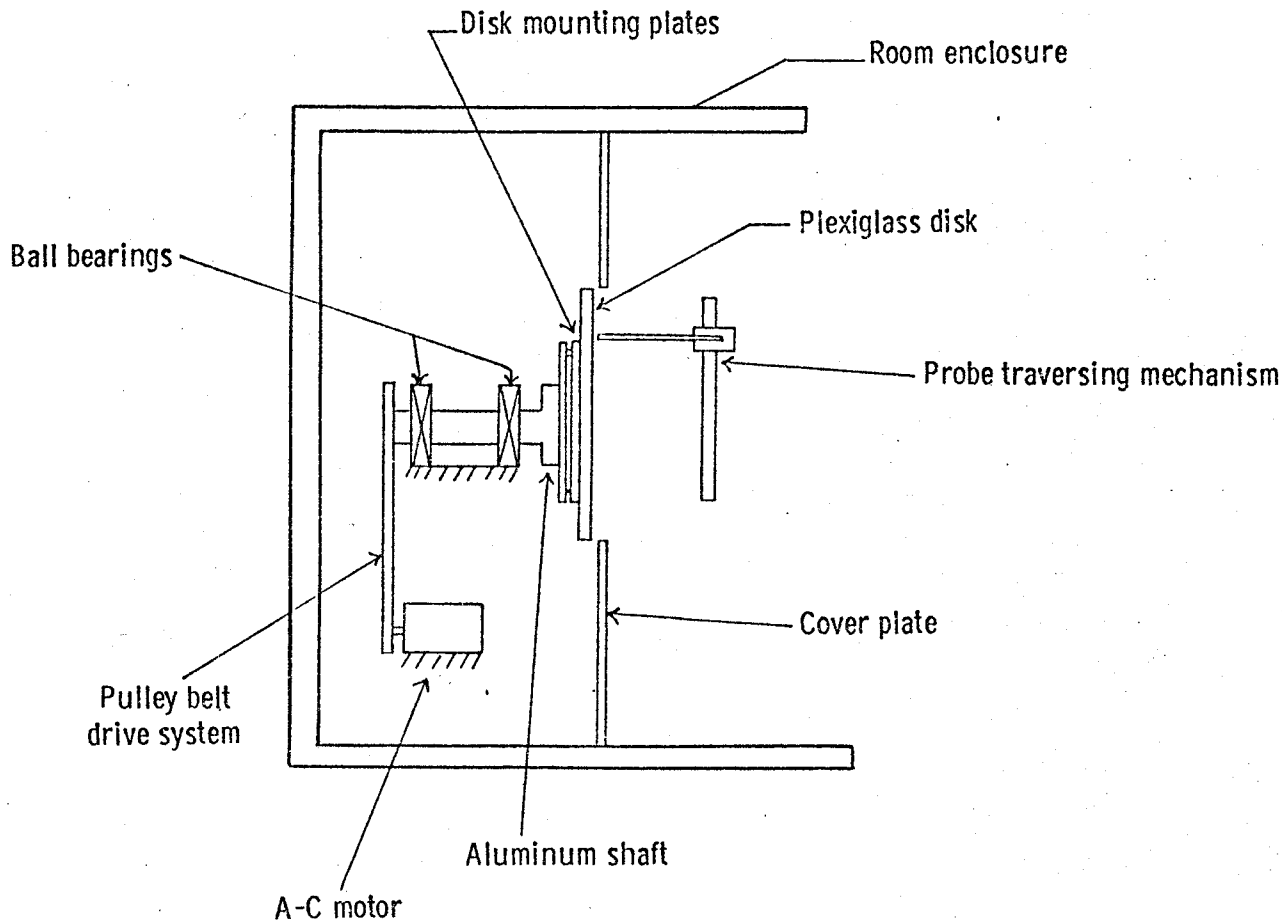

Figure 1. Disk system lay out - top view

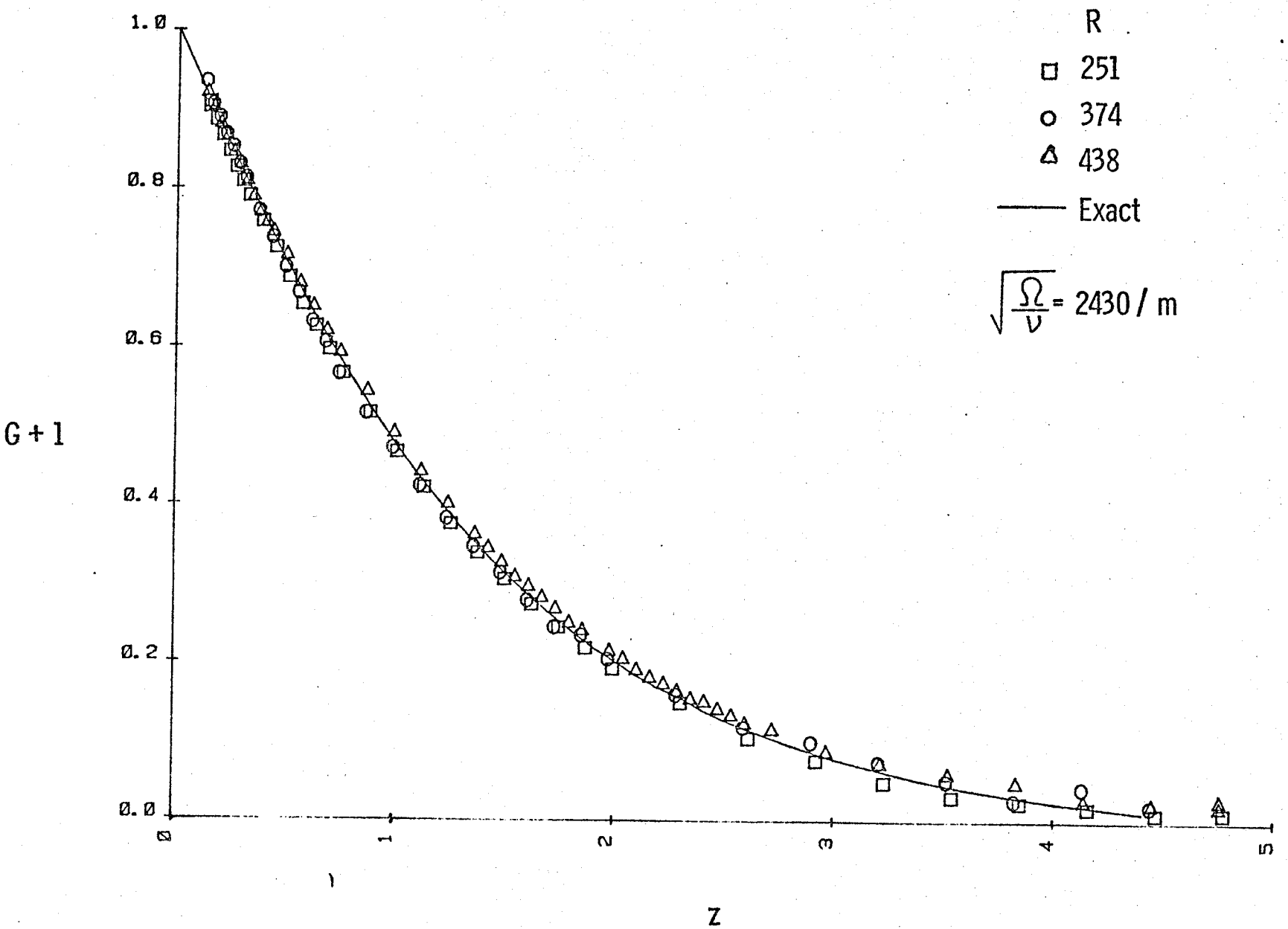

Figure 2. Normalized mean tangential velocity profiles for the Kármán rotating disk flow

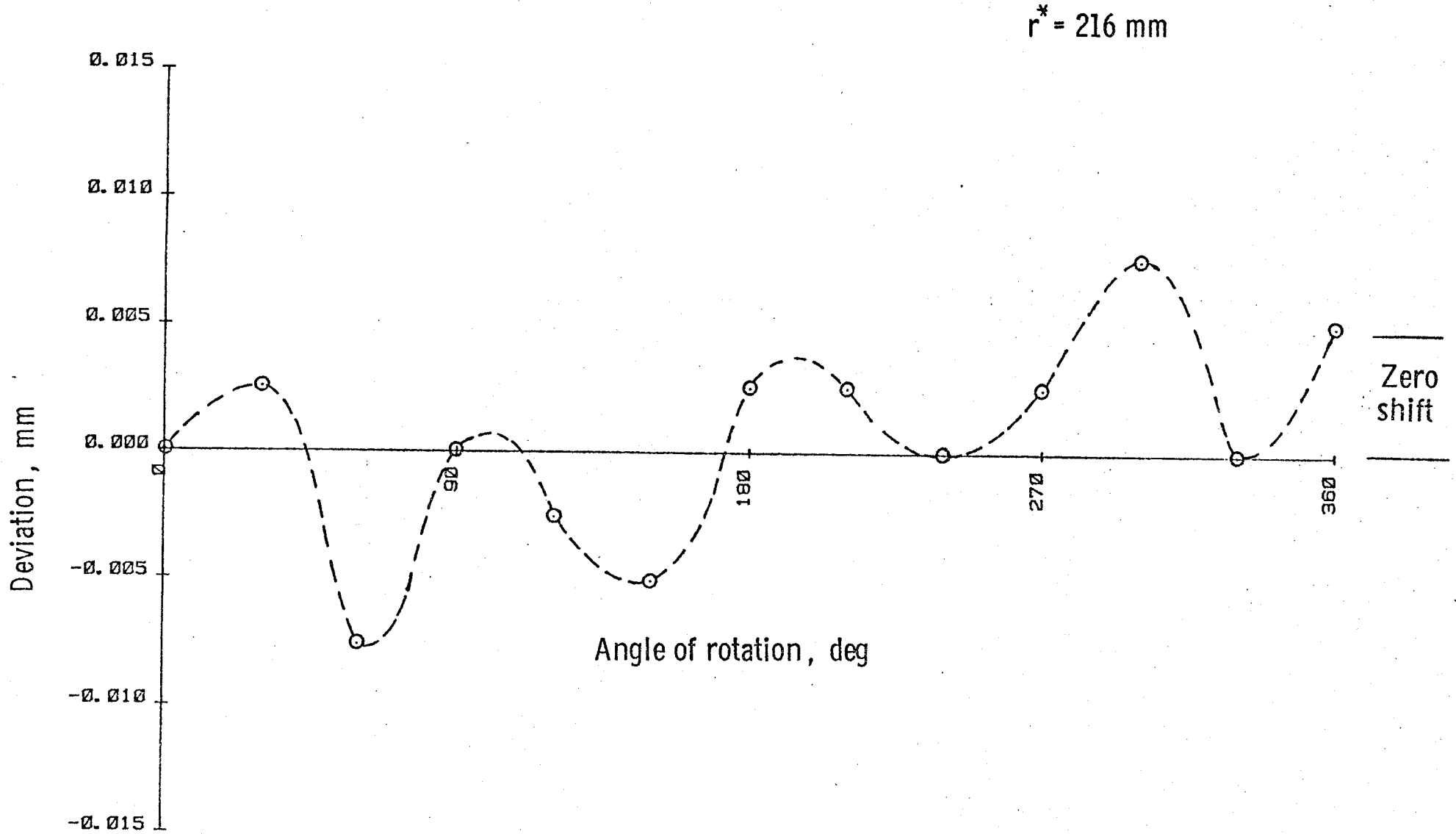

Figure 3. Measured deviation of disk surface from a flat plane

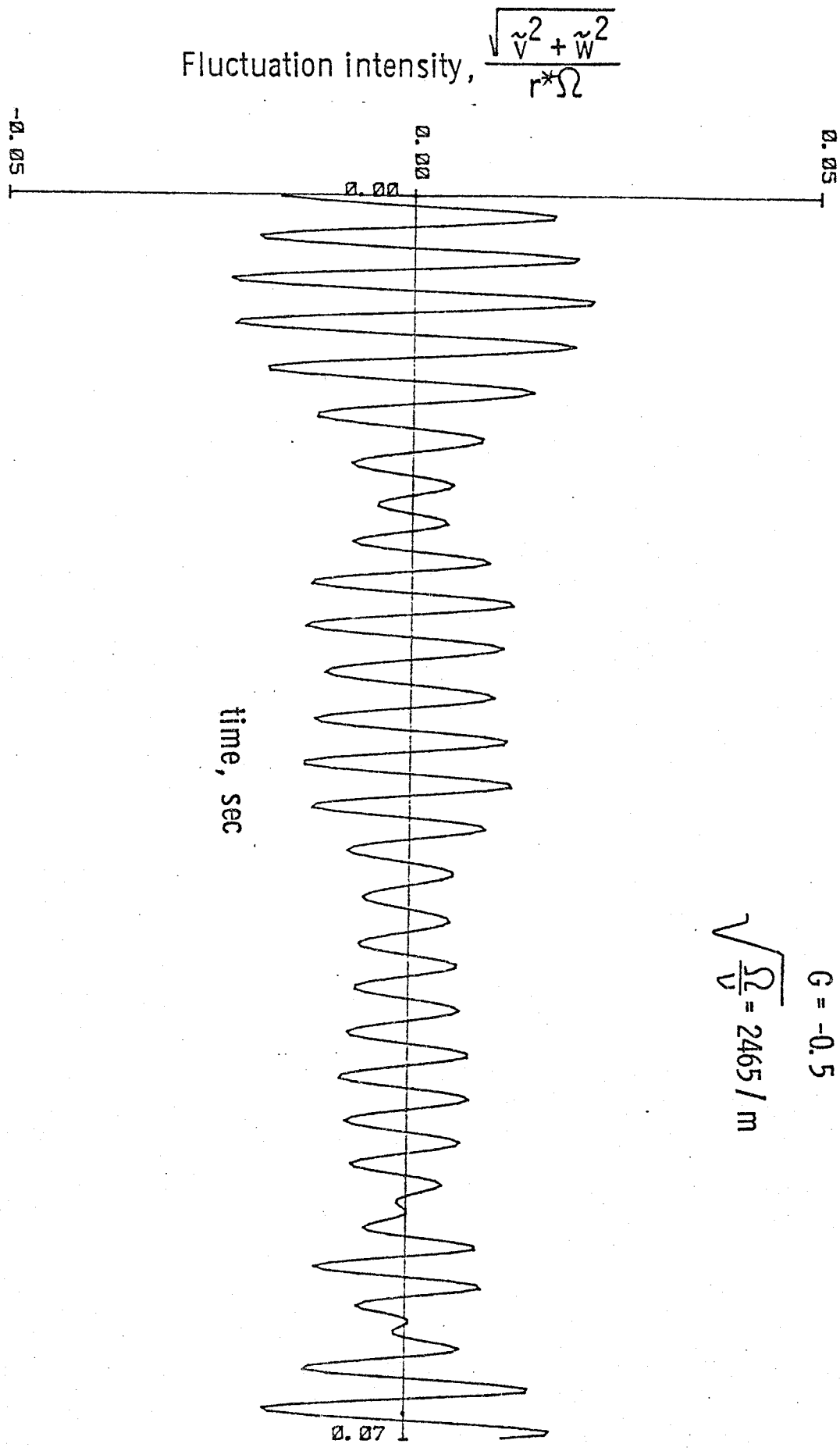

Figure 4. Time variation of fluctuation intensity

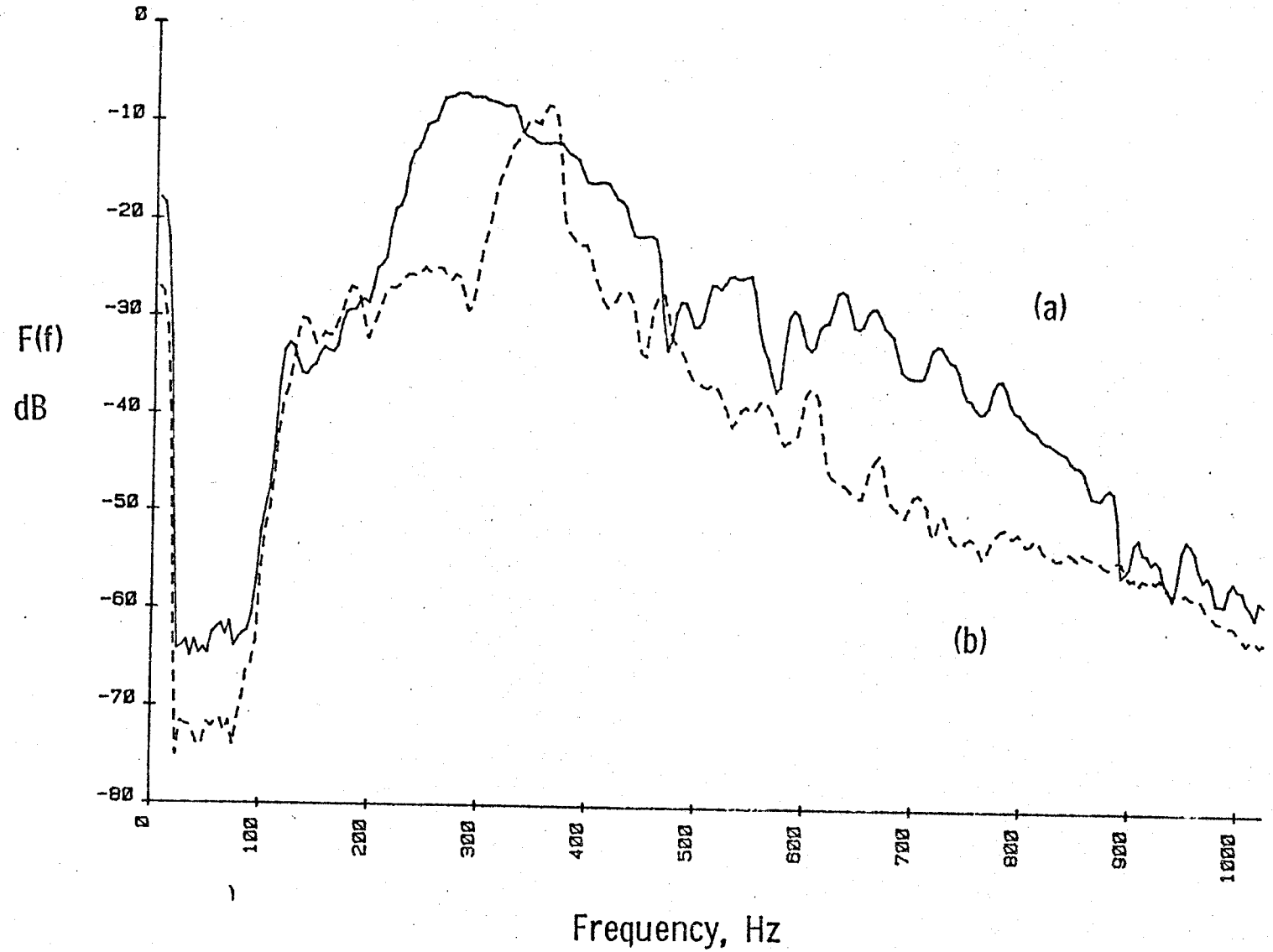

Figure 5. Comparison of disk vibration spectrum with hot wire output. (a) Hot wire output (b) Proximeter

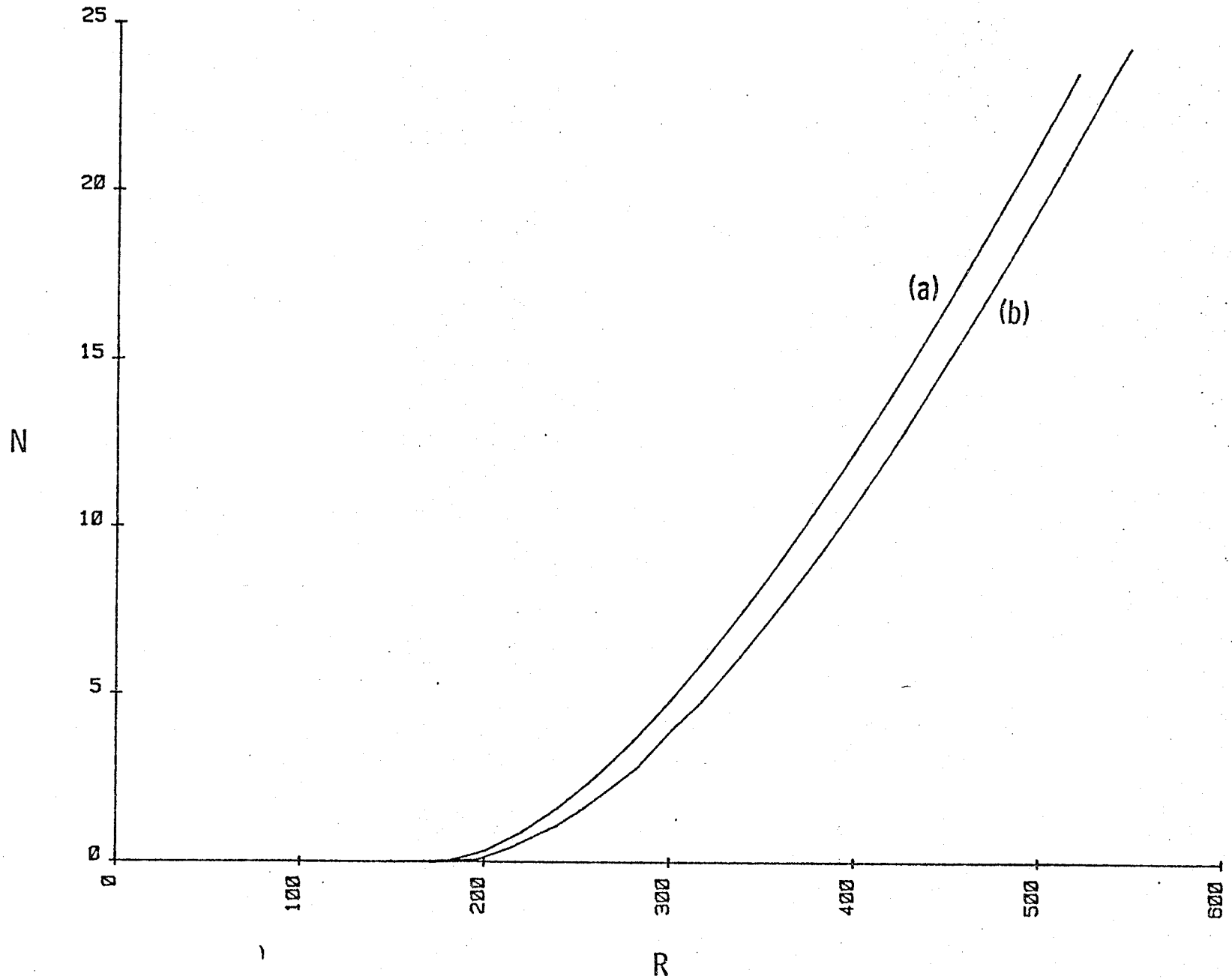

Figure 6. Integrated growth factor using Orr-Sommerfeld equation
(a) Present calculations
(b) Cebeci and Stewartson [3]

Figure 7. Temporal growth rates for stationary vortices
(a) Orr-Sommerfeld equation
(b) Orr-Sommerfeld equation with Coriolis force effects included
(c) Orr-Sommerfeld equation with Coriolis force and streamline curvature effects included

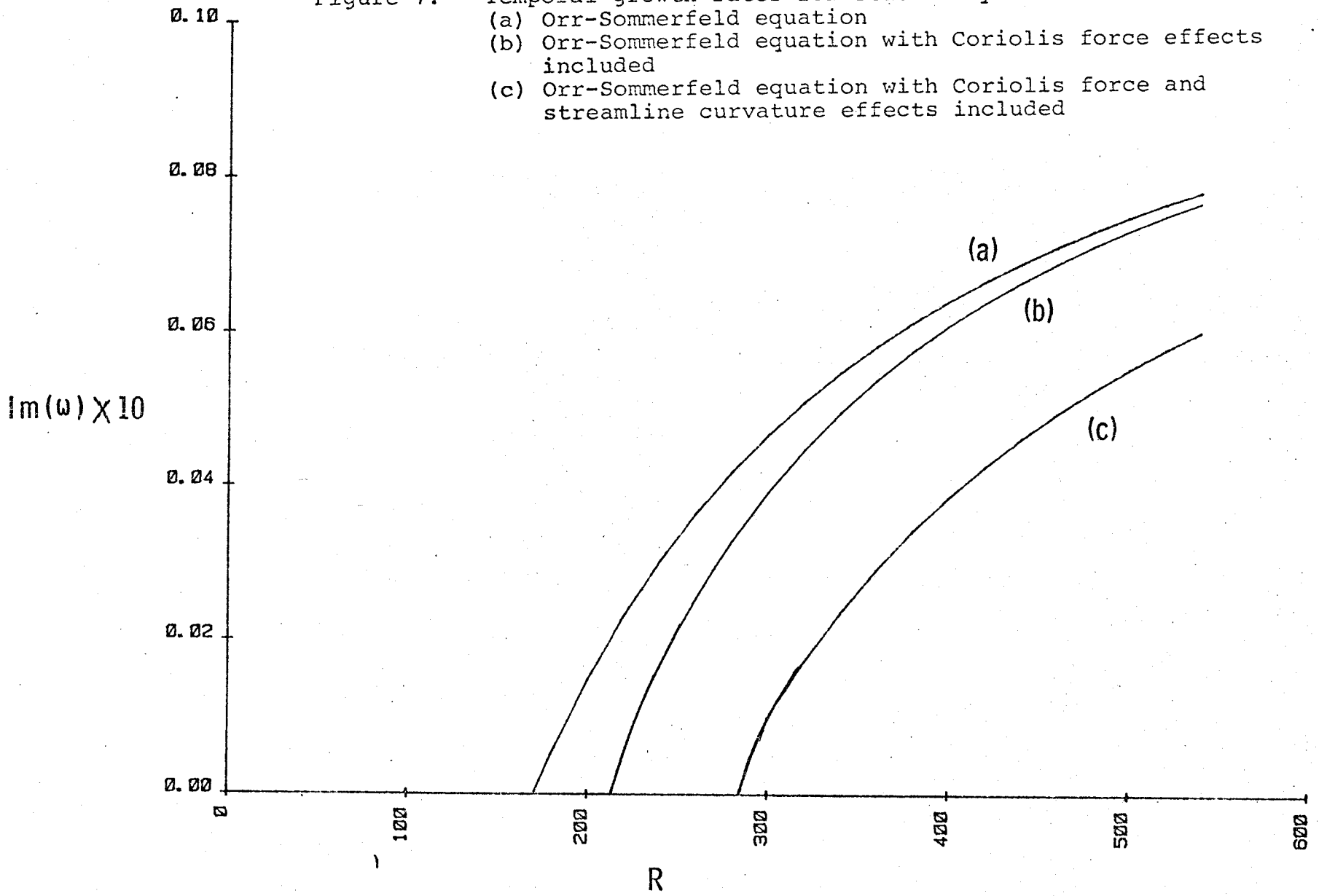

Figure 8. Spatial growth rates for stationary vortices
(a) Orr-Sommerfeld euqation
(b) Present theory
(+) Experimental data

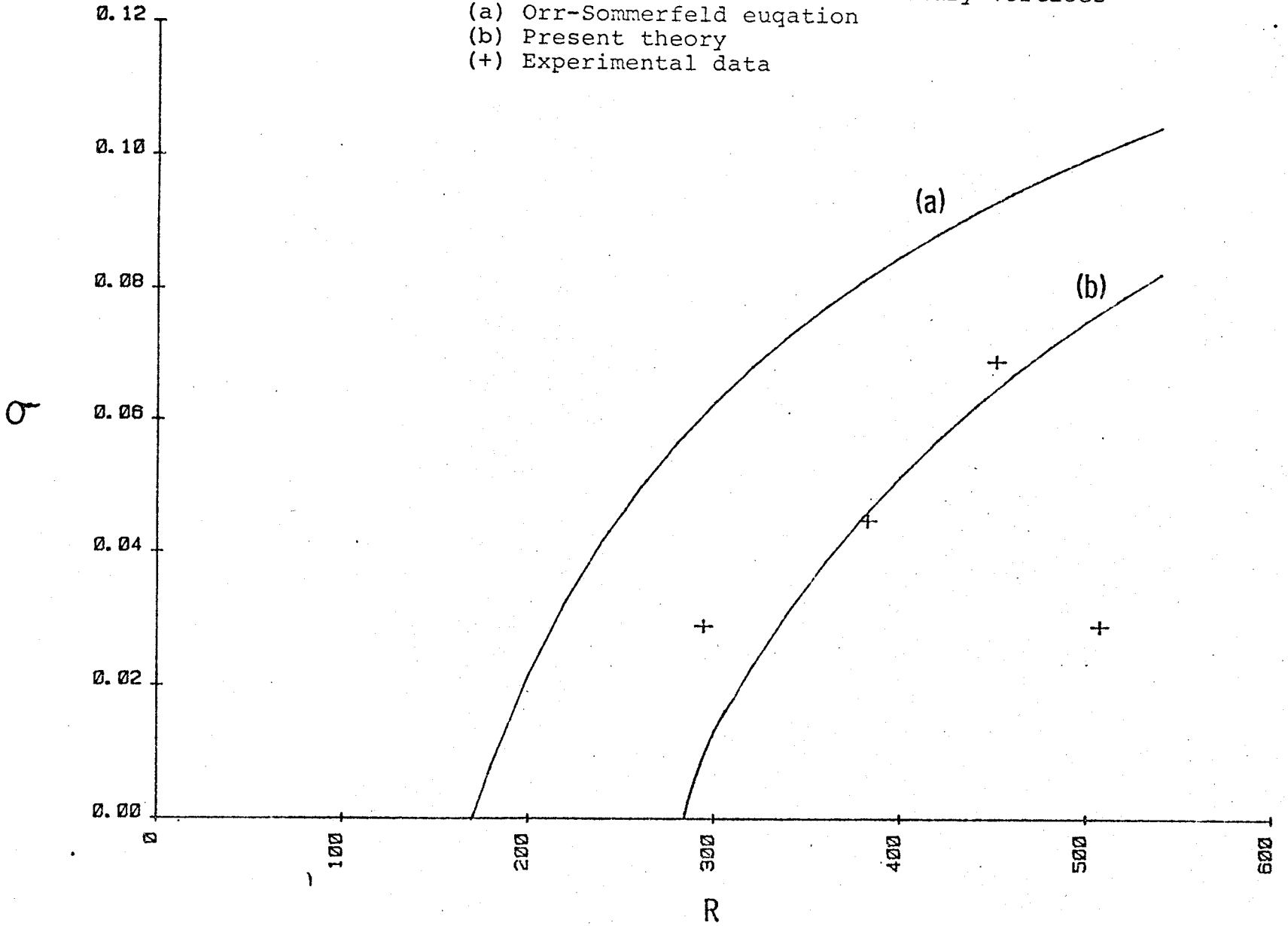

Figure 9. Integrated growth factor for stationary vortices
(a) Orr-Sommerfeld equation
(b) Present theory
(+) Experimental data

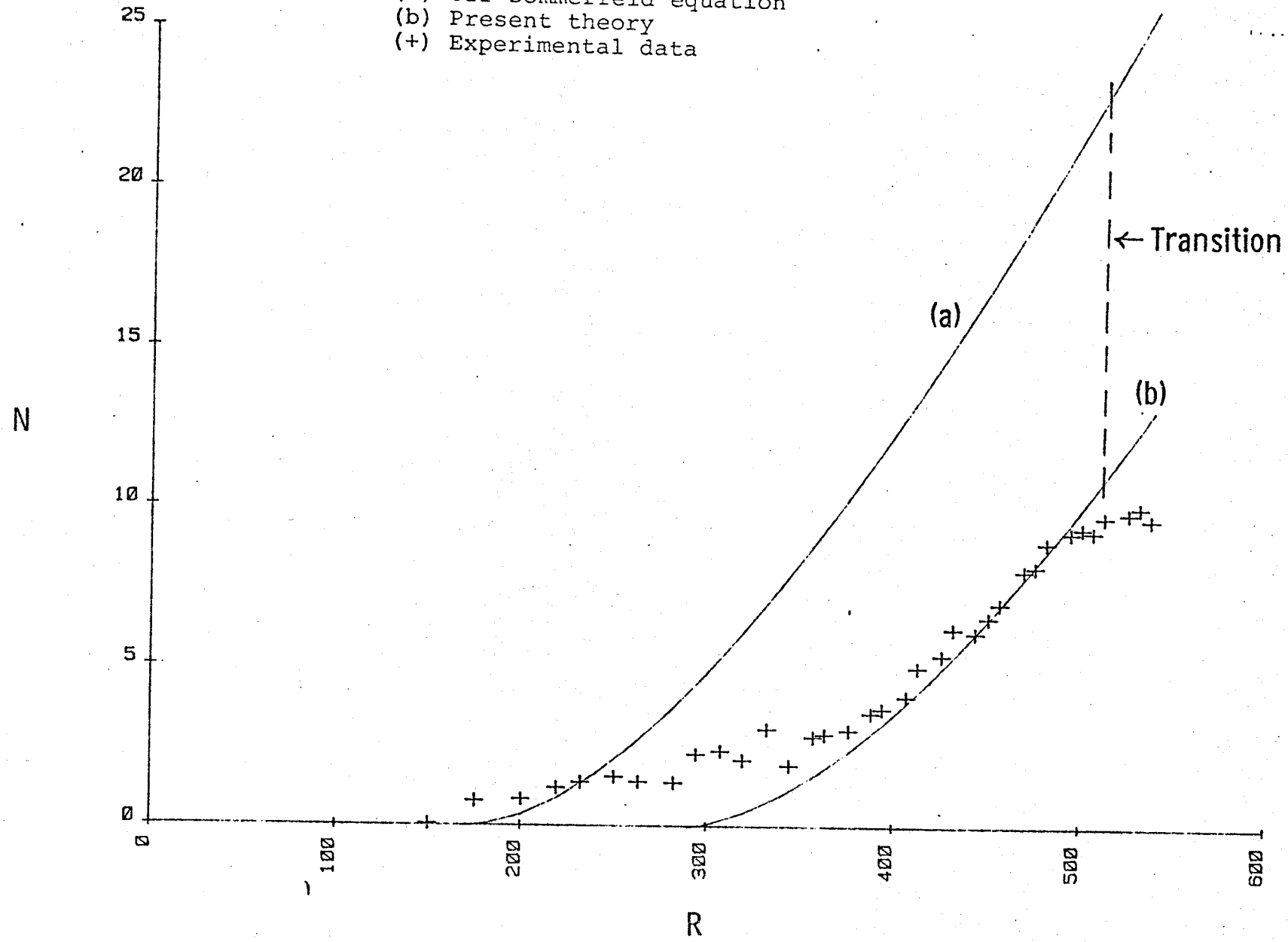

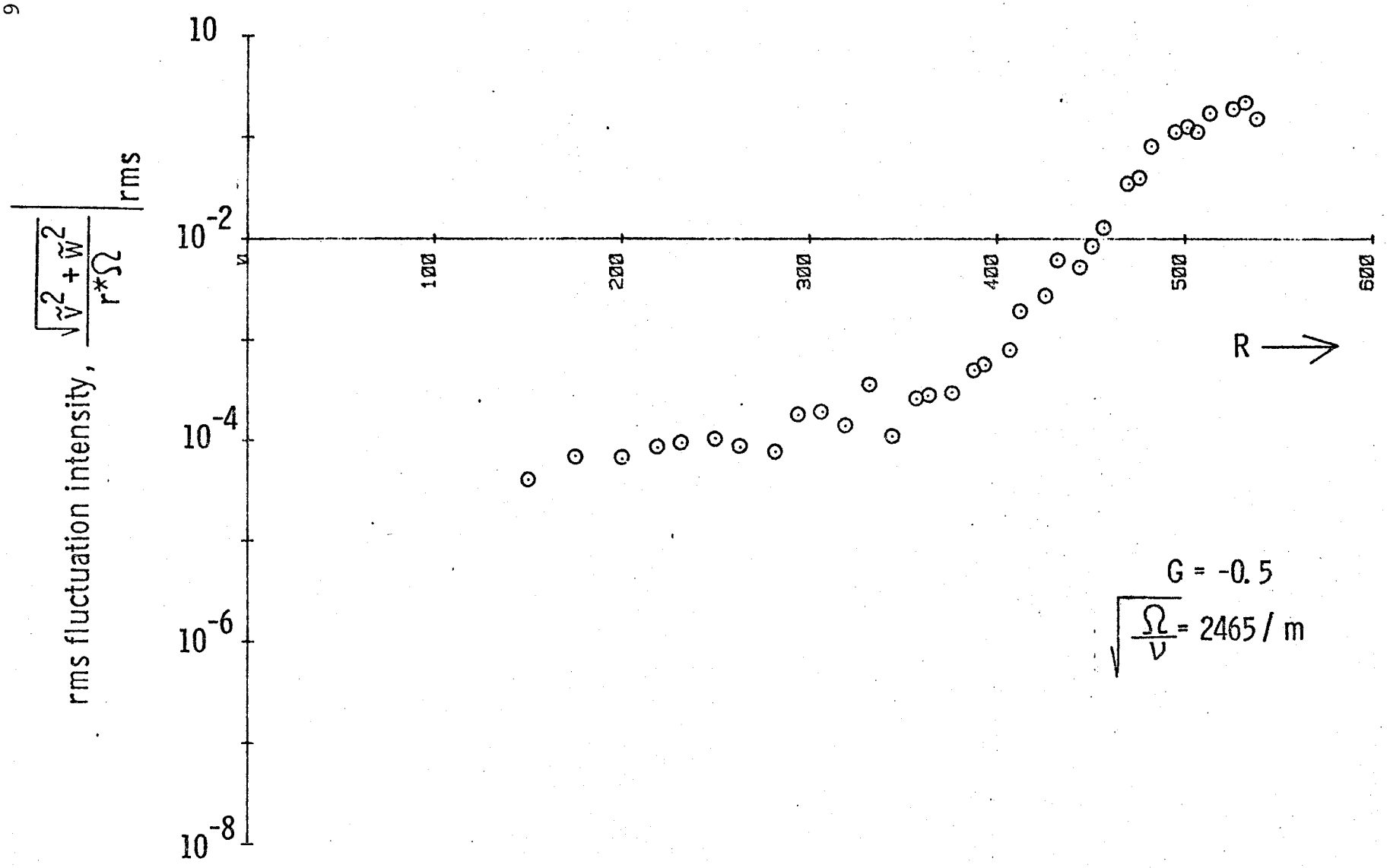

Figure 10. RMS intensity of velocity fluctuations as a function of Reynolds number

V. Subcritical Transition to Turbulence in Plane Channel Flows

While experiments[1] show that incompressible plane Poiseuille and plane Couette flow may undergo transition to turbulence at Reynolds numbers R of order 1000, linear stability analysis of these plane parallel flows gives critical Reynolds numbers of 5772 for plane Poiseuille flow[2] and ∞ for plane Couette flow[3]. This discrepancy between theory and experiment suggests that the mechanism of transition is not properly represented by parallel-flow linear stability analysis. In this Letter, we present a new linear three-dimensional mechanism that predicts transition at Reynolds numbers in good agreement with experiment for both plane Poiseuille and plane Couette flows. Here we present the theory applied to plane Poiseuille flow, defined as flow between fixed parallel plates that is driven by a pressure gradient.

We begin by studying two-dimensional travelling-wave solutions to the Navier-Stokes equations:

$$\vec{v}(x,z,t) = \vec{F}(x-ct,z) \qquad (1)$$

where c is a real wave speed, x is the downstream coordinate and z is the coordinate perpendicular to the channel walls at $z = \pm 1$. No-slip boundary conditions are applied at the walls and $2\pi/\alpha$ periodicity in x is assumed. For all R, one solution is the laminar flow $(1-z^2)$, where

$R = 1/\nu$ and ν is the kinematic viscosity. For $R \gtrsim 2900$, up to 2 other solutions (neglecting an arbitrary phase) may exist for any given α .[4] The locus of points in (E,R,α) space for which these solutions exist is called the neutral surface. Here E is the energy of the flow relative to that of the laminar flow. A slice of the neutral surface for given subcritical Reynolds number ($2900 \lesssim R < 5772$) is shown in Fig. 1.

If a one-dimensional phase space representation were appropriate to describe the behavior of flows off the neutral surface, E would evolve according to

$$\frac{dE}{dt} = f(E) \qquad (2)$$

Typically the critical points of (2) are alternately stable and unstable, so the lower branch (LB) solutions on the subcritical neutral surface plotted in Fig. 1 are unstable while the upper branch (UB) solutions are stable.

While these stability predictions are correct, the evolution of two-dimensional flows is not restricted to a one-dimensional phase space. Projections of numerical solutions[5] of the two-dimensional Navier-Stokes equations on the two-dimensional phase space $(\sqrt{E_1}, \sqrt{E_2})$ are plotted in Fig. 2. Here E_k is the kinetic energy in that part of the flow that depends on x like $e^{ik\alpha x}$. Orbits of solutions with initially large energies do not follow simple

curves. The time-dependent evolution of two-dimensional flows evidently requires a multi- (likely infinite) dimensional phase space. Thus, Landau-Stuart-Watson[6] nonlinear stability theory, which gives evolution equations of the form (2) can not be valid away from the neutral surface.[7]

Several other features of Fig. 2 are noteworthy. First, the two orbits in the lower left hand corner illustrate the existence of a threshold energy (near that of the LB solution) below which disturbances decay. Second, solutions with energies less than that of the UB solution (indicated by the point marked 'steady solution' in Fig. 2) can overshoot the UB energy by factors of 4 or more. Third, and most importantly, typical solutions quickly evolve to a state within a band of quasi-equilibria and, then, only very slowly approach the steady UB solution. The time scale for initial adjustment to a quasi-equilibrium state is of order the eddy circulation time $1/\sqrt{E}$, (i.e., of order 10) while the time scale for approach to the equilibrium state is of order the diffusion time $1/\nu$ (i.e., of order 1000 - 10000). In the quasi-equilibria, the spanwise vorticity must be nearly constant on streamlines[8], so that equilibrium is achieved by diffusion of vorticity. In fact, vorticity can vary by at most $0(\nu)$ along interior streamlines of the equilibrium flows. Nearby flows must have the same property implying the existence of quasi-equilibria evolving only on a diffusive time scale.

The quasi-equilibria are the basis of our transition mechanism in plane Poiseuille flow as direct numerical solution of the Navier-Stokes equations[9] shows that they

are strongly unstable to infinitesimal three-dimensional disturbances. In Fig. 3, we plot the evolution of (initially small) three-dimensional disturbances superposed on finite-amplitude two-dimensional motions. Evidently, the three-dimensional disturbances quickly achieve a form that grows exponentially in time for $R \gtrsim 1000$. The growth rate of the three-dimensional disturbances is rapid with their amplitude increasing by a factor of about 10 in a time of 10. This short time scale for subcritical three-dimensional growth should be contrasted with the long time scale of order 1000 for evolution of supercritical Orr-Sommerfeld modes.[2]

There is strong evidence that this instability is a physically relevant one in that it is fairly insensitive to initial conditions and has small threshold energies. It is necessary to distinguish here between this instability and the ensuing transition to turbulence. If the two-dimensional flow persists sufficiently long for the three-dimensional perturbations to attain a finite amplitude, direct numerical simulation has shown[9] that the resulting three-dimensional flow quickly develops a turbulent character with strongly non-periodic behavior. Thus to 'predict' transition one must know the initial two-dimensional and three-dimensional energies as well as their respective time scales. For instance, the most dangerous three dimensional instability for given two-dimensional energy is not necessarily the most likely to force transition if the two-dimensional state is outside the

band (in wavenumber) of quasi-equilibria. It is possible to use our methods to construct a neutral surface for transition in any given (presumably large) parameter space. However, we confine attention here to demonstrating that our mechanism predicts transitional Reynolds numbers in accordance with experiment.

The exponential growth illustrated in Fig. 3 suggests that a linear instability mechanism is involved.[10] Assuming a flow of the form

$$\vec{v}(\vec{x},t) = \vec{F}(x-ct,z) + \varepsilon\, \mathrm{Re}[\vec{G}(x-ct,z)e^{\sigma t+i\beta y}] , \qquad (3)$$

substituting into the Navier-Stokes equations, and linearizing with respect to ε, a linear eigenvalue problem for σ results. The Galilean transformation to a reference frame moving with the phase speed c eliminates time-dependent coefficients, so the problem is separable in t. The resulting eigenvalue problem has been solved numerically using Chebyshev polynomial expansions in z and highly truncated Fourier series expansions in x for $\vec{F}$ and $\vec{G}$. In Fig. 4, we plot the maximum growth rate[11], $\mathrm{Re}(\sigma)$, vs the spanwise wavenumber β for $R = 4000$, $\alpha = 1.25$. The results of direct numerical simulations (cf. Fig. 3) are also plotted in Fig. 4. Evidently, the large growth rates observed in the direct numerical simulations can be explained by this linear eigenvalue problem.

Note that the linear theory presented above can be extended to Reynolds numbers below 2900 by freezing the

quasi-equilibria which evolve very slowly compared to the rapid exponential growth of the three-dimensional perturbations. For $R \gtrsim 1000$, the quasi-equilibria decay sufficiently slowly that three-dimensional perturbations can grow, overwhelm the two-dimensional flow, and break down to turbulence.

The rapid growth rates described above are due to the combined action of vortex stretching by the nearly inviscid two-dimensional steady motion $\vec{F}$ and tilting of the vortex lines of $\vec{F}$ by the perturbation $\vec{G}$. By itself, vortex stretching by $\vec{F}$ can not give exponential growth rates because of the two-dimensional anti-dynamo theorem.[12] Detailed flow visualizations of the instabilities described here will be given elsewhere. It will be shown that three-dimensional perturbations grow on a time scale of order $1/\sqrt{E}_{2-D}$, which must be shorter than the decay time of the two dimensional motion for the instability to be effective. The sharp cutoff in growth rate $Re(\sigma)$ for small β observed in Fig. 4 reflects a threshold of streamwise vorticity for stretching to persist.

Direct numerical simulations[9] of transition in plane Couette flow show that while there is no evidence that equilibria of the form (1) exist, the three-dimensional instability process outlined above is still effective down to Reynolds numbers of order 1000. While there are no quasi-equilibria in plane Couette flow that evolve on purely diffusive time scales, the decay rates of finite-amplitude two-dimensional disturbances are still several eddy circulation times.

This implies that the threshold three-dimensional energies in plane Couette flow are somewhat larger than in plane Poiseuille flow. However, the resulting instability is at least as strong and turbulence quickly ensues.

References

1. For transition experiments in plane Poiseuille flow see Davies, S. J. and C. M. White, Proc. Roy. Soc., A119, 92 (1928). For plane Couette flow, see Reichardt, H., Max-Planck-Inst. StrömForsch., 22 (1959). Further references are given by Orszag, S. A. and L. C. Kells, J. Fluid Mech., 96, 159 (1980).
2. Orszag, S. A., J. Fluid Mech., 50, 689 (1971).
3. Davey, A., J. Fluid Mech., 57, 369 (1973).
4. Zahn, J.-P., J. Toomre, E. A. Spiegel, and D. O. Gough, J. Fluid Mech., 64, 319 (1974). See also Herbert, T., in Proc. 5th Int. Conf. on Numerical Methods in Fluid Dynamics, edited by A. I. van de Vooren and P. J. Zandbergen, (Springer, Berlin, 1976), p. 235.
5. Patera, A. T. and S. A. Orszag,in Proc. 7th Int. Conf. on Numerical Methods in Fluid Dynamics, (Springer, Berlin, in press). For further details on the numerical methods, see Orszag and Kells (Ref. 1).
6. Stuart, J. T., Ann. Rev. Fluid Mech., 3, 347 (1971).
7. Herbert, T., AIAA J., 18, 243 (1980). Behavior similar to that plotted in Fig. 2 is observed in other low-dimensional phase spaces, such as $(\sqrt{E_3}, \sqrt{E_4})$.
8. Batchelor, G. K., J. Fluid Mech., 1, 177 (1956).
9. See Orszag and Kells (Ref. 1) and Patera and Orszag (Ref. 5). We have used several different spectral codes at various space-time resolutions to solve the three-dimensional incompressible Navier-Stokes equations.

All the codes employ Fourier series in the (assumed) periodic directions (spanwise and streamwise) and Chebyshev polynomials in the cross-stream direction. The codes differ in their treatment of the incompressibility constraint and viscous effects. The accuracy of our results has been carefully checked by comparison runs.

10. A related linear stability calculation to explain the wavy instability of Bénard convection rolls has been given by Clever, R. M. and F. H. Busse, J. Fluid Mech. 65, 625 (1974).

11. The stability calculations exploit symmetries in y and z consistent with the Navier-Stokes equations. The fastest growing mode for the particular set of symmetries assumed here has $\mathrm{Im}(\sigma) = 0$, and as a result G_x, G_z can be taken real and G_y pure imaginary. This reduces the computational work considerably. We use 33 Chebyshev polynomials in z for each of the 2 Fourier modes in x, resulting in a 106×106 (real) matrix eigenvalue problem. Further details will be published elsewhere.

12. Bullard, E. C. and H. Gellman, Phil. Trans. Roy. Soc. (London) A247, 213 (1954).

Figure Captions

Fig. 1.

A subcritical (E,α) slice of the neutral surface for plane Poiseuille flow at $R = 4000$. The stability of solutions is indicated by the arrows. The behavior shown in this plot is typical for $2900 \lesssim R < 5772$.

Fig. 2.

A phase portrait of disturbances to laminar plane Poiseuille flow in $(\sqrt{E_1},\sqrt{E_2})$ space at $R = 4000, \alpha = 1.25$. The dots, equally spaced by 1.25 in time, indicate the evolution of perturbations from initial conditions proportional to the least stable Orr-Sommerfeld eigenfunction at this (α,R). Note the existence of a band of quasi-equilibria.

Fig. 3.

A plot of the growth of three-dimensional perturbations on finite-amplitude two-dimensional states in plane Poiseuille flow at $(\alpha,\beta) = (1.32, 1.32)$. Here E_{2-D} is the total energy (relative to the laminar flow) in wavenumbers of the form $(n\alpha,0)$, while E_{3-D} is the total energy in wavenumbers $(n\alpha,\beta)$. For $R \gtrsim 1000$ we obtain growth and for $R = 500$ decay. The growth rate of the three-dimensional disturbance <u>amplitude</u> at $R = 4000$ is about 0.18 $(\sim\sqrt{E_{2-D}})$ and depends only weakly on R for larger R. The initial conditions are superpositions of the laminar flow, a [large $(E_{2-D}=0.04)$] two-dimensional Orr-Sommerfeld mode with wavevector $(\alpha,0)$ and a [very

small ($E_{3-D} = 10^{-16}$)] three-dimensional transverse Orr-Sommerfeld mode with wavevectors $(0,\beta)$.

Fig. 4.

A plot of the growth rate σ of three-dimensional perturbations as a function of β at $R = 4000$, $\alpha = 1.25$. Note the good agreement between the linear calculation and the 2-mode direct simulations. Increasing the number of retained modes in x increases the growth rates. However, the error in the 2-mode model is not large.

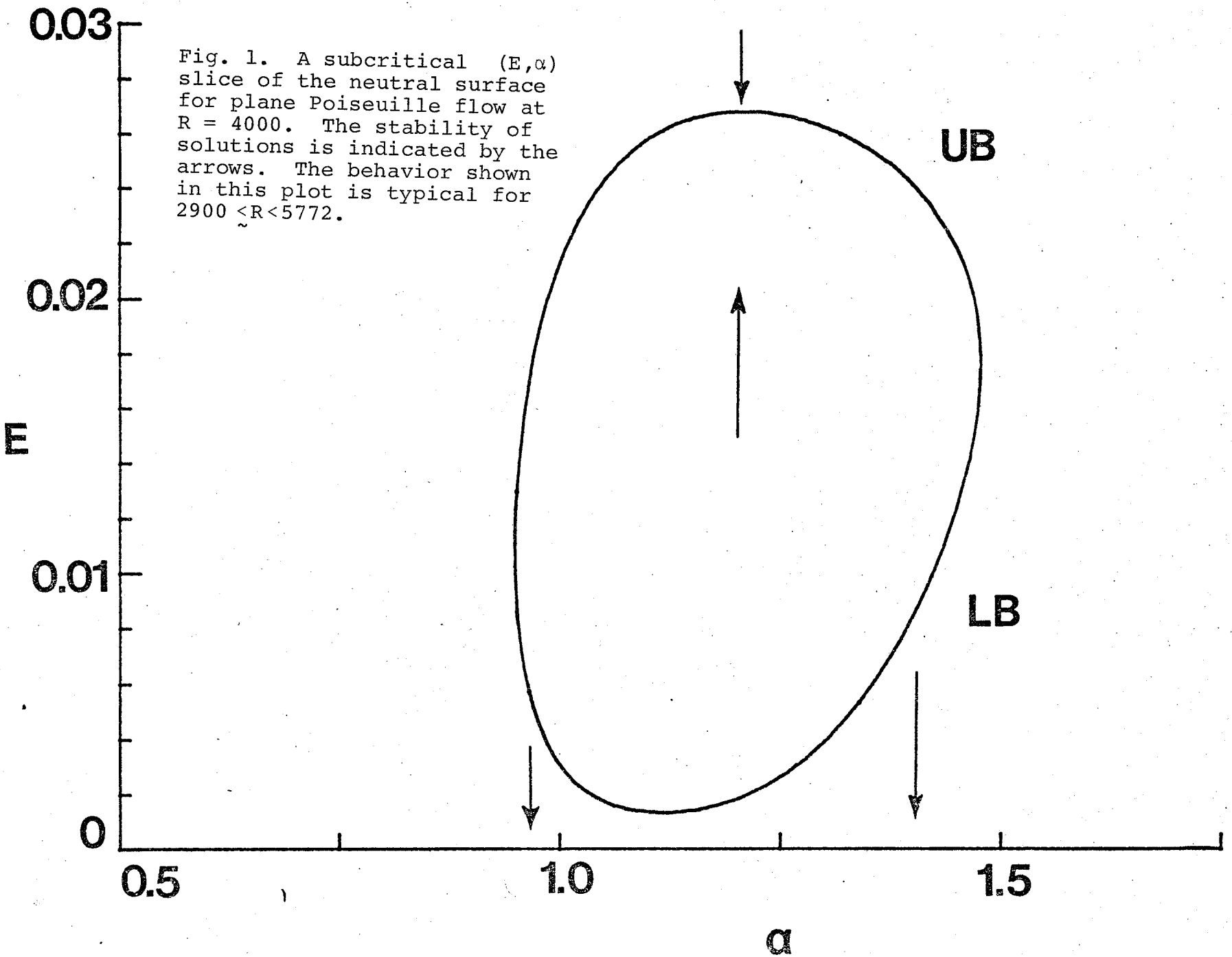

Fig. 1. A subcritical (E,α) slice of the neutral surface for plane Poiseuille flow at $R = 4000$. The stability of solutions is indicated by the arrows. The behavior shown in this plot is typical for $2900 \lesssim R < 5772$.

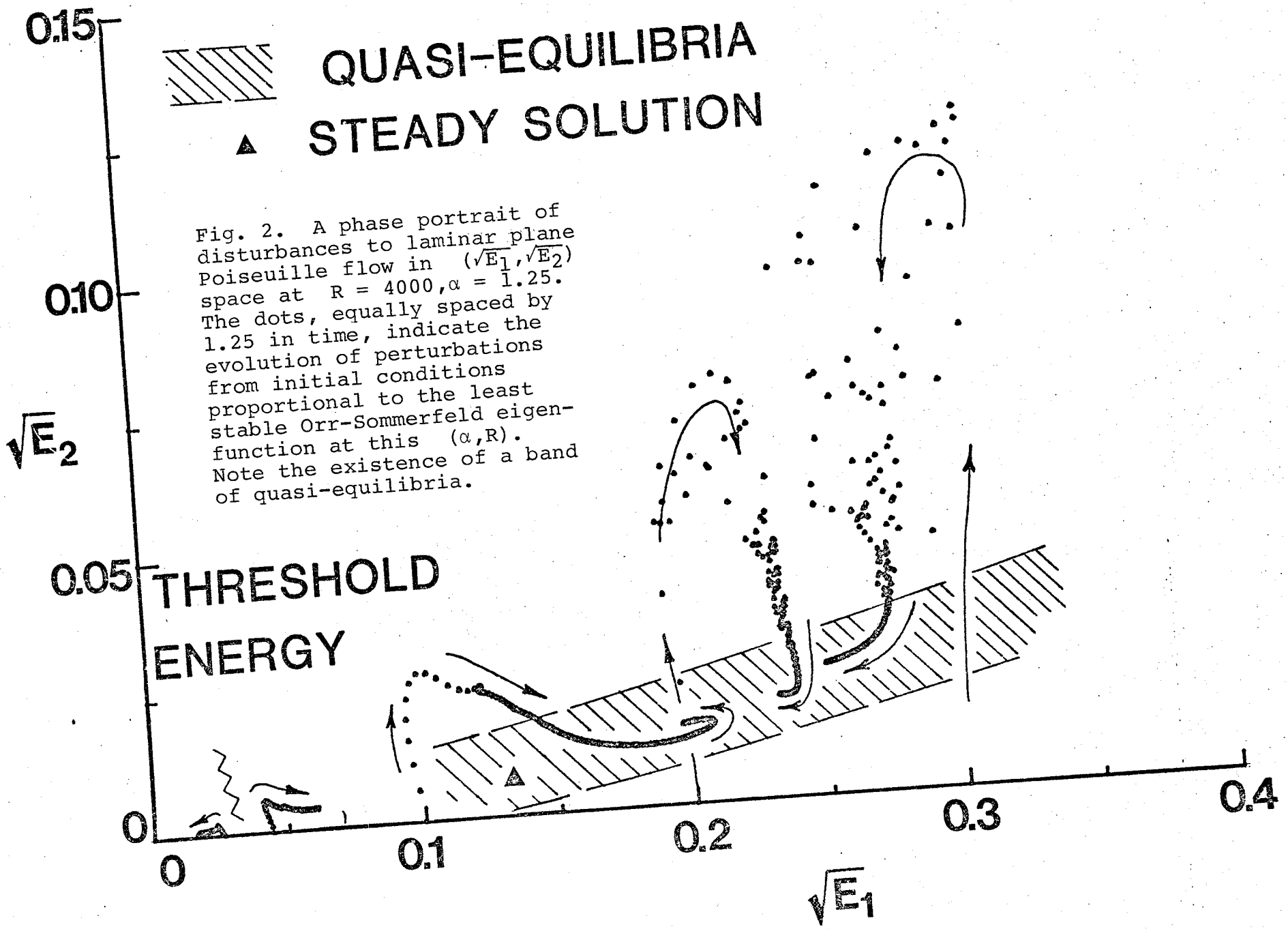

Fig. 2. A phase portrait of disturbances to laminar plane Poiseuille flow in $(\sqrt{E_1},\sqrt{E_2})$ space at $R = 4000, \alpha = 1.25$. The dots, equally spaced by 1.25 in time, indicate the evolution of perturbations from initial conditions proportional to the least stable Orr-Sommerfeld eigenfunction at this (α,R). Note the existence of a band of quasi-equilibria.

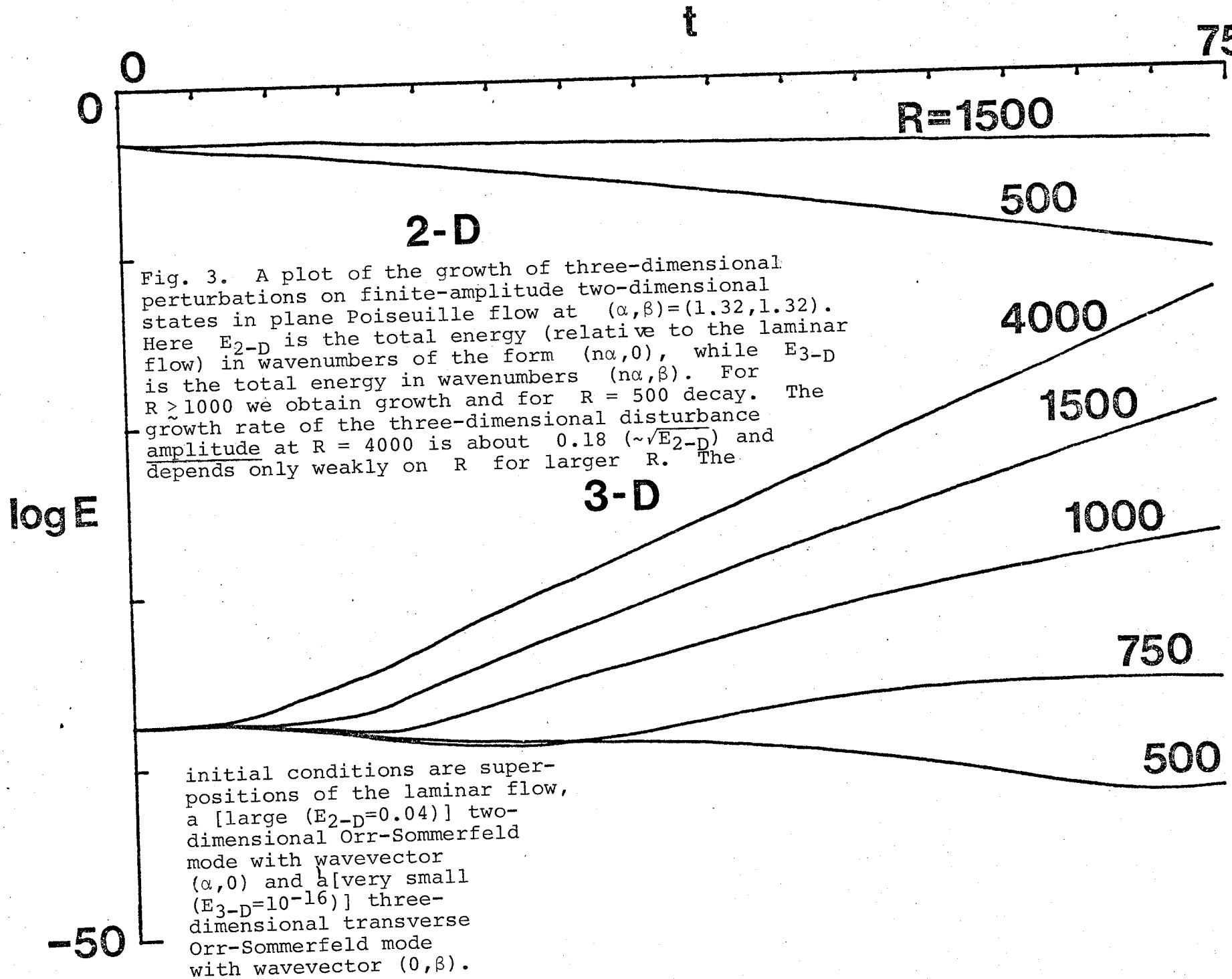

Fig. 3. A plot of the growth of three-dimensional perturbations on finite-amplitude two-dimensional states in plane Poiseuille flow at $(\alpha,\beta)=(1.32,1.32)$. Here E_{2-D} is the total energy (relative to the laminar flow) in wavenumbers of the form $(n\alpha,0)$, while E_{3-D} is the total energy in wavenumbers $(n\alpha,\beta)$. For $R \gtrsim 1000$ we obtain growth and for $R = 500$ decay. The growth rate of the three-dimensional disturbance amplitude at $R = 4000$ is about 0.18 ($\sim\sqrt{E_{2-D}}$) and depends only weakly on R for larger R. The initial conditions are superpositions of the laminar flow, a [large ($E_{2-D}=0.04$)] two-dimensional Orr-Sommerfeld mode with wavevector $(\alpha,0)$ and a [very small ($E_{3-D}=10^{-16}$)] three-dimensional transverse Orr-Sommerfeld mode with wavevector $(0,\beta)$.

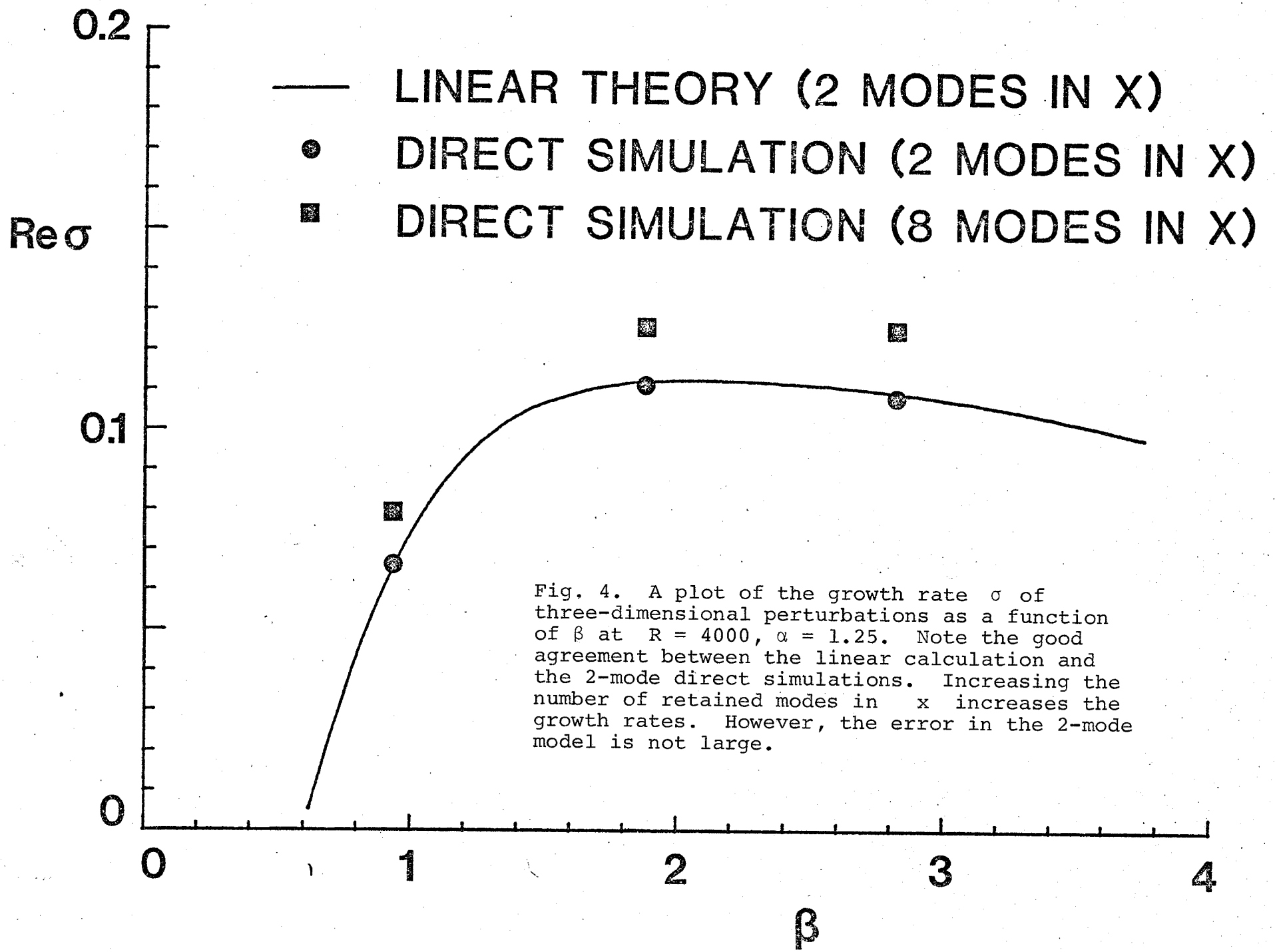

Fig. 4. A plot of the growth rate σ of three-dimensional perturbations as a function of β at $R = 4000$, $\alpha = 1.25$. Note the good agreement between the linear calculation and the 2-mode direct simulations. Increasing the number of retained modes in x increases the growth rates. However, the error in the 2-mode model is not large.

VI. Finite Amplitude Stability of Axisymmetric Pipe Flow

ABSTRACT

The stability of pipe flow to axisymmetric disturbances is studied by direct numerical simulation of the incompressible Navier-Stokes equations. There is no evidence of finite-amplitude equilibria at any of the wavenumber/Reynolds number combinations investigated, with all perturbations decaying on a time scale much shorter than the diffusive (viscous) time scale. In particular, decay is obtained where amplitude-expansion perturbation techniques predict equilibria, indicating that these methods are not valid away from the neutral curve of linear stability theory.

1. INTRODUCTION

It is generally agreed that pipe Poiseuille flow (also called Hagen-Poiseuille flow) is linearly stable to all disturbances (both axisymmetric and non-axisymmetric) at all Reynolds numbers (Sexl 1927, Lessen et al 1968, Davey & Drazin 1969, Metcalfe & Orszag 1973, Salwen et al 1980) . Therefore, the explanation of the observed transition to turbulence in this flow requires finite-amplitude instabilities.

Finite-amplitude stability analyses of pipe flow have so far been restricted to axisymmetric disturbances (Davey & Nguyen 1971) and even these results are not without controversy (Itoh 1977, Davey 1977). In this paper, we use spectral methods to investigate numerically the behavior of finite-amplitude axisymmetric disturbances in pressure-driven pipe flow. The basic question concerns the existence of finite-amplitude equilibrium states of this flow. If such states do not exist then pipe flow is stable to all axisymmetric distrubances. Available finite-amplitude analyses predict equilibria, however they are in disagreement over both results and methodology.

2. NUMERICAL METHODS

The axisymmetric incompressible Navier-Stokes equations are, in rotation form,

$$\frac{\partial u}{\partial t} = -\frac{\partial \Pi}{\partial x} + \frac{4}{R} + v\omega + \frac{1}{R}\left(D^2 + \frac{\partial^2}{\partial x^2}\right) u \qquad (1)$$

$$\frac{\partial v}{\partial t} = -\frac{\partial \Pi}{\partial r} - u\omega + \frac{1}{R}\left(D^2 - \frac{1}{r^2} + \frac{\partial^2}{\partial x^2}\right) v \qquad (2)$$

$$\frac{\partial}{\partial x}(ru) + \frac{\partial}{\partial r}(rv) = 0 \qquad (3)$$

where u and v are the velocities in the x and r directions, respectively, $D^2 = \frac{1}{r}\,\partial/\partial r(r\partial/\partial r)$, and $\omega = \partial v/\partial x - \partial u/\partial r$ is the azimuthal vorticity. The boundary conditions on the velocities are

$$u,\ v/r \text{ bounded } (r = 0),\quad u, v = 0 \quad (r = 1) \qquad (4)$$

R is the Reynolds number based on pipe radius and center-line velocity. The constant pressure gradient term is assumed to be that of the laminar flow, namely $4/R$, and Π is the disturbance pressure head.

We discuss briefly below four features of our numerical methods: spectral representation; time-stepping; operator inversion; and initial conditions. The major

difference between the present pipe flow calculations and our plane channel flow simulations (Orszag & Kells 1980; Patera & Orszag 1980) is that variable-coefficient equations must now be solved implicitly, whereas in planar geometry only constant coefficient equations require implicit solution.

The velocities are expanded as

$$u(x,r,t) = \sum_{|n|\leq N} \sum_{p=0}^{P} \tilde{u}(n,p,t) e^{i\alpha n x} T_{2p}(r) \qquad (5)$$

$$v(x,r,t) = \sum_{|n|<N} \sum_{p=0}^{P} \tilde{v}(n,p,t) e^{i\alpha n x} T_{2p+1}(r) \qquad (6)$$

where the Chebyshev polynomials $T_q(r)$ are defined by

$$T_q(\cos\theta) = \cos q\theta$$

The even (odd) nature of u (v) follows naturally from the axisymmetry of the problem. Boundedness at the origin is then automatically imposed. Periodic boundary conditions are applied in x with periodicity interval $2\pi/\alpha$.

A fractional time stepping method (Orszag & Kells 1980) is used, each full step consisting of (i) a non-linear step, (ii) a pressure step, and (iii) a viscous dissipation step. For the first fractional step a second order Adams-Bashforth method is used:

$$\hat{u}^{n+1} = u^n + \Delta t \left(\frac{3}{2} v^n \omega^n - \frac{1}{2} v^{n-1} \omega^{n-1} + 4/R\right)$$

$$\hat{v}^{n+1} = v^n + \Delta t \left(-\frac{3}{2} u^n \omega^n + \frac{1}{2} u^{n-1} \omega^{n-1}\right)$$

where the superscript refers to time step. The non-linear terms are calculated efficiently using transform methods and collocation (pseudospectral) techniques (Gottlieb & Orszag 1977). Products are evaluated in physical space while derivatives are calculated in spectral space. Transformations between the two representations are done using extensions of the fast Fourier transform algorithm. In the remainder of this Section it is assumed that the velocities are in mixed representation, Fourier in x but physical in r. The axial wavenumber of a Fourier mode will be denoted by γ.

Next, incompressibility is imposed with the pressure step

$$\hat{\hat{u}}^{n+1} = \hat{u}^{n+1} - i\gamma\Delta t\Pi^* \quad (r < 1) \tag{7}$$

$$\hat{\hat{v}}^{n+1} = \hat{v}^{n+1} - \Delta t \frac{\partial \Pi^*}{\partial r} \quad (r < 1) \tag{8}$$

$$i\gamma r\hat{\hat{u}}^{n+1} + \frac{\partial}{\partial r}(r\hat{\hat{v}}^{n+1}) = 0 \quad (r \leq 1) \tag{9}$$

$$\hat{\hat{v}}^{n+1} = 0 \quad (r = 1), \tag{10}$$

where we write Π^* rather than Π to indicate that the pressure obtained here is an intermediate result. Eqns. (7)-(10) can be combined to give a single equation for Π^*,

$$(D^2 - \gamma^2)\pi^* = i\gamma\hat{u}^{n+1} + \frac{1}{r}\frac{\partial}{\partial r}(r\hat{v}^{n+1}) \quad (r < 1) \tag{11}$$

$$\frac{\partial \Pi^*}{\partial r} = 0 \quad (r = 1). \tag{12}$$

Note that π^* is expanded in an even series of Chebyshev polynomials like (5). The solution of (11) - (12) is discussed below.

In the final fractional step, viscous effects are included using the Euler backward scheme

$$u^{n+1} = \hat{u}^{n+1} + \frac{\Delta t}{R}(D^2 - \gamma^2)u^{n+1} \quad (r < 1) \tag{13}$$

$$u^{n+1} = 0 \quad (r = 1) \tag{14}$$

$$v^{n+1} = \hat{v}^{n+1} + \frac{\Delta t}{R}(D^2 - \frac{1}{r^2} - \gamma^2)v^{n+1} \quad (r < 1) \tag{15}$$

$$v^{n+1} = 0 \quad (r = 1). \tag{16}$$

The overall scheme is only first order accurate in time because the viscous and pressure operators do not commute. Higher order accuracy in time may be obtained by extrapolation methods.

The implicit parts of the procedure given above all involve solution of an equation of the form

$$(L - \beta^2)\phi = f \quad (r < 1) \tag{17}$$

$$a\phi + b\frac{\partial \phi}{\partial r} = 0 \qquad r = 1 \tag{18}$$

for each Fourier mode, where L is a second order (Laplacian) operator in r, β^2 depends only on the x-Fourier index (not r), and a and b are constants independent of Fourier mode. We discuss briefly here the discretization of L and the method of inversion. For planar geometries L can be written as a tri-diagonal system using a Chebyshev tau-method (Orszag and Kells 1980). This system can then be inverted in $0(P)$ operations for each x-Fourier mode. The curvature terms introduced by the cylindrical geometry destroy the tridiagonal property of the tau-method matrix, and collocation then becomes more attractive due to the ease with which variable coefficient problems can be handled.

To solve the full matrix equations resulting from the collocation approximation of (17) - (18), an eigenfunction solver is used that reduces the operation count from $0(P^3)$ to $0(P^2)$ while only requiring the storage of one $P \times P$ matrix for given (L,a,b). More precisely, we diagonalize the collocation approximation to L as

$$L = \Psi^{-1} \Lambda \Psi$$

The solution to (17) - (18) can then be written as

$$\phi = \Psi^{-1} \, (\Lambda - \beta^2 I)^{-1} \, \Psi f$$

The diagonalization (independent of Fourier mode) is done in a pre-processing stage.

Finally, the initial conditions for the runs presented here are of the form

$$\vec{v}(x,r,t = 0) = (1-r^2)\vec{x} + A \, \vec{v}_L(x,r)$$

where $\vec{v}_L$ is an eigenfunction of the fourth-order linear stability equation obtained from (1) - (3) by assuming a solution of the form

$$\vec{v} = (1-r^2)\vec{x} + \varepsilon\psi(r) \, e^{i(x-\omega t)\alpha}$$

and linearizing with respect to ε. The magnitude of the perturbation is characterized by its energy relative to that of the unperturbed flow:

$$E = 12 \int_0^1 (u^2 + v^2) r \, dr \qquad (19)$$

The details of the linear problem are well-documented (Lessen et al 1968, Davey & Drazin 1969, Salwen et al 1980) and will not be discussed here. The numerical procedure used to determine the eigenvalue ω and eigenfunction $\psi(r)$ for given R, α is similar to that described by Orszag (1971) for planar geometries, except

that collocation rather than the tau-method is used.

3. RESULTS

Before investigating finite-amplitude behavior it is necessary to confirm that the direct simulation gives decay rates and phase velocities in agreement with those predicted by linear theory. The results of two such tests are summarized in Table 1, where it is seen that the code adequately resolves both center and wall modes at modest time steps (even without using extrapolation methods to reduce the first order error in time).

The results of linear theory can also be used to test whether interactions between a primary mode and its harmonic are accurately simulated. For pipe flow, a center mode with wavenumber α nearly resonates with its harmonic in the sense that the phase speed of the mode with wavenumber 2α is very close to that of the primary. If one assumes they resonate exactly (i.e. $\omega_{2r} = 2\omega_{1r}$), the harmonic will obey a forced amplitude equation of the form

$$\frac{\partial A_2}{\partial t} = \omega_{2i} A_2 + 0(A_1^2) e^{2\omega_{1i} t}$$

and thus A_2 grows secularly in t for short times and attains a maximum at

$$t_r^* = \frac{\ell n(-2\omega_{1i}) - \ell n(-\omega_{2i})}{-2\omega_{1i} + \omega_{2i}} \qquad (20)$$

As the modes are not exactly phase-locked, we would expect the actual maximum to occur at $t^* < t_r^*$. This behavior is verified in Fig. 1 by a plot of t^*/t_r^* at $\alpha = 1$ for various Reynolds numbers. The maximum deviation between (20) and our direct simulations is -3%.

Next, we study finite-amplitude disturbances predicted to be dangerous by the method of false problems. Davey & Nguyen (1971) find that the two disturbances tested above at very small amplitude (see Table 1) have threshold (unstable equilibrium) energies (19) of $E \simeq 0.003$. The method of Itoh (1977) as applied by Davey (1978) indicates that the center mode should decay at finite amplitude, however it too predicts a small-amplitude equilibrium state for the wall mode. To test these theoretical results, the same series of runs reported in Table 1 were repeated except that the axial and radial resolution was increased, the time integration was taken to a final time of $T = 20$ rather than $T = 10$, and the initial energies of the disturbance were taken to be 0.01. The results for the wall mode

and center mode are shown in Figs. 2 and 3 respectively, as plots of the logarithm of the primary and secondary energies as a function of time. There is apparently no evidence of equilibria. Runs at lower and higher initial energies (e.g. $E \simeq 0.04$) decay in a similar manner.

The lack of equilibria reported above does not preclude their existence for other Reynolds number/ wavenumber combinations. However, in a variety of runs, we have found no finite-amplitude steady-states. The results of a typical run at $R = 4000$, $\alpha = 1.0$, $\omega = 0.3783 - i\ 0.1025$, are plotted in Fig. 4. From Fig. 4 we infer that the disturbance at $R = 4000$ decays in a time very short compared to a diffusive time scale, and is therefore consistent with the absence of equilibria (Orszag & Patera 1980).

The time scale for decay of finite-amplitude axi-symmetric states is central to an understanding of three-dimensional transition. The three-dimensional instability mechanism leading to transition in plane Poiseuille and Couette flows (Orszag & Patera 1980) develops on a time scale of order $1/\sqrt{E}$, where E is the energy of the two-dimensional disturbance. For the disturbance plotted in Fig. 4, $1/\sqrt{E}$ is significantly shorter than the time scale on which the perturbation decays.

Thus, it seems that the instability we found in planar channel flows may be relevant to transition in pipe flow as well. This possibility will be investigated further in a later paper in which the behavior of non-axisymmetric disturbances to decaying axisymmetric states will be considered.

Our results indicate that the method of false problems is not a valid procedure for investigating finite-amplitude axisymmetric perturbations to pipe flow. We do not attempt a critique of these methods here except to emphasize a point made by Herbert (1977). Herbert commented that the retention of only the first term in the amplitude expansion of the frequency without knowing the convergence properties of the series can lead to incorrect conclusions, especially in cases (such as pipe flow and plane Couette flow) where there is no linear neutral curve. The radius of convergence of the amplitude expansion may simply be too small to predict equilibria. For example, numerical simulations of plane Couette flow (Orszag & Kells 1980, Patera & Orszag 1980) do not confirm the existence of two-dimensional equilibria predicted by Davey & Nguyen (1971) on the basis of amplitude expansions. The direct iteration procedure of Herbert (1977) bypasses this problem and can predict the existence of equilibria as well as their threshold energy.

However, a limited survey of the available phase space has not yet yielded any finite-amplitude solutions. We suspect there are none.

REFERENCES

Davey, A. 1978 On Itoh's finite amplitude stability theory for pipe flow. J. Fluid Mech., 86, 695-703.

Davey, A. & Drazin, P. G. 1969 The stability of Poiseuille flow in a pipe. J. Fluid Mech., 36, 209-218.

Davey, A.& Nguyen, H.P.F. 1971 Finite-amplitude stability of pipe flow. J. Fluid Mech., 45, 701-720.

Gottlieb. D. & Orszag, S.A. 1977 Numerical Analysis of Spectral Methods: Theory and Applications. NSF-CBMS Monograph No. 26 Soc. Ind. App. Math., Philadelphia.

Herbert, T. 1977 Finite amplitude stability of plane parallel flows. In Laminar-Turbulent Transition, AGARD Conf. Proc. No. 224, 3-1-3-10.

Itoh, N. 1977 Nonlinear stability of parallel flows with subcritical Reynolds number. Part 2. Stability of pipe Poiseuille flow to finite axisymmetric disturbances. J. Fluid Mech., 82, 469-479.

Lessen, M., Sadler, S. G. & Liu, T. Y. 1968 Stability of pipe Poiseuille flow. Phys. Fluids, 11, 1404-1409.

Metcalfe,R.W., & Orszag, S.A. 1973 Numerical calculation of the linear stability of pipe flows. Flow Research Report No. 25, Kent, Washington.

Orszag, S. A. 1971 Accurate solution of the Orr-Sommerfeld stability equation. J. Fluid Mech., 50, 689-703.

Orszag, S. A. & Kells, L.C. 1980 Transition to turbulence in plane Poiseuille and plane Couette flow. J. Fluid Mech., 96, 159-205.

Orszag, S. A. & Patera, A.T. 1980 Subcritical transition to turbulence in plane channel flows. Phys. Rev. Letters, 45, 989-992.

Patera, A. T. & Orszag, S. A. 1980 Transition and turbulence in planar channel flows. In Proc. 7th Int. Conf. on Numerical Methods in Fluid Dynamics (ed. W. C. Reynolds and R. W. MacCormack), p.xxx, Springer.

Salwen, H., Cotton, F.W., & Grocsh, C. E. 1980 Linear stability of Poiseuille flow in a circular pipe. J. Fluid Mech., 98, 273-284.

Table 1. Behavior of Linear Modes

	Wall Mode	Center Mode
R	1600.	500.
α	5.8	6.2
Re ω	1.5849	5.8852
Im ω	-0.5396	-0.3917
Perturbation Energy	1×10^{-10}	1×10^{-10}
Spatial Resolution ($2N\times(P+1)$)	8×33	8×17
Δt	0.005	0.01
Final Time, T	10.	10.
Computed Re ω	1.5836	5.9146
Computed Im ω	-0.5410	-0.3876

FIGURE CAPTIONS

Fig. 1 The ratio of the time at which the harmonic attains its maximum to the time predicted by linear theory (assuming perfect phase-locking) is plotted as a function of Reynolds number when $\alpha = 1$. The actual (computed) time is less than the predicted linear theory time because the real frequency of the harmonic is not exactly twice that of the primary.

Fig. 2 Decay of a wall mode at $R = 1600$, $\alpha = 5.8$ from an initial energy ($E = 0.01$) larger than the equilibrium value predicted by the method of false problems. Higher energy disturbances also decay. Here E is the energy of the disturbance relative to the mean flow [defined in (19)]. Here $N = 8$ and $P = 64$ in (4)- (5). The accuracy of this and other runs was tested by changing N, P and the time step Δt.

Fig. 3 Decay of a center mode at $R = 500$, $\alpha = 6.2$ from an initial energy ($E = 0.01$) larger than the equilibrium value predicted by perturbation theory. Here $N = 8$ and $P = 32$ in (4)- (5).

Fig. 4 Decay of a wall mode at $R = 4000$, $\alpha = 1$. The decay occurs on a time scale much shorter than the diffusive scale indicating the absence of equilibria. Here $N = 8$ and $P = 32$ in (4) - (5).

Fig. 1 The ratio of the time at which the harmonic attains its maximum to the time predicted by linear theory (assuming perfect phase-locking) is plotted as a function of Reynolds number when $\alpha = 1$. The actual (computed) time is less than the predicted linear theory time because the real frequency of the harmonic is not exactly twice that of the primary.

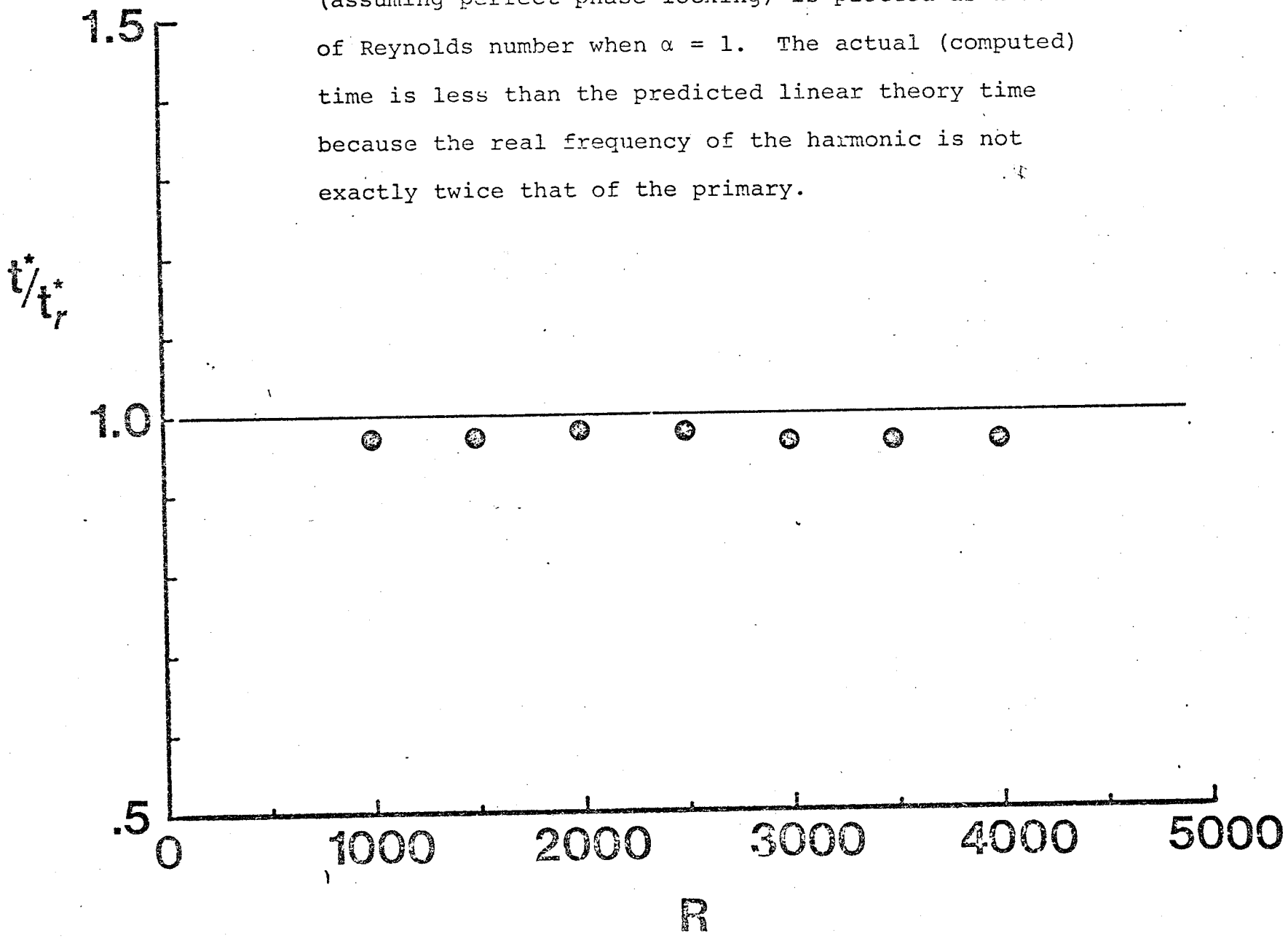

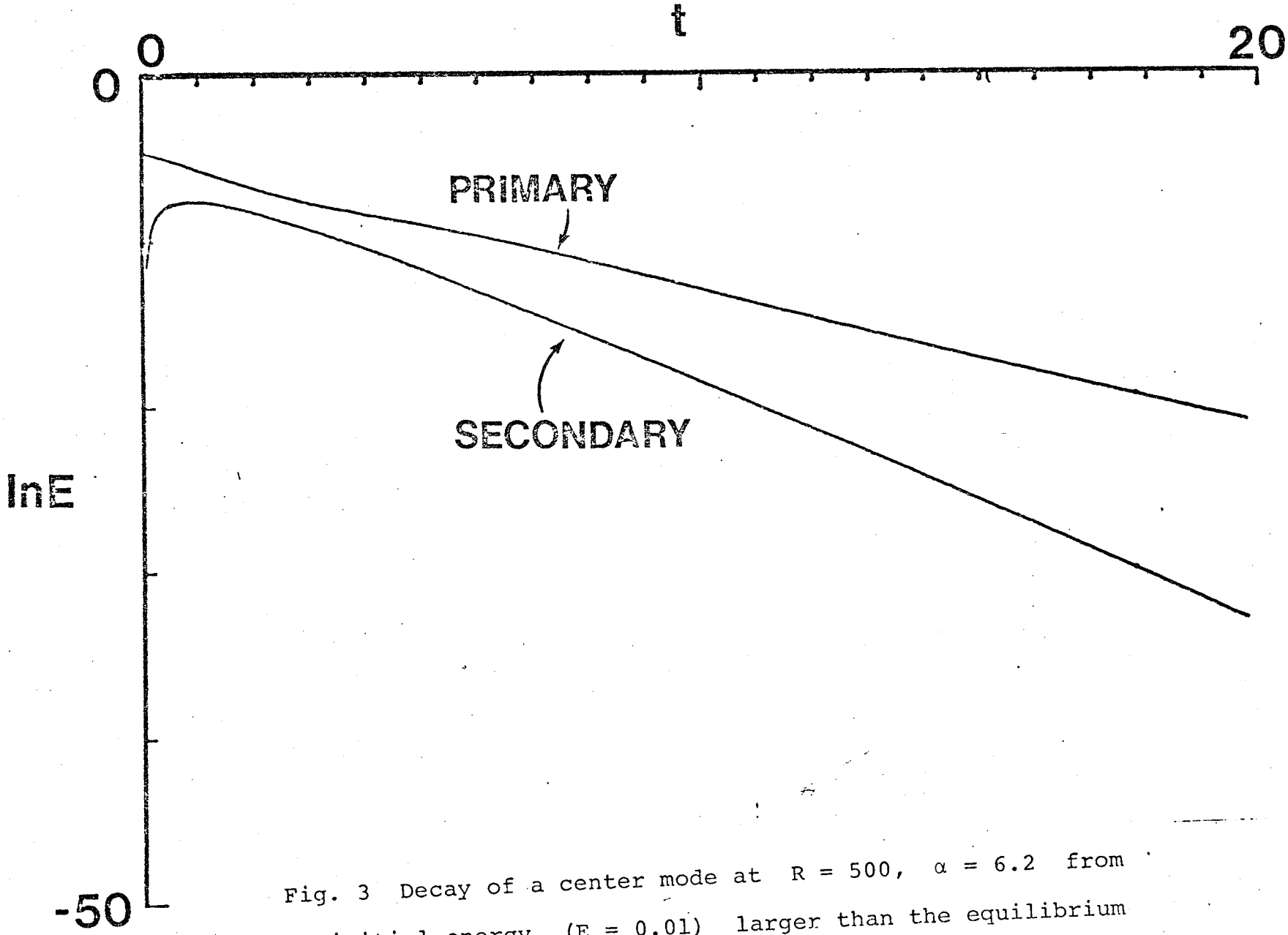

Fig. 3 Decay of a center mode at $R = 500$, $\alpha = 6.2$ from an initial energy ($E = 0.01$) larger than the equilibrium value predicted by perturbation theory. Here $N = 8$ and $P = 32$ in (4)- (5).

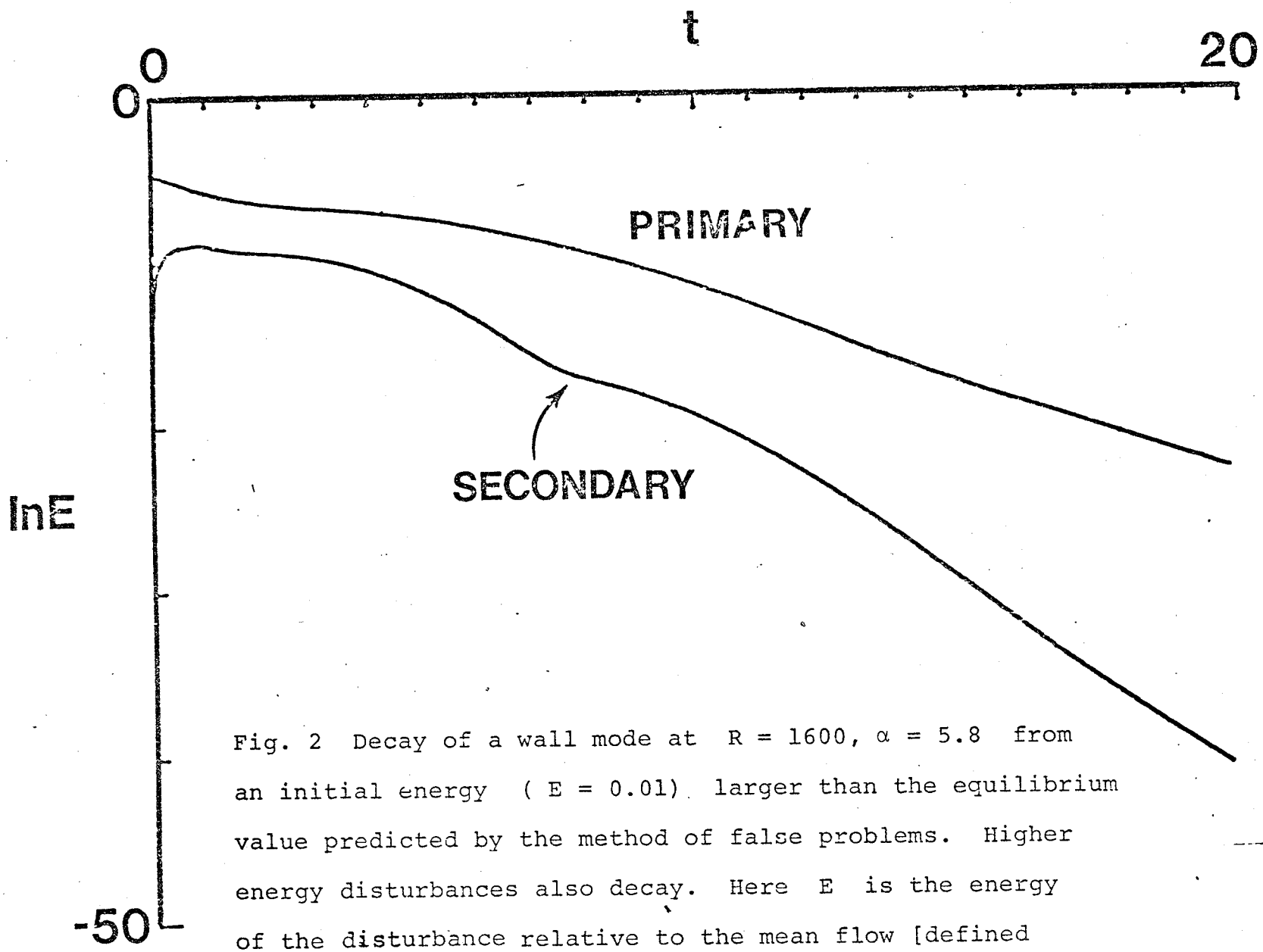

Fig. 2 Decay of a wall mode at $R = 1600$, $\alpha = 5.8$ from an initial energy ($E = 0.01$) larger than the equilibrium value predicted by the method of false problems. Higher energy disturbances also decay. Here E is the energy of the disturbance relative to the mean flow [defined in (19)]. Here $N = 8$ and $P = 64$ in (4)- (5). The accuracy of this and other runs was tested by changing N, P and the time step Δt.

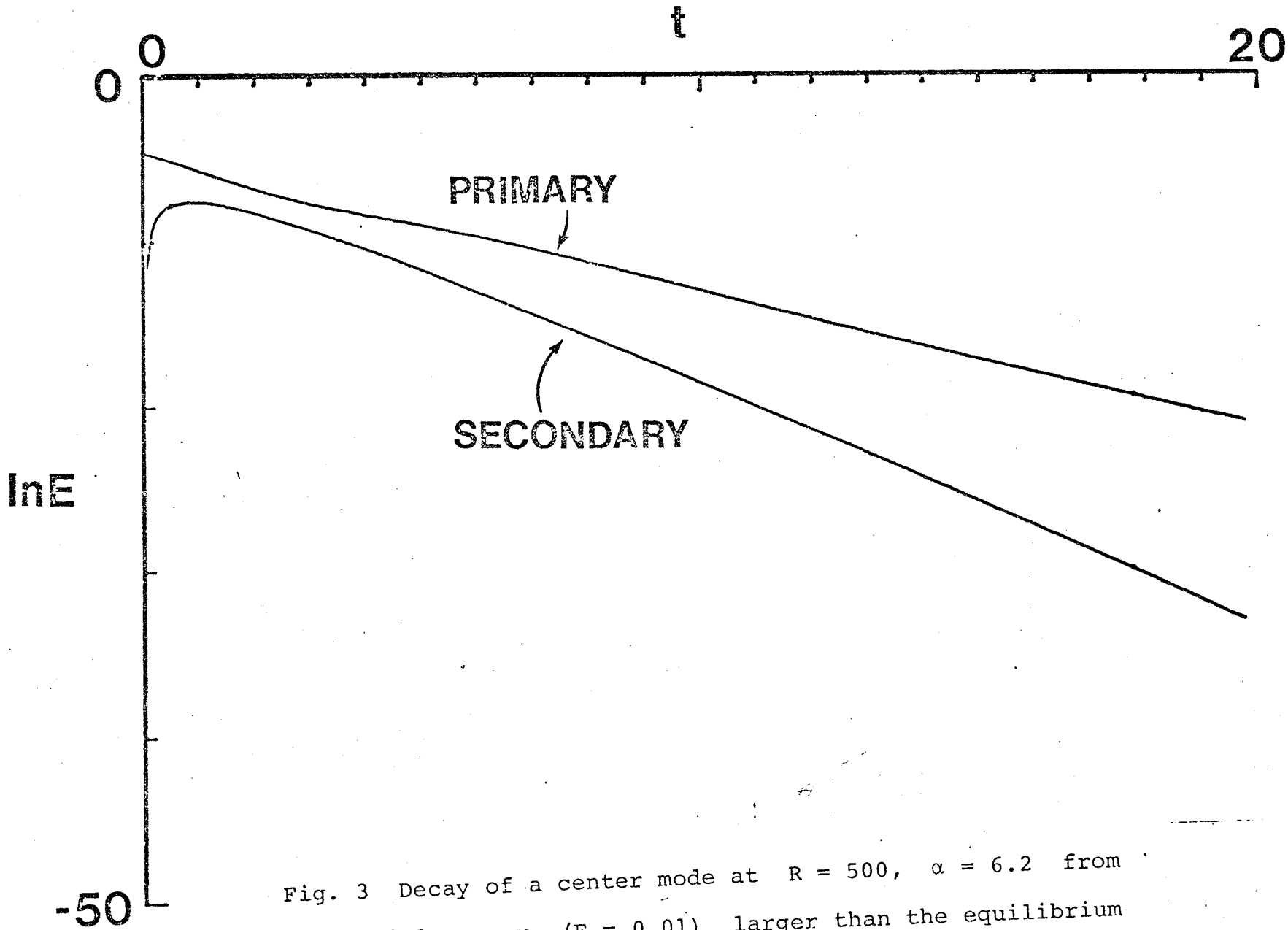

Fig. 3 Decay of a center mode at $R = 500$, $\alpha = 6.2$ from an initial energy ($E = 0.01$) larger than the equilibrium value predicted by perturbation theory. Here $N = 8$ and $P = 32$ in (4)- (5).

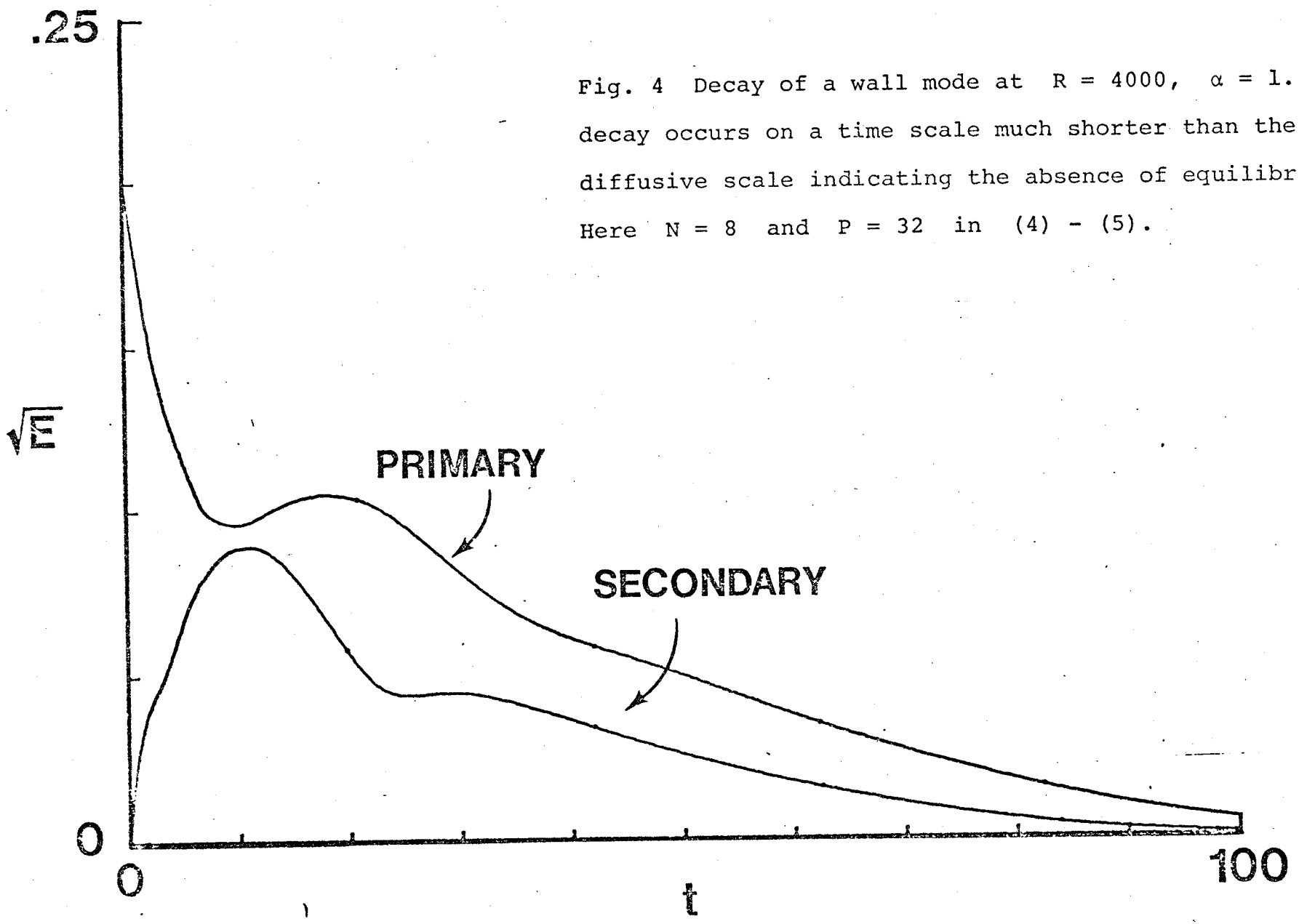

Fig. 4 Decay of a wall mode at $R = 4000$, $\alpha = 1$. The decay occurs on a time scale much shorter than the diffusive scale indicating the absence of equilibria. Here $N = 8$ and $P = 32$ in (4) - (5).

1. Report No.	2. Government Accession No.	3. Recipient's Catalog No.
NASA CR-165661		

4. Title and Subtitle	5. Report Date
ADVANCED STABILITY ANALYSES FOR LAMINAR FLOW CONTROL	February 1981
	6. Performing Organization Code
7. Author(s)	8. Performing Organization Report No.
Steven A. Orszag	CHI Report No. 43
	10. Work Unit No.
9. Performing Organization Name and Address Cambridge Hydrodynamics, Inc. P.O. Box 249, M.I.T. Station Cambridge, Massachusetts 02139	11. Contract or Grant No. NAS1-15894
	13. Type of Report and Period Covered Final
12. Sponsoring Agency Name and Address National Aeronautics and Space Administration Washington, D.C. 20545	14. Sponsoring Agency Code

15. Supplementary Notes

Langley Technical Monitor: Dennis M. Bushnell

16. Abstract

Five classes of problems are addressed. (i) The extension of the SALLY stability analysis code to the full eighth-order compressible stability equations for three-dimensional boundary layer flows is discussed. The resulting computer code seems to be at least an order of magnitude faster than previous codes. (ii) A comparison of methods for prediction of transition using SALLY is given for incompressible flows. It is shown that the envelope method is most efficient. (iii) A study of instability and transition in rotating disk flows is given in which the effects of Coriolis forces and streamline curvature are included. Good agreement with experiments performed at NASA LaRC is demonstrated. (iv) A new 'linear' three-dimensional instability mechanism that predicts Reynolds numbers for transition to turbulence in planar shear flows in good agreement with experiment is introduced and studied. (v) A study of the stability of finite-amplitude disturbances in axisymmetric pipe flow shows the stability of this flow to all nonlinear axisymmetric disturbances, in contrast to the predictions of nonlinear stability theory.

17. Key Words (Suggested by Author(s))	18. Distribution Statement
Stability theory Laminar flow control Nonlinear stability Transition Shear flow Numerical methods Boundary layers Spectral methods	Unlimited - Unclassified

19. Security Classif. (of this report)	20. Security Classif. (of this page)	21. No. of Pages	22. Price*
Unclassified	Unclassified	124	

For sale by the National Technical Information Service, Springfield, Virginia 22161